POLITECNICO DI MILANO

School of Civil, Environmental and Land Management Engineering
Master of Science in Environmental and Land Planning Engineering

DEVELOPING AN OPERATIVE TOOL FOR WATER STRESS MONITORING BASED ON HYDROLOGICAL MODEL AND EARTH OBSERVATIONS:
THE CAPITANATA CONSORTIUM CASE STUDY

Advisor: Prof.ssa Chiara Corbari
Co-Advisor: Ing. Nicola Paciolla

Master thesis by:
Giada Restuccia Matr. 900422

Academic Year 2019/2020

Abstract

In Mediterranean regions drought conditions occur frequently, and the irrigation consortium and the farmers must deal with water scarcity which implies a decrease in the agricultural yields and economic problem. Therefore, the development of techniques for the optimization of the management of the water resource destined to irrigation is highlighted. In this thesis a tool for water stress monitoring based on earth observation and hydrological model is developed, applied on the case study of Capitanata Consortium in Puglia. Soil moisture ground observations at high spatial and temporal resolution are correlated with vegetative indices from Landsat at field scale. Then, the same analysis is performed at basin scale using Landsat and Sentinel2 images and soil moisture estimates from the hydrological model FEST-EWB, which is validated with Land Surface Temperature (LST) images from Landsat for the years 2015-2019. Agricultural drought process is finally analyzed and a combined drought index, able to identify water scarcity conditions is proposed. Combining the standardize precipitation index and the anomalies of soil moisture, evapotranspiration, land surface temperature and vegetation stress information in such way that different levels of drought are detected. Therefore, coupling modeled hydrological variables, ground observation and remote sensing data at two different spatial and temporal scales, anomalies and water stress indices are computed. The results at different scale are discussed and compared with irrigation aqueduct volumes of consortium.

Sintesi

Nelle regioni del Mediterraneo si verificano molto frequentemente fenomeni di siccità, i consorzi per l’irrigazione e gli agricoltori devono far fronte alla scarsità della risorsa idrica che comporta una diminuzione della resa agricola e di conseguenza problemi economici. In questo contesto, risulta fondamentale lo sviluppo di tecniche per l’ottimizzazione della gestione della risorsa idrica destinata all’irrigazione. L’obiettivo di questo elaborato di tesi consiste nello sviluppo di uno strumento operativo per il monitoraggio dello stress idrico basato su un modello idrologico e su immagini satellitari, applicato al caso di studio del Consorzio per la Bonifica della Capitanata in Puglia.

Dati al suolo di umidità ad alta risoluzione spaziale e temporale sono stati correlati a scala di campo con indici di vegetazione da Landsat. Poi, la stessa analisi è stata condotta a scala di bacino utilizzando immagini satellitari da Landsat e Sentinel2 e umidità del suolo stimata tramite il modello idrologico FEST-EWB, il quale è stato validato con immagini Landsat di Land Surface Temperature (LST) per gli anni 2015-2019. Infine, analizzando il processo di siccità agricola è stato proposto un indicatore di siccità combinato in grado di rilevare condizioni di stress idrico. Sono stati definiti differenti livelli di siccità combinando l’indice standardizzato di precipitazione, le anomalie di umidità del suolo, evapotraspirazione, LST e le informazioni sullo stress vegetativo. Le anomalie e l’indice sono stati calcolati utilizzando le variabili modellate, le osservazioni al suolo e le immagini satellitari su due scale spaziali e temporali differenti. Infine, per validare l’indice di siccità è stato effettuato il confronto con i volumi dell’acquedotto irriguo del consorzio.

Index

Introduction 1
Chapter 1 7
1.1 Hydrological Model 7
  1.1.1 Statistical Indices.. 9
  1.1.2 Correlation coefficients 10
  1.1.3 Autocorrelation.. 10
1.2 Earth Observation indexes and variables 11
  1.2.1 Satellite soil moisture products 11
  1.2.2 Vegetation Indexes 12
    1.2.2.1 Normalized Difference Vegetation Index 13
    1.2.2.2 Normalized Difference Water Index 14
    1.2.2.3 Modified Soil Adjusted Vegetation Index 15
    1.2.2.4 Fractional Vegetation Cover and Leaf Area Index 15
    1.2.2.5 Enhanced Vegetation Index 15
  1.2.3 Land Surface Temperature 16
1.3 Drought Indicators.. 16
  1.3.1 Anomaly 17
    1.3.1.1 Standard Precipitation Index (SPI)... 18
    1.3.1.2 Standard Precipitation Evapotranspiration Index (SPEI)..................... 19
    1.3.1.3 Soil Water Deficit Index (SWDI)... 19
  1.3.2 The combined drought indicator 20
Chapter 2 23
2.1 Study area... 23
2.2 Data 24
  2.2.1 Soil moisture ground observation 24
    2.2.1.1 GROW sensors.. 24
    2.2.1.2 Continuous monitoring stations 26
  2.2.2 Soil moisture satellite products 28
  2.2.3 Vegetative indices 29
    2.2.3.1 Landsat and Sentinel2 29
    3.2.3.2 MODIS 30
  2.2.4 Land surface temperature 30
    2.2.4.1 Landsat 30
    2.2.4.2 MODIS 31

  2.2.5 Precipitation 32
    2.2.5.1 Ground Precipitation 32
    2.2.5.2 Precipitation from ERA5 32
Chapter 3 35
3.1 Sensor in tomato fields 35
  3.1.1 Soil moisture time series 37
  3.1.2 Soil moisture and vegetative indices 40
3.2 Sensors in asparagus and other vegetables fields 42
3.3 Fixed monitoring station 43
  3.3.1 Temporal correlations 46
Chapter 4 48
4.1 Comparison between observed LST and simulated RET 48
  4.1.1 Spatial autocorrelation 52
  4.1.2 Temporal correlations 52
  4.2 Spatial LST – NDVI relationship 55
Chapter 5 59
5.1 Long time series analysis (2000-2020) 59
  5.1.1 Anomalies 59
    5.1.1.1 Precipitation anomaly and SPI1 59
    5.1.1.2 Soil moisture anomalies 61
    5.1.1.3 Land surface temperature anomalies 64
    5.1.1.4 Vegetative indices anomalies 65
  5.1.2 Correlation between anomalies 68
  5.1.3 Agricultural combined drought Index 69
  5.1.4 Drought index validation 74
    5.1.4.1 Comparison with irrigation aqueduct volume (2006/16) 74
    5.1.4.2 Comparison with news from local newspaper 76
5.2 High resolution analysis (2015-2019) 76
  5.2.1 Anomalies and water stress indices 76
    5.2.1.1 Precipitation anomaly and SPI1 76
    5.2.1.2 Soil moisture anomaly 77
    5.2.1.3 LST and RET anomaly 79
    5.2.1.4 Vegetative indices anomaly 80
    5.2.1.5 Evapotranspiration deficit anomaly 82
    5.2.1.6 SPEI 83
    5.2.1.7 SWDI 84
  5.2.2 Anomaly on cultivated fields 85
  5.2.3 Anomaly maps 87

5.2.4 Correlation between anomalies 89
5.2.5 Combined drought index 90
Conclusion 93
Bibliography 95
Index of Figures 100
Index of Tables 103
Ringraziamenti 105

Introduction

By 2050, it is estimated that the population will reach 9.7 billion and one in four people will suffer water scarcity (WPP, 2019). Water scarcity can be related to scarcity in availability due to physical shortage or scarcity in access due to inadequate infrastructure or the failure of institution to ensure regular water supply. Thus, the concept of water scarcity does not only involve arid, drought areas and the availability of water but also on its quality. Drought can arise from several causes and conditions so that create different typology of drought. Meteorological drought due to precipitation scarcity, hydrological if there a depletion in low streamflow, agricultural if the soil is not adequate to grow a crop in healthy state and, also socioeconomic drought when the socioeconomic contest is the cause.

Moreover, studies on the climate change effect on water requirement demonstrate that the water scarcity will increase around the globe, especially in regions where suffering conditions already exist, and only within a mitigation scenario large overall water saving could be possible (Fischer, Tubiello, van Velthuizen, & Wiberg, 2007). In the present social economic context, the water demand will increase not only because of this population growth but also of the current lifestyle and improvement living standards (Ravazzani et al., 2017). Hence, a sustainable use of water, through an improvement in its management, and a changing in production and consumption of our goods, are necessary to face up this issue.

In this scenario, the agriculture, that is the largest user of water among human activities, indeed irrigation water withdrawals are 70% of the total anthropogenic use of renewable water resources (Fischer et al., 2007), has seen an improvement in water management. Therefore, new technologies and efficient irrigation scheduling are required to meet the increase in water demand and the change of socio-economics outlook. In this contest, words as ‘smart irrigation’ and ‘smart farming’ started to be frequently used in farm and irrigation management (Ravazzani et al., 2017). Often agricultural decisions and the irrigation scheduling are made only on the base of farmers’ personal experience. While in the past the farmers could work at individual scale, today the agriculture has to face different issues at global scale, as the water security, the sustainability along the production chain and the optimization of crops yield. (Vuolo, Essl, & Atzberger, 2015).
A continuous development and improvement in irrigation practices are the aim of several studies carried out in the last decades (Ceppi et al., 2014; Ravazzani et al., 2017; Vinukollu, Wood, Ferguson, & Fisher, 2011; Vuolo et al., 2015). Predict the level of soil water in the root

zone and a priori knowledge of soil moisture can improve the crop yield, optimize the water resource management leading to large economic benefits. Hence, the keys of an efficient water management are the evaluation of evapotranspiration (ET) and the soil moisture (SM), that play a role of pillars in water and energy balance.

The evapotranspiration is a combined process of evaporation of liquid water from various land surfaces, transpiration from leaves of plants and sublimation of ice and snow (Vinukollu et al., 2011). Only having a depth knowledge of this term and its spatial distribution the water management and the determination of water saving measures can be achieved (Droogers, 2000). However, the ET assessment is very complex due to heterogeneity, spatial and temporal distribution of the variables involved. Indeed, ET direct measurement through an eddy covariance station or a lysimeter, and more in general in situ methods need great resources and efforts and are not completely trustworthy (Bastiaanssen et al., 2005). Direct measurement of soil moisture is complex and very local, therefore hydrological model able to compute evapotranspiration and soil moisture at different spatial and temporal scales are needed.

Satellite-based Earth Observations (EO) development have increased the possibility to estimates at higher resolutions and accuracy ET and SM, and therefore the irrigation practices and the water-resource management. The possibility to retrieve the key variables of the soil-water balance from satellite measure gave the opportunity to build new tool for the water stress monitoring.

The development of sensors able to measure spectral reflectance and emittance at different spectral bands gives the opportunity to quantify agronomical parameters, providing quantitative assessment of crop requirement and vegetation characteristics (Hatfield, Gitelson, Schepers, & Walthall, 2008). Nowadays, vegetative indices (VIs), resulting from waveband combination, are widely used tools for stress crop assessment, implying an improvement in water management and in crop yields.

Several satellite missions aim to soil moisture retrievals have been released in the last decades. Passive, such as the radiometer and scatterometer, and microwave-based instruments are used to monitor soil moisture both spatially and temporally (Al Bitar et al., 2012; Brocca et al., 2018; Kerr et al., 2001; W Wagner et al., 2000), even tough for operational water management applications can be used at irrigation district scales (passive sensor spatial resolution is in between 25 and 50 km) but not for field scale irrigation management. Some efforts are now focused in the direction of soil moisture pixel disaggregation (Merlin et al., 2010). The second concern is related to the retrieval of the soil water content of few centimetres, which is not congruent with the hydrological active soil for plant root zone uptake. Moreover, there are problems linked to the saturation of soil moisture retrieval algorithms for active radars (Giacomelli, Bacchiega, Troch, & Mancini, 1995) and their ability to detect soil moisture over vegetated surfaces (Bindlish & Barros, 2001).

Instead Land Surface Temperature (LST) computed using the thermal infrared (TIR) spectra, retrieved from several sensors installed on board the satellites (Jiménez-Muñoz & Sobrino, 2003) is widely used in energy or energy-water balance models to compute evapotranspiration.

A wide panorama of applications of the earth observations is provide by scientific literature. It’s possible to subdivided ET estimation approaches into genetic algorithm, budget models and distributed hydrologic models.

Considering the algorithm-based approaches, (Vinukollu et al., 2011) analyzed the P-M equation and its streamlined version, called Priestley-Taylor equation, using remote sensing data as input. Both surface meteorological data, radiative flux and vegetation parameters derive from satellite observations. The soil moisture dynamic is not directly included in these algorithms, therefore, considered values come from vegetation characteristics and vapor pressure deficit.

On the other hand, *one source* energy balance models that compute the evapotranspiration as a residual term of the balance, as the Surface Energy Balance Algorithm for Land (SEBAL) and the Surface Energy Balance System (SEBS), are widely used.

The former was tested worldwide, in more than 30 countries, assessing that remote sensing data for the estimation of ET is a precious tool when a priori knowledge of soil, crop and management conditions lacks (Bastiaanssen et al., 2005). Moreover, in (Cammalleri, Ciraolo, La Loggia, & Maltese, 2012), the assumption of scaling satellite instantaneous values of the fluxes, involved in the ET balance, to average daytime values was tested. The capability of the SEBAL model under different water condition is also demonstrated.

The latter was analyzed in (Vinukollu et al., 2011), instantaneous fluxes at global scale generated from SEBS model and observed data from an eddy covariance station were compared. Both the models, only taking into account the energy fluxes, neglect the mass transfer, hence, the direct calculation of the soil moisture is not possible.

Soil moisture prediction is vitally to achieve the best irrigation practices, but in the previous approaches the soil moisture problem remains unresolved. To solve this issue, recently, spatially distributed hydrological models based on the coupling of the energy and water balance models, as the FEST-WB and FEST-EWB (Corbari, Ravazzani, & Mancini, 2011; Corbari, Salerno, Ceppi, Telesca, & Mancini, 2019) were applied to irrigation districts where the availability of ground measurements is low, to compute evapotranspiration and SM by merging ground and satellite data. Distributed models can compute the main processes of hydrological cycle: evapotranspiration, infiltration, run off, subsurface flow, snow dynamic and soil water content (Ceppi et al., 2014). Thus, are able to estimate a continuous and direct values of SM and ET, to evaluate and forecast water deficit. Furthermore, satellite images, having an intrinsic raster structure, are suitable for calibration and validation phases of these models.

Projects such as the PREGI in 2013, the SEGUICI in 2016 and the SIM (Smart Irrigation from Soil Moisture Forecast Using Satellite and Hydro-Meteorological Modelling) in 2018 aimed to a optimize irrigation scheduling using hydrological models, ground measurements, weather forecast and satellite observations developing drought forecasting operative systems. In (Corbari et al., 2019) a focus in Puglia region is presented. In Mediterranean regions, such us Puglia, drought conditions occur frequently, and the irrigation consortium must deal with water scarcity which implies also economic problem as the increase of water costs for the farmers.
In this contest, where surface moisture conditions declined rapidly because of high temperatures and enhanced evaporative losses, the needed of rapid response indicator was highlighted.
A simple and immediate tool must be the key of a reliable support decision system for water stress monitoring and managing. Drought, like other hazards, can be characterized in terms of their severity, location, duration and timing. Indeed, several drought indicators and indices, with different specification, are provided in literature, an overview is presented in (Svoboda & Fuchs, 2017). The range of indices and indicators typically used to detect agricultural drought, such as NDVI, has a limitation, because even if they have demonstrated their capability to detect vegetation stress, this stress is not necessarily related to drought (Sepulcre-Canto, Horion, Singleton, Carrao, & Vogt, 2012). Therefore, the current strategy in operational drought monitoring is to assemble a suite of independent indicators, sampling different types of impacts on the agricultural drought and then blend these indicators into a unique tool for water stress detection. On this matter, the development of a single combined drought indicator that makes use of meteorological, evapotranspiration, soil moisture, land surface temperature and vegetation stress information can enable the monitoring of agricultural drought and its evolution in space and time at different spatial and temporal scale (Del Pilar Jiménez-Donaire, Tarquis, & Vicente Giráldez, 2020). Anomalies of the hydrological variables combined with other indices can identify water scarcity conditions and may also play a role, providing an historical background, in irrigation management planning on agricultural field.

In this thesis a tool for water stress monitoring based on earth observation and hydrological model is developed at different spatial scale. Firstly, soil moisture ground observation high spatial and temporal resolution, land surface temperature and vegetative indices satellite retried from Landsat and Sentinel2 are analyzed at field scale. Studying their correlation, a new definition of stress threshold is searched to better regulate the irrigation timing. Then, moving to basin scale the same analysis are carried out, using Landsat and Sentinel2 images and soil moisture estimates from the hydrological model FEST-EWB, which is validated with Land Surface Temperature (LST) images from Landsat for the years 2015-2019. Studying the agricultural drought process and its evolution phases, the method proposed in this thesis combines the standardize precipitation index and the anomalies of SM, LST and NDVI, in such way different levels of drought can be defined.

Therefore, two parallel analysis are carried out. Long time series from 2000 to 2020 of SM, LST, NDVI and precipitation retrieved from remote sensing at low resolution are used to calculate anomalies at basin scale. Simulated hydrological variables and high-resolution satellite images for a shorter period from 2015 to 2019 are analyzed: distributed, averaged anomaly are computed considering the total consortium area and only for cultivated field. The agricultural combined drought index is performed, for both the series, and its reliability is assessed using irrigation aqueduct volumes of the consortium area.

This thesis is structured as follow:
In Chapter 1 methods and tools used are introduced;
In Chapter 2 the case study area and the data are described;
In Chapter 3 soil moisture ground observations analysis at field scale is developed and commented;
In Chapter 4 hydrological model validation is discussed;
In Chapter 5 anomalies and water stress indices calculation is provide, the agricultural combined drought index is developed, and its reliability is assessed.

Chapter 1

Methodology

This chapter aims at reviewing methods and tools used in the analysis. Firstly, the distributed hydrological model implemented for the mass and energy fluxes quantification at irrigation district scale and the tool for its validation are detailed. Then, an overview of water stress and drought indices which can be retrieved from satellite earth observation as a support of water management is provided. Finally, an outline of the instrument for water stress detection such us the anomaly and indices that will be implemented in the indicator for the drought assessment is described.

1.1 Hydrological Model

FEST-EWB is a distributed hydrological energy water balance model that computes the main processes of hydrological cycle such as evapotranspiration, infiltration, surface runoff, flow routing, subsurface flow and snow dynamic. The model is based on a system of two equations, one that involves the water balance (1.1) and the other the energy balance (1.2). The key variable is the land surface temperature (LST, both the equations are written in term of LST, this permit a direct comparison between LST maps retrieved from satellite. The value of LST that close the balance in any pixel of the basin surface is the representative equilibrium temperature (RET).

The model solves the following equations' system at the ground surface:

$$\begin{cases} \dfrac{dSM}{dt} = \dfrac{P + I - R - PE - ET}{dz} & (1.1) \\ R_n - G - H - LE = \dfrac{dS}{dt} & (1.2) \end{cases}$$

where: SM (-) is the soil water content, P (mm) is the precipitation rate, I (mm) the irrigation rate, R (mm) is the runoff flux, PE (mm) is the drainage flux, ET (mm) is the evapotranspiration, dz (mm) is the soil depth, R_n (Wm^{-2}) is the net radiation, G (Wm^{-2}) is the soil heat flux, H (Wm^{-2}) is the sensible heat flux, LE (Wm^{-2}) is the latent heat flux, dS/dt encloses the energy storage terms, such as the photosynthesis flux and the crop and air enthalpy changes.

The core of the model is the system between soil surface, vegetation and low atmosphere that are linked through ET, that is linked to the latent heat flux by the equation:

$$LE = \lambda \rho_w ET \qquad (1.3)$$

$$LE = \frac{\rho_a c_p}{\gamma}(e^* - e_a)\left[\frac{f_v}{r_a + r_c} + \frac{1 - f_v}{r_{abs} + r_s}\right] \qquad (1.4)$$

Where λ is the latent heat of vaporization, ρ_w the water density, ρ_a the air density, γ the psychometric constant, f_v the vegetation fraction, c_p the specific heat of humid air. The saturation vapour pressure (e*) is a function of the RET and the vapour pressure (e_a) a function of air temperature. The canopy resistance (r_c) is expressed following (Jarvis, 1976), while the soil resistance (r_s) according to Sun (1982). The aerodynamic resistance (r_a for vegetation and r_{abs} for bare soil) is computed using the model from Thom (1975).

So following this approach, SM is linked to the LE and then to RET. LE is computed as a function of LST, that closes the energy balance, but at the same time the LE, as effective ET, is a term of the mass equation, which compute at every time step the SM evolution.
If, more SM is available in the soil, more ET is present, and less energy is available for heating the surface. Hence, considering the system of energy and mass equation, LST variability can influence SM changes significantly.

The distributed model is applied to the study area discretized with a regular mesh made by square cells of 30x30m. For each cells every input parameter is defined, and all variables are calculated.

The model needs the following input:

1. *Meteorological variables* such as the air temperature, incoming shortwave radiation, wind velocity, air humidity, precipitation. Data related to 45 stations distributed in the study area from 8th November 2013 to 24th September 2019 are used.

2. *Soil parameters* such as the field capacity, wilting point, saturated hydraulic conductivity, Brooks-Corey index, soil depth, residual and saturated soil moisture.

3. *Vegetation parameters* such us the leaf area index (LAI), fraction cover, albedo, minimum stomal resistance, vegetation height, normalized difference vegetation index (NDVI).

4. *Digital elevation model* and *land use/cover map.*

FEST-EWB model is run at spatial resolution of 30 meters and with a time step of 1 hour. The data of irrigation’s volumes for each field are not available, hence, the irrigation is applied considering the average curve retrieved from the annual irrigation volume supplied by the Consortium to the entire area. The irrigation distribution in the model needs the identification of crop areas and their dynamics in time, so fraction cover and NDVI satellite retrievals are implemented in the model. The application is determined by a NDVI threshold equal to 0.3, if the cell has a value of NDVI greater than the threshold irrigation is applied. This decision criterion introduces uncertainties in the irrigation volumes; indeed, the total volume is equally distributed to all the cells having an NDVI value higher that the threshold, not considering the field’s size or the type of crop.

1.1.1 Statistical Indices

To determine the goodness of the hydrological model estimates in term of SM, RET and energy fluxes the following statistical indices: Absolute Mean Bias Error (AMBE), Root Mean Square Error (RMSE) and Nash index, are calculated by these formulas:

$$AMBE = \frac{\sum_{i=1}^{n} |Obs_i - Sim_i|}{n} \tag{1.5}$$

$$RMSE = \sqrt{\sum_{i=1}^{n} \frac{(Obs_i - Sim_i)^2}{n}} \tag{1.6}$$

$$NASH = 1 - \frac{\sum_{i=1}^{n} (Obs_i - Sim_i)^2}{\sum_{i=1}^{n} (Obs_i - \overline{Obs})^2} \tag{1.7}$$

Where n is the sample size, Obs_i are the ith observed values and Sim_i the ith simulated by FEST-EWB and $\overline{Obs}$ is the average observed variable. The simulated and observed values are referred to the same variable, e.i. the RET estimation (simulated variable) is compared with the LST satellite retrieved (observed variable). Nash index can range from -∞ to 1. The index equal to corresponds to a perfect match of modeled to the observed data.

1.1.2 Correlation coefficients

Pearson correlation coefficient

Pearson correlation coefficient is a measure of the linear correlation between two variables. It has a value between +1 and −1, where 1 is total positive linear correlation, 0 is no linear correlation, and −1 is total negative linear correlation.
The coefficient for a sample is calculated by the formula:

$$r_{XY} = \frac{\sum_{i=1}^{n}(x_i - \bar{x})(y_i - \bar{y})}{\left(\sum_{i=1}^{n}(x_i - \bar{x})^2 \sum_{i=1}^{n}(y_i - \bar{y})^2\right)^{\frac{1}{2}}} \qquad (1.8)$$

Where n is the size of the sample, x_i, y_i are the individual sample points indexed with i and $\bar{x}, \bar{y}$ the means of the samples.

Spearman correlation coefficient

In statistics, Spearman's rank correlation coefficient is a measure of rank correlation (statistical dependence between the rankings of two variables). While Pearson's correlation assesses linear relationships, Spearman's correlation assesses monotonic relationships (whether linear or not). If there are no repeated data values, a perfect Spearman correlation of +1 or −1 occurs when each of the variables is a perfect monotone function of the other.

1.1.3 Autocorrelation

Spatial autocorrelation is the term used to describe the spatial variation of a variable observed/measured at different location across a geographical area.
The term spatial autocorrelation suggests its meaning: ‘auto’ as in ‘self’; ‘correlation’ as in the statistical use of that term to measure a ‘relationship’. In fact, the spatial autocorrelation is a measure of the relationship between the value of a variable at a location and the same variable but at another location separated by some specified distance. Positive spatial autocorrelation is the tendency of the areas separated by the specified distance to have similar values of the variable instead negative spatial autocorrelation means dissimilar values.

Autocorrelation curves are computer using the Moran's I correlation coefficient as a function of distance:

$$I(d) = \frac{\frac{1}{W}\sum_{h=1}^{n}\sum_{i=1}^{n} w_{hi}(y_h - \bar{y})(y_i - \bar{y})}{\frac{1}{n}\sum_{i=1}^{n}(y_i - \bar{y})^2} \qquad for\ h \neq i \tag{1.9}$$

where y_h and y_i are the values of variable at location *h* and *i*, w_{hi} is a matrix of weighted values where the elements are a function of distance *d*: equal to 1 if y_h and y_i are within a given distance (for $y_h \neq y_i$) and equal to 0 for all the other cases. W is the sum of a values of the matrix w_{hi}, $\bar{y}$ the mean and *n* is the sample size. The results in coefficients ranging from -1 to +1, where values between [0,1] indicates positive association.

A distance equal to 700 meters is chosen as the maximum distance of autocorrelation and each step (h, i) is equal to 30 meters, corresponding to the pixel size. As a matter of fact, for distances higher than 700 meters no more relationship exists between two values (the coefficient takes zero values), so that a perturbance in a pixel value does not implies any change in pixel far more than 700 meters from it.

1.2 Earth Observation indexes and variables

Remote sensing provides valuable support into agricultural managements. The possibility to quantify crop stress and water content using earth observation of canopy gives a great contribution in water stress monitoring.

In this thesis, the following soil water balance key variables are retrieved by satellite earth observations: SM, VIs and LST.

1.2.1 Satellite soil moisture products

Considering the effects of soil moisture on agricultural management, the availability of soil moisture databases is essential for the prediction of agricultural drought.

Conventionally, soil moisture data are derived from observations of in situ soil moisture networks with different depths and various densities. Such as the sensors used in this thesis and monitoring station (eddy covariance station). But, the development of remote sensing techniques enriched surface soil moisture observations at different temporal and spatial resolutions. Several satellite soil moisture products have been released since the 2000s. Soil moisture retrieval algorithms are continuously developed for both passive and active instruments, such us radiometer, scatterometer and microwave sensor.

These datasets can be useful for drought and flood forecasting, hydrological modeling at large scale and rainfall estimation. The knowledge of the characteristic error, limitations and quality of these soil moisture products becoming even more fundamental, to assure the correct use and improve the product itself. Soil Moisture and Ocean Salinity (SMOS) (Kerr et al., 2010), the Advanced Microwave Scanning Radiometer (AMSR-E) (Imaoka et al., 2012), the Soil Moisture Active Passive (SMAP) (Entekhabi et al., 2010), the Advanced Scatterometer (ASCAT) (Wolfgang Wagner et al., 2013) are ones of the most widely used satellite-based soil moisture datasets. Furthermore, multi-satellite moisture dataset, introduced by the Climate Change Initiative (CCI) program released by the ESA (European Space Agency), i.e. ESA CCI Active and ESA CCI Combined are considered (Dorigo et al., 2017).

In the study of (Cui et al., 2018) an intercomparison between these datasets is developed. The issues common to all the dataset are the spatial resolution and the investigated depth. Indeed, the available satellite products for passive microwave have a spatial resolution between 25 and 100 km, only applying algorithms 1 km of resolution can be reached. Hence, their use at small scale must be done being aware of the uncertainties of which they are affected. Furthermore, the soil investigated depth is around 5-10 cm, depending on the type of crop this depth could not be enough to capture the effective soil moisture. For example, the root apparatus of corn can reach more than 1 meter of depth.

The used datasets in this thesis, with their own specifics are described in Chapter 2 Paragraph 2.2.2.

1.2.2 Vegetation Indexes

The canopy characteristics, such us the content of chlorophyll, pigments (Carotenoids and Anthocyanin), the water content, the nutrients (Nitrogen and Phosphorus), are related to the canopies and leaves reflectance. The reflectance signature of plants extends from the VIS (Visible Spectrum), i.e. the Chlorophyll absorbance region, to the NIR (Near Infrared) i.e. the leaf’s spongy tissue absorbance region till the SWIR (Short Wave Infrared) where the absorption caused by the water content is detected. The plant’s signature compared with the signature of soil and water is visible in Figure 1.1.

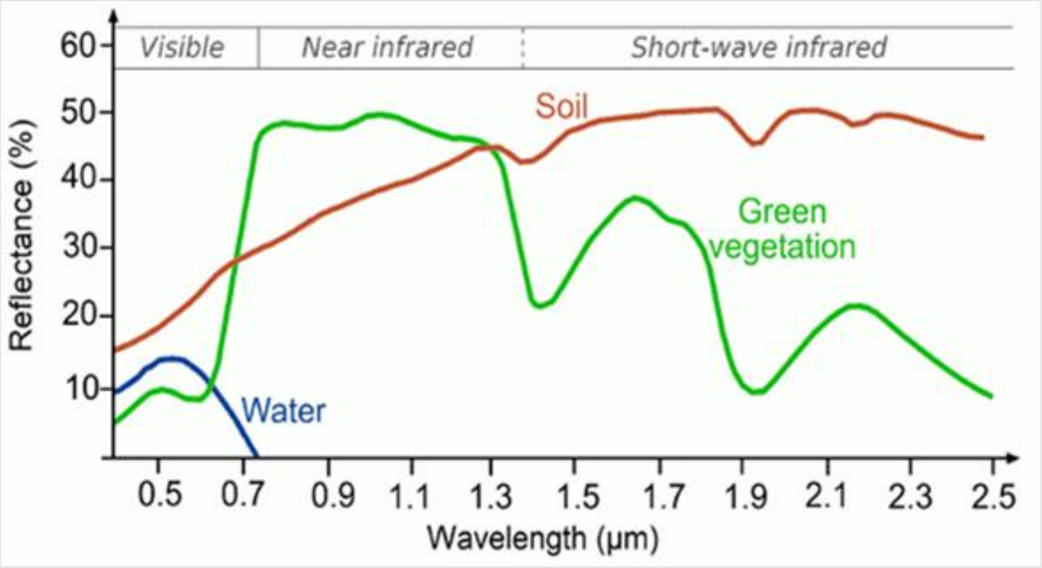

Figure 1.1 Spectral signature of vegetation, soil and water

Therefore, the study of VIS, NIR and SWIR portions of the electromagnetic spectrum provides useful information about vegetation healthy conditions. The development of sensors able to measure spectral reflectance and absorbance gave the opportunity to retried agronomic parameters. Vegetative indices (VIs) linked to greenness (chlorophyll content), pigmentation, water content and nutriment, are assessed from the combination of canopy reflectance at two or more bands of the spectral signature. A vast array of VIs that measure indirectly the healthy state of the plants and provide information about the water availability in the soil, are available.

In this study, the VIs accounted are the Normalized Difference Vegetation Index (NDVI), the Normalized Difference Water Index (NDWI), the Soil Adjusted Vegetation Index (SAVI), the Modified Soil Adjusted Vegetation Index (MSAVI), the Fractional Vegetation Cover (Fcover), the Leaf Area Index (LAI) and the Enhanced Vegetation Index (EVI).

1.2.2.1 Normalized Difference Vegetation Index

The NDVI is a simple indicator that quantifies vegetation by measuring the difference between near-infrared (which vegetation strongly reflects) and red light (which vegetation absorbs). It's part of the *greenness* indices giving information about the vegetation vigor and its state. Indeed, if a plant is dead or stressed reflects more visible light and less near infrared light, on the contrary if the plant is healthy and green absorbed much more the red light. Thanks to its properties the NDVI is one of the most used indices in agriculture.

The index is calculated by the formula:

$$NDWI = \frac{R_{NIR} - R_{SWIR}}{R_{NIR} + R_{SWIR}} \tag{1.10}$$

where R_{NIR} is the reflectance in the Near InfraRed band and R_{red} in the red portion of the spectrum.

Values of NDVI can range from -1.0 to +1.0, but values less than zero typically do not have any ecological meaning, so the range of the index is truncated to 0.0 to +1.0.
Higher values signify a larger difference between the red and near infrared radiation recorded by the sensor so that a highly photosynthetically-activity condition in the canopies. On the contrary, low NDVI values mean there is little difference between the red and NIR signals, little photosynthetically-activity or bare soil.

1.2.2.2 Normalized Difference Water Index

The NDWI is another remote sensing derived index and estimates the leaf water content at canopy level. The water body has a strong absorbance in SWIR band and low in the range between the visible and infrared, the index uses this phenomenon to estimate the water content in canopies.
NDVI is largely used to monitor vegetation growth since this index is strongly correlated to leaf area index. Instead, the NDWI is more related to the quantity of water thus, is commonly used to monitor vegetation water stress, for example in irrigation management. However, stress to plant canopies can be caused by impacts other than drought, and it is difficult to discern them using only NDWI.

The index is calculated by the formula:

$$NDWI = \frac{R_{NIR} - R_{SWIR}}{R_{NIR} + R_{SWIR}} \tag{1.11}$$

where R_{NIR} is the reflectance in the NIR band and R_{SWIR} in the SWIR portion of the spectrum.
Value of the NDWI are in the range of [-1, +1]. Values under the 0 means bright surface with vegetation or water content. Even higher values always represent vegetation with a greater water content.

1.2.2.3 Modified Soil Adjusted Vegetation Index

The MSAVI and SAVI are indices that seek to address some of the limitation of NDVI when applied to areas with a high degree of exposed soil surface.
The indices are calculated by the formula:

$$MSAVI(SAVI) = \frac{(R_{NIR}-R_{red})(1+L)}{R_{NIR}+R_{red}+L} \tag{1.12}$$

where L is soil brightness correction factor. The difference between the indices comes in how L is calculated. In SAVI, L is estimated based on how much vegetation there is (but it's generally left alone at a compromise of 0.5). MSAVI uses the following formula to calculate L:

$$\mathrm{L} = 1 - \frac{2s(R_{NIR}-R_{red})(\mathrm{R_{NIR}}-\mathrm{sR_{red}})}{R_{NIR}+R_{red}} \tag{1.13}$$

where *s* is the slope of the soil line from a plot of red versus near infrared brightness values.
The value of L varies by the amount or cover of green vegetation: in very high vegetation regions, L is equal to 0, and in areas with no green vegetation, L is equal to 1. SAVI/MSAVI range from -1 to 1. The lower the value, the lower the amount/cover of green vegetation.

1.2.2.4 Fractional Vegetation Cover and Leaf Area Index

The Fcover is an intuitive e simple indicator to understand if an area has vegetative covered or not. The values of the index are between 1, that represents total cover such us dense canopies or woods and 0 that is bare soil.
The LAI is defined as the one-sided green leaf area per unit ground surface area in broadleaf canopies. Thus, is directly related to the amount of light that can be intercepted by plants and represent a variable used to predict photosynthetic primary production.

1.2.2.5 Enhanced Vegetation Index

The EVI can be considered a modified NDVI with improved sensitivity to high biomass regions and improved vegetation monitoring capability through a de-coupling of the canopy background signal and a reduction in atmospheric influences.

1.2.3 Land Surface Temperature

The LST is the radiative skin temperature of the land surface that is not the same as the air temperature. Its estimation results from the energy balance of the fluxes between the atmosphere, surface and subsurface soil, so that depends on the albedo, the vegetation cover and the soil moisture. LST is a mixture of vegetation and bare soil temperatures. Because both respond rapidly to changes in incoming solar radiation due to cloud cover and aerosol load modifications and diurnal variation of illumination, the LST displays quick variations too.

Measurement of surface temperature with infrared thermometers has become a routine and offers the potential for crop water stress detection. Different satellites are involved in LST capture, such us the high-resolution Landsat-7 and Landsat-8 satellites and the Moderate Resolution Imaging Spectroradiometer (MODIS).

The used datasets with their own specifics are described in Chapter 2 Paragraph 2.2.2.

1.3 Drought Indicators

Several indices and indicator with different characteristics, data required, and ease of use were developed for the purpose of defining level of drought/wet period and their warning. These indicators are generally based on anomalies over the time period or at monthly scale.
Indices computation can be divided in to three methods (Svoboda & Fuchs, 2017): single index, multiple indices/indicators and composite indicator for drought assessment. Single index/indicator consider only one input e.g. precipitation values, multiple ones derived from different input variables, and the combined ones are not directly computed but are divided into steps or complex calculation. Depending on the aim of the application, the data availability and the specifics of the problems each indicator/index could be more or less suitable.

For example, in the study of (Del Pilar Jiménez-Donaire et al., 2020) a combined indicator called combined drought indicator (CDI), is developed to assess drought period in three Spanish regions. Composed of three warning levels (watch, warning and alert) by integrating three drought indicators: SPI, the anomaly of soil moisture computed with a water balance model and remotely sensed vegetation in term of NDVI data. The indicator revealed a good performance in drought warning system and crop damages are correctly predicted.

In this thesis, a new combined indicator, at daily scale, is developed. In Chapter 5 its validation is carried out. The concept behind the indicator is the cause–effect relationship for agricultural drought. This cause–effect relationship assumes that a deficit of precipitation or irrigation (the cause) leads to a soil moisture shortage that results at first in vegetation water stress and then in drying (the effect). Such a relationship gives the opportunity to provide a system for water stress monitoring, by defining the stage of this dryness process. Figure 1.2 shows the stage of the cause effect relationship in agricultural drought and how it is computed in the combined indicator.

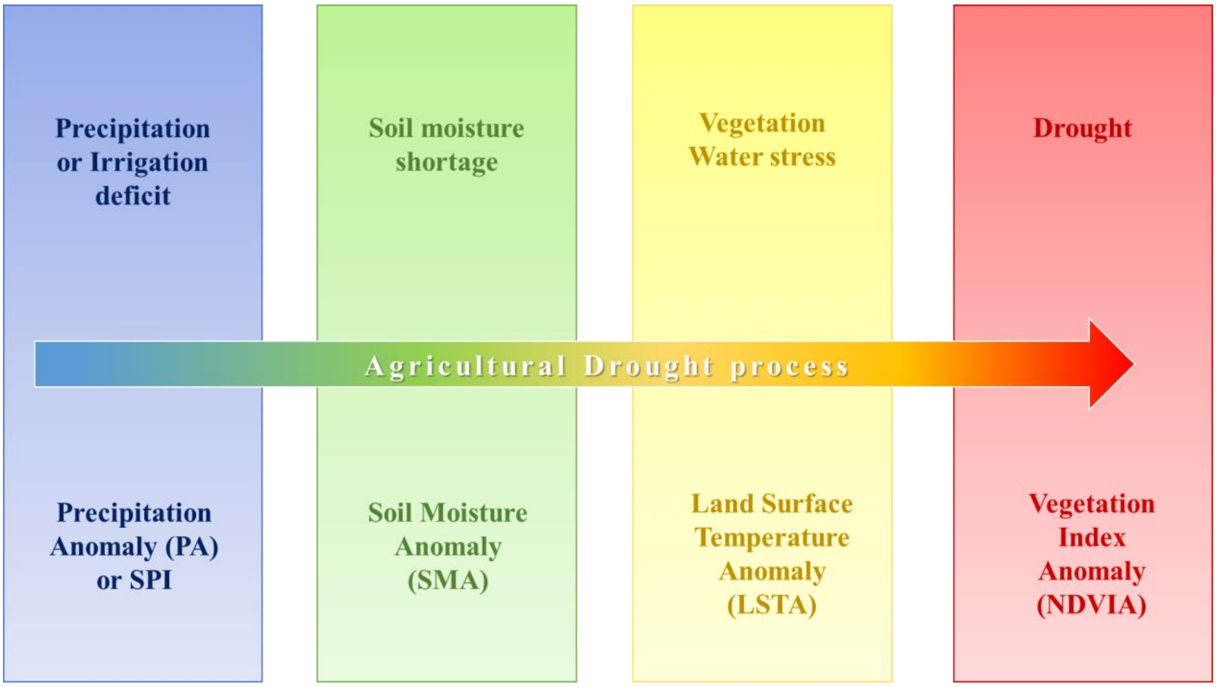

Figure 1.2 Agricultural drought process

1.3.1 Anomaly

The anomaly expresses the deviation of a parameters from a long-term mean value. Thus, their calculation can be useful to understand the spatial distribution and the temporal variation of a variable.

The anomaly is calculated as follow:

$$Anomaly = \frac{X_i - \bar{X}_{total}}{\bar{\sigma}_{X_{total}}} \tag{1.14}$$

where X_i is value of the variable at the ith day, $\bar{X}_{total}$ and $\bar{\sigma}_{total}$ are respectively the mean and standard deviation calculated along all the time series.

In addition, monthly anomalies are computed using the following equation:

$$Montlhy\ Anomaly = \frac{X_{i_m} - \bar{X}_m}{\bar{\sigma}_{X_m}} \tag{1.15}$$

where X_{i_m} is value of the variable at the ith day of the m month, $\bar{X}_m$ and $\bar{\sigma}_{X_m}$ are respectively the mean and standard deviation calculated along each m month of the year. Hence, computing the anomaly in January means compare a value of soil moisture in January with the mean and standard deviation over all the Januarys.

In this study daily are computed the following anomalies: precipitation anomaly (PA), soil moisture anomaly (SMA), vegetative indices anomaly (such as NDVIA and NDWIA), land surface temperature anomaly (LSTA), representative equilibrium temperature anomaly (RETA) and evapotranspiration deficit anomaly (ETdef).

1.3.1.1 Standard Precipitation Index (SPI)

The Standardized Precipitation Index (SPI-n) (McKee et al., 1993) is a statistical indicator that compares the total precipitation at a location during a period of n months with the long-term precipitation distribution for the same period at that location. It is calculated considering the deviation of precipitation values with respect to the mean value at a defined temporal scale and then divided by the standard deviation, as if was an anomaly but long-term record is fitted to a gamma probability distribution, which is then transformed into a normal distribution so that the mean SPI for the location and desired period is zero and unit variance. Having an index with fixed mean and variance, gives the opportunity to have comparable values for different areas or scale and to account likewise wet and dry periods.

Depending on the aim of the application SPI is calculated at multiple time scale, considering a moving window of n months, where n indicates the precipitation accumulation period, the index is calculated on 1, 3, 6, 9, 12, 24 or 48 months. SPI values for 1-3 months might be useful for drought monitoring, values for 6 months or less for monitoring agricultural impacts and values for 12 months or longer for hydrological impacts.

For this thesis, using daily precipitation values the SPI on 1 month (SPI 1) is computed using an easy to use and readily available program called ‘SPI Generator’ provided by the National Drought Mitigation Center (NDMC).

SPI has an intensity scale in which both positive and negative values are calculated, which correlate directly to wet and dry events. The index’s scale is visible in Table 1.1.

Table 1.1 Classification of drought according to SPI

SPI Values	Category
SPI ≥ 2.0	Extremely wet
1.5 ≤ SPI < 2.0	Severely wet
1 ≤ SPI < 1.5	Moderately wet
0< SPI <1	Mildly wet
-1.0 < SPI < 0	Mild drought
-1.5 < SPI ≤ -1.0	Moderate drought
-2.0 < SPI ≤ -1.5	Severe drought
SPI ≤ -2.0	Extreme drought

1.3.1.2 Standard Precipitation Evapotranspiration Index (SPEI)

The Standardized Precipitation Evapotranspiration Index (SPEI) (Vicente-Serrano, Beguería, & López-Moreno, 2010) is an extension of the widely used SPI. The index is designed to considering both precipitation and potential evapotranspiration values in determining drought. Thus, unlike the SPI, it takes into account the impact of temperature on water demand. The computation is like SPI index where the deficit between precipitation and potential evapotranspiration is fitted to log-logistic distribution. Like the SPI, the SPEI can be calculated on a range of timescales from 1-48 months.

For this thesis, using daily precipitation values the SPEI on 1 month is computed using a MATLAB code.

1.3.1.3 Soil Water Deficit Index (SWDI)

The Soil Water Deficit Index (Martínez-Fernández, González-Zamora, Sánchez, & Gumuzzio, 2015), which is based on the surface SM, the SM at field capacity and the available water, can be used to capture agricultural drought conditions through bio-physical principles.
The SWDI is calculated as follows:

$$SWDI = \left(\frac{\theta - \theta_{FC}}{\theta_{AMC}}\right) 10 \tag{1.16}$$

where θ is the SM, θ_{FC} is the SM at field capacity, and θ_{AWC} is the SM at the available water content and is calculated by subtracting the SM at wilting point (θ_{WP}) from the SM at field capacity (θ_{FC}).In addition, the range of values is transformed from a fractional magnitude to a range with agricultural meaning by multiplied by 10.

The critical threshold of SWDI to distingue between drought and non-drought conditions is represented by zero value. Thus, positive values indicate no drought because excess water is available for plant absorption, while negative ones imply agricultural drought due to inadequate water for plant growth. When the $SWDI \leq -10$, the water deficit is absolute, which means the soil water content is below the lower limit of available water for crops. The level of drought corresponding to SWDI values are visible in Table 1.2.

Table 1.2 Classification of drought according to SWDI

SWDI values	**Level of drought**
SWDI >0	No drought
0>SWDI>-2	Mild
-2>SWDI>-5	Moderate
-5>SWDI>-10	Severe
-10 <SWDI	Extreme

1.3.2 The combined drought indicator

Starting from the assumption of agricultural drought, the indicator is divided into 4 steps. Precipitation or water deficit is assessed using the PA or SPI index. Soil moisture shortage is evaluated by SMA. Then the vegetation stress and drying are respectively estimated by LSTA and NDVIA.

The indicator can take the following values:

During the irrigation period, between March and October, meteorological drought (PA/SPI<0) does not lead to hydrological drought (SMA<0) if the irrigation is applied correctly. Hence, the indicator takes 1 (or 0.5 if NDVIA<0) i.e. adequate irrigation condition (blue indicator).

Values of PA or SPI higher than zero means wet condition, the indicator takes 0 value i.e. no drought (green indicator).

For values of PA or SPI less than zero with no soil moisture involvement, the indicator takes -1 value i.e. mild drought (pale indicator).

If precipitation or irrigation deficit is assessed and SMA is less than zero, soil moisture shortage is confirmed. The indicator takes -2 value i.e. moderate drought (yellow indicator).

If soil moisture deficit is assessed and LSTA is less than zero also vegetation water stress is confirmed. The indicator takes -3 value i.e. severe drought (orange indicator).

If vegetation water stress is assessed and NDVIA is less than zero drying is confirmed. The indicator takes -4 value i.e. extreme drought (red indicator).

A delay between meteorological drought and the rise of soil moisture shortage can occur. Thus, the indicator can take halfway values i.e. -1.5, -2.5, -3.5, because the precipitation deficit at the previous day is considered.

In Table 1.3 the classification of drought according to the combined drought index is visible.

Table 1.3 Classification of drought according to the agricultural combined drought index

Index value	PA/SPI1	SMA	LSTA	NDVIA	Condition
1	<0	>0	<0	>0	Irrigation (March/October)
0.5	<0	>0	<0	<0	Irrigation (March/October)
0	>0	>0	<0	>0	No drought
-1	<0				Mild Drought
-1.5	day-1<0	<0			
-2	<0	<0			Moderate Drought
-2.5	day-1<0	<0	>0		
-3	<0	<0	>0		Severe Drought
-3.5	day-1<0	<0	>0	<0	
-4	<0	<0	>0	<0	Extreme Drought

Chapter 2

Case of study and data

In this chapter a framework of the case study and data used in the analysis are presented. Fist the Capitanata consortium area is described briefly. Then, soil moisture, vegetative indices, land surface temperature and precipitation datasets from ground observation and remote sensing are described. Characteristic and problems of the datasets are explained in detail.

2.1 Study area

The study site is the Capitanata irrigation consortium near Foggia (Puglia) the total area is around 1000 km^2 (Figure 2.1). As in all the Mediterranean regions, the climate in Puglia is very hot and dry in summer and temperate during the winter, so that the region is affected by water scarcity problems. The farms cultivate fresh vegetables such as cabbage, fennel between September and April, tomatoes during summer, asparagus during all the year, and wheat. This zone is highly irrigated generally performing sprinkle or drip irrigation on demand.

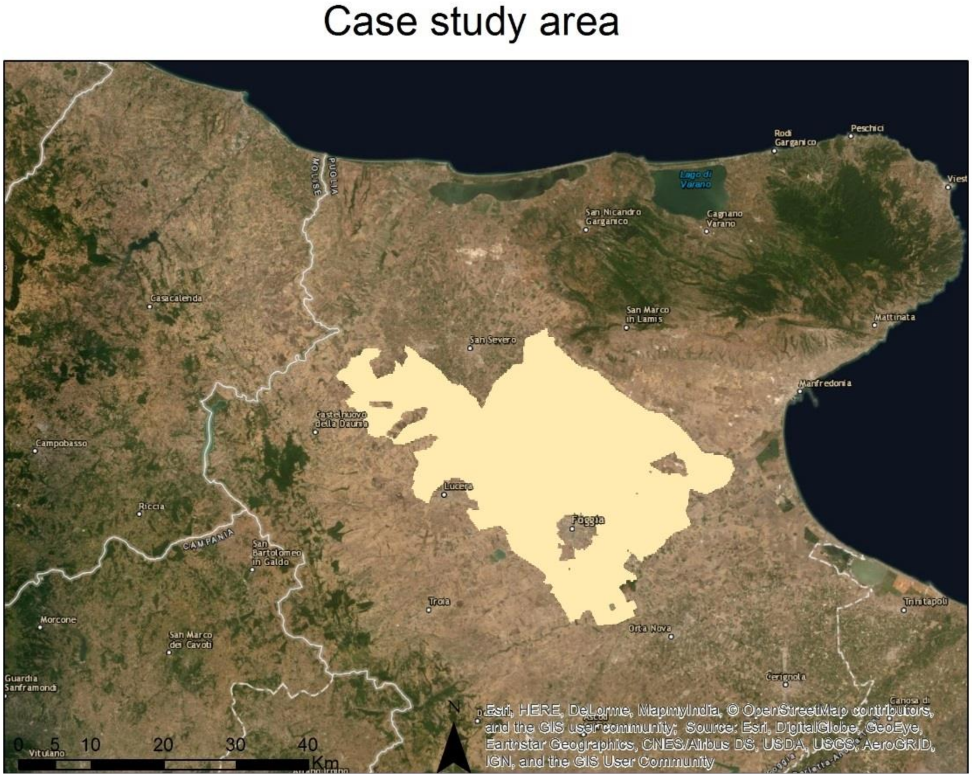

Figure 2.1 Case study area: Capitanata irrigation Consortium

2.2 Data

The variables of interest for the analysis are soil moisture, vegetative indices, land surface temperature and precipitation. For each variable different dataset are implemented in the analysis, both ground measurement and remote sensing images with different spatial and temporal resolution.

2.2.1 Soil moisture ground observation

2.2.1.1 GROW sensors

Soil moisture is measured by 300 cheap and easy to use sensors installed in the cultivated field of the Consortium area (Figure 2.2). The sensors register soil moisture around every 15 minutes and are inserted in the first 5-10 centimeters of the soil surface. Daily and hourly average of the series are computed to have comparable series of soil moisture for each sensor. Each field is independently managed by the owners that means that each field and crop have their own irrigation scheduling.

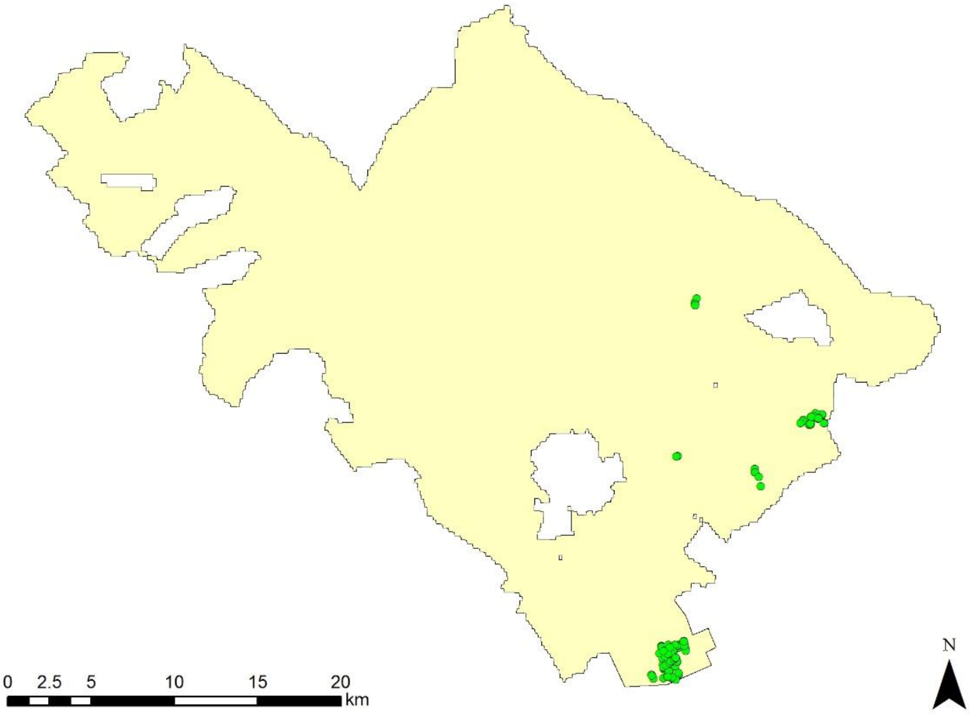

Figure 2.2 Spatial distribution of GROW sensors

For each sensor, identified by four characters code, the position in geographic coordinates (latitude, longitude), the day of activation, the type of crops at the time of installation, the identification number of filed where is located, the day of the last survey and in case of deactivation/broken its cause, are available. For the further analysis, the geographic coordinates of the sensors are projected in WGS84 UTM Zone 33N system. An example of dataset for two sensors, one active and one disabled, is visible in Table 2.1.

Table 2.1 Example of sensors dataset

Active	**Field**	**Crop**	**Active from**	**Last survey**	**Cod.**	**Lat**	**Long**	**Problems**
No	359 *(Onoranza Consortium)*	Tomato	22 July	October	EB70	41.44955	15.68401	Harvested with tomato
Yes	75 *(Giannasi Farm)*	Asparagus	23 July	October	E9B4	41.35302	15.61463	-

The sensors have been installed in the field of the consortium area in July 2019 and they have registered soil moisture series hourly since the 22 of July till the 20 of October. During this period some crops have been harvested or seeded hence, the sensor could be in bare soil for some periods of time. For example, tomato field are harvested at the end of august then are bare soil from September to October, on the contrary other crops such the fennel or cabbage field at the begin of July are bare soil or with very small plants that grow during summer.
Unfortunately, despite the high number of sensors installed several broke or have been destroyed by the harvest than only a reduced number of them could be used for the analysis. Moreover, maybe due to an error in data download the soil moisture series have a serious lack of data, from the 28th July till the 11th August no data have been registered from any sensors. Due to these problems only 145 sensors, that one with long enough series, are considered for the analysis.

The configuration of the usable sensors for the analysis is visible in Figure 2.3 (southern sensors) and Figure 2.4 (eastern sensors). Fractional cover higher than 0.05 is considered in Figure, high spatial resolution is obtained.

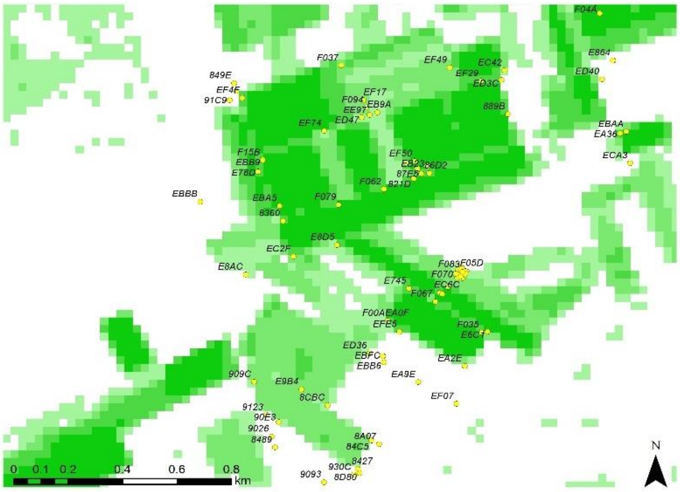

Figure 2.3 Sensors configuration (southern area)

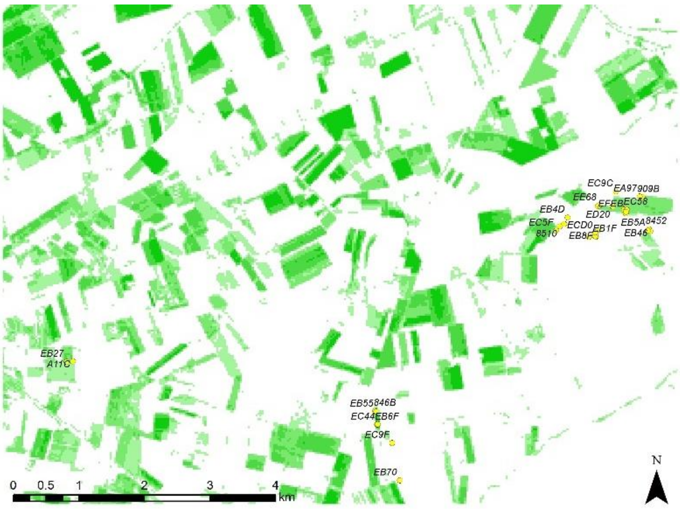

Figure 2.4 Sensors configuration (eastern area)

2.2.1.2 Continuous monitoring stations

The fields visible in Figure 2.5 are monitored with fixed meteorological station equipped with sensors to measure soil moisture and meteorological forcing such us air temperature, air temperature, incoming shortwave radiation, wind velocity, air humidity and precipitation. The data retried from these stations are also used as input of the hydrological model together with others monitoring stations spread on the area. The soil moisture data are available every 30 minutes, daily mean is calculated.

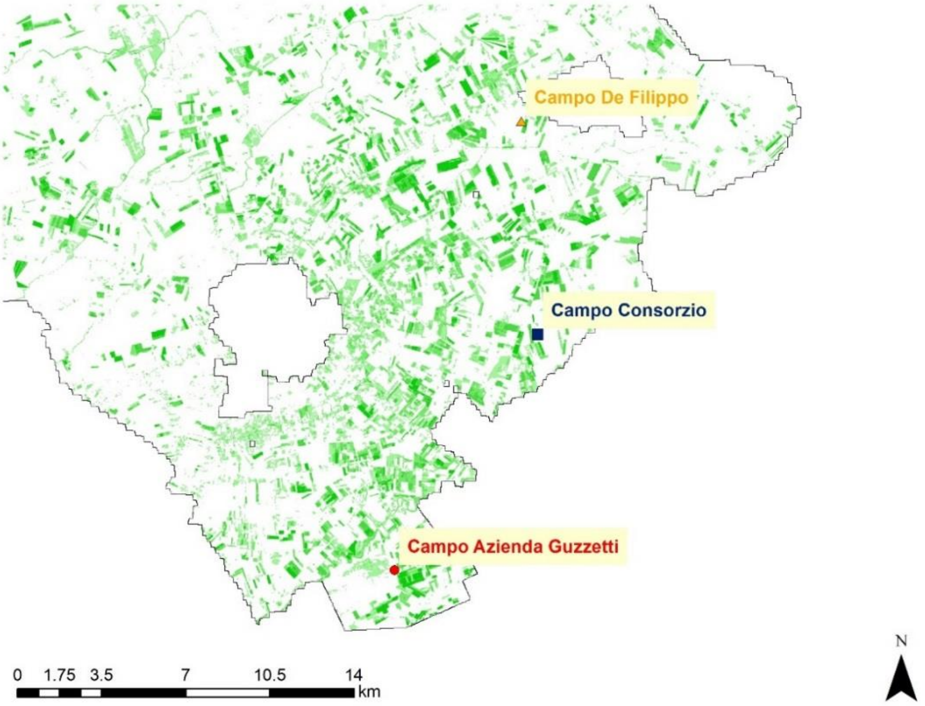

Figure 2.5 Fields with monitoring stations

The analyzed periods are the following:

- *Onoranza Consortium Tomato Field* soil moisture data available from 27th May to 23rd September 2019;
- *De Filippo Field* is cultivated with tomato from 28th April to 1st August 2017 and with grain from the 1st September 2017 to 1st October 2018.

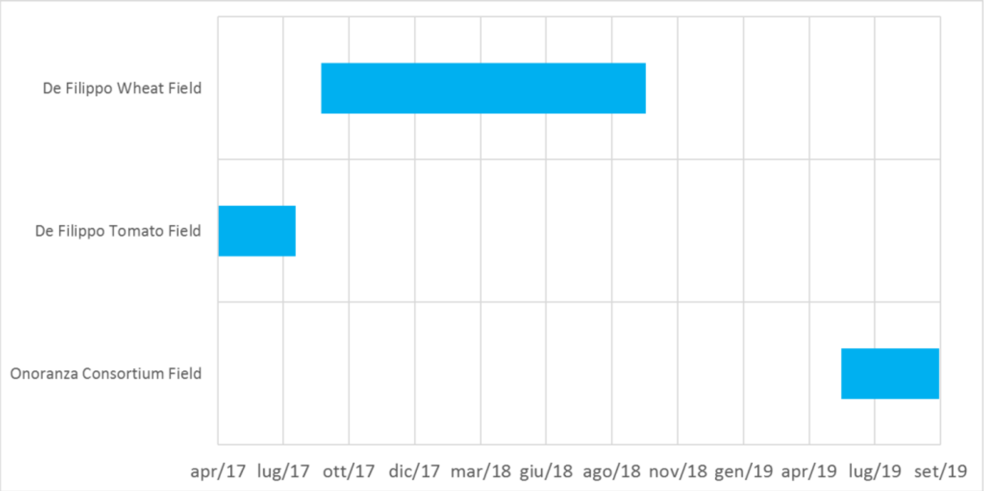

Figure 2.6 Temporal duration of monitoring stations data

2.2.2 Soil moisture satellite products

The soil moisture satellite products are retrieved from different source such us the SMOS, SMAP and satellite and from multi-satellite dataset ESA CCI Active and Passive.

1. The SMOS mission is a soil moisture-dedicated satellite, which carries an interferometric L-band radiometer, in orbit since its launch by ESA the 2nd November 2009. The satellite monitors the global near-surface soil moisture every three days, with the ascending orbit at 6:00 A.M. (SMOS-Asc) and the descending orbit at 6:00 P.M. (SMOS-Des). The daily SMOS-Asc soil moisture product with 50 km of resolution is used. The basin area is almost 60km so that only one pixel is enough to cover it, in Figure 2.7 is visible the size of images' pixel used to retrieve the data. SMOS soil moisture dataset is available from 13th January 2010 to 30th March 2020.

2. The SMAP mission was launched by the National Aeronautics Space Agency (NASA) in January 2015. The satellites are used to retrieve the global surface soil moisture information at 0–5 cm using the L-band radiometer. Like SMOS satellite, the SMAP have the ascending orbit at 6:00 P.M. (SMAP-Asc) and the descending orbit at 6:00 A.M. (SMAP-Des). The SMAP can provide SM data at 40 km of resolution (Figure 2.7) every three days, soil moisture series are available from 4th April 2015 to 30th March 2020.

3. The ESA-CCI are soil moisture products derived from ESA Climate Change Initiative program and are the first multi satellite soil moisture dataset. The active part is retried from microwave scatterometers, the passive one from microwave radiometers. The ESA CCI active blends only active products, instead the ESA CCI combined combines both active and passive data. The daily ESA CCI Active product with 0.25° (around 30km) of resolution is used. In this case, having higher spatial resolution with respect to SMOS, 3 pixels are necessary to cover the case study are, in Figure 2.8 is visible the size of the three pixels a mean of their values is used to retrieve the soil moisture data. ESA CCI active dataset is available from 1st January 2000 to 31st December 2019, ESA CCI combined from 1st January 2000 to 31st December 2018.

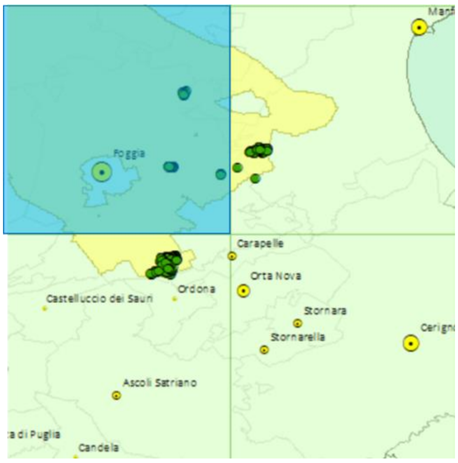

Figure 2.7 Pixel size of SMOS and SMAP images

Figure 2.8 Pixel size of ESA CCI active/combined images

4. The Copernicus Global Land Service (CGLS) is a component of the Land Monitoring Core Service (LMCS) of Copernicus, the European flagship programme on Earth Observation (Bauer-Marschallinger et al., 2018). Soil moisture is derived daily from microwave radar data observed by the Sentinel-1 SAR satellite sensors, with 1km of spatial resolution. Data from the 1st January 2015 to 31st December 2018 are available.

2.2.3 Vegetative indices

2.2.3.1 Landsat and Sentinel2

Images form the Sentinel2 (S2A), Landsat 7 (L7) and Landsat 8 (L8) satellite are used to retrieved vegetation parameters such as the Fcover, LAI, NVDI, NDWI, MSAVI, MSI. Landsat satellites overfly the case study area every 15 days then using Landsat 7 and 8 the temporal resolution is around 7/8 days and spatial resolution of 30 meters. Instead, Sentinel2 have 5 days of temporal resolution and spatial resolution of 30 meters. Satellite images from 2013 to 2019 are available. These are obtained from Skokovic (2017).

The dataset provided contains 2 different type of LST satellite images: the *directly measured* images and the *composite* ones (to overcome clouds problems).The latter are re-elaborated correcting the previous problems, such as the lack of data and the clouds, means by algorithms that take in to account the index values belonging to images of the days before. This is feasible because vegetation dynamic is not instantaneous.

3.2.3.2 MODIS

Satellite vegetation indices values are provided by The Terra Moderate Resolution Imaging Spectroradiometer Vegetation Indices (MOD13Q1) every 16 days at 250 meters spatial resolution and by Moderate Resolution Imaging Spectroradiometer (MODIS) Terra MOD09A1 every 8 days with 500 meters of spatial resolution.
NDVI, NDWI, MSAVI and EVI values from 18th February 2000 to 30th March 2020 with both spatial and temporal resolution are used in the analysis.

2.2.4 Land surface temperature

2.2.4.1 Landsat

LST images at high resolution are retrieved from L8 and L7 satellite with 30 meters of spatial resolution every 8/15 days. These are obtained from Skokovic (2017).
The images are captured at the time of the passage of the satellite over the area with no correction in fact this kind of images are affected by 3 problems:

- *Problem with clouds*: as we can see in fig, in cloudy days the resulting satellite images are also covered by clouds that can affect the values of LST measured. For this reason, in our analysis only clear sky days are considered (Figure 2.9).

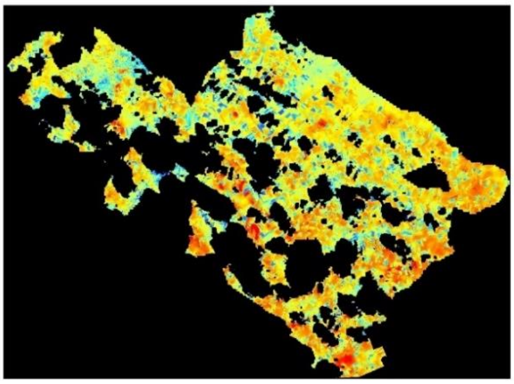

Figure 2.9 Clouds in LST satellite images

- *Strips in L7 sensors:* the one of the sensors belonging to L7 is broken and all the images retried by L7 satellite present by black strips, i.e. lack of data (Figure 2.10).

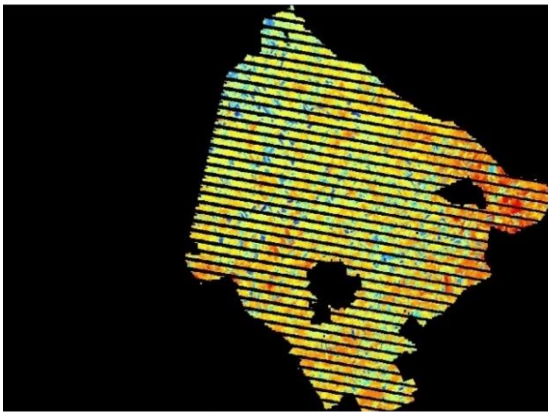

Figure 2.10 Image with strips of L7 satellite

- *Cropped images:* depending on the satellite orbit some days the images result partial, not all the basin area is captured (Figure 2.11).

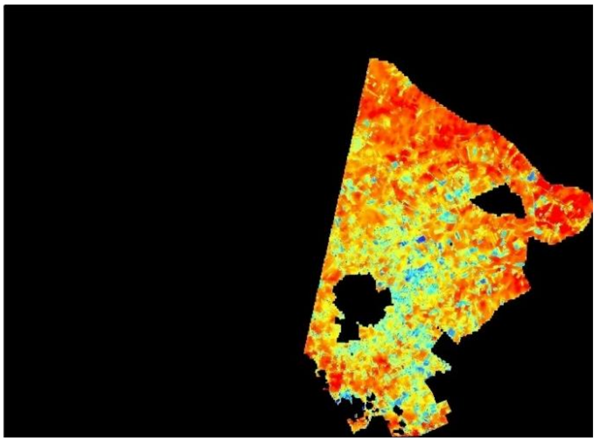

Figure 2.11 Cropped LST image

Satellite images from 2014 to 2019 are considered in the analysis.

2.2.4.2 MODIS

The LST values are retrieved using data collected during the daytime by MODIS on NASA's Terra satellite. MODIS Terra MOD09A1 Version 6 product provides an estimate of the surface spectral reflectance of Terra MODIS Bands 1 through 7 corrected for atmospheric conditions such as gasses, aerosols, and Rayleigh scattering.
The dataset provided contains daily series at 1 km of spatial resolution from the 1st January 2000 to 30th March 2020.

2.2.5 Precipitation

2.2.5.1 Ground Precipitation

Ground precipitation is measured by meteorological fixed station from Puglia ARPA and the stations installed in the consortium area (Figure 2.12) Averaged daily value at basin scale are available from the 1st January 2015 till the 31st December 2019.

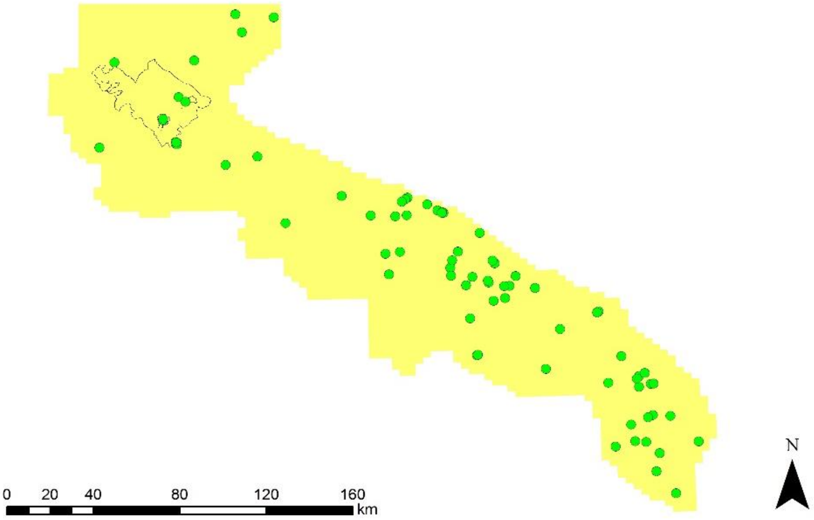

Figure 2.12 Meteorological stations distribution in the territory of Puglia with Consortium area highlighted

2.2.5.2 Precipitation from ERA5

Precipitation data for the long series analysis are extracted by ECMWF (European Centre for Medium-Range Weather Forecasts) ERA5 database. ECMWF uses its forecast models and data assimilation systems to reanalyze archived observations, creating global data sets describing the recent history of the atmosphere, land surface, and oceans. ERA5 provides hourly estimates of many atmospheric, land and oceanic climate variable, such as precipitation values. The data cover the Earth on a 30km grid and resolve the atmosphere using 137 levels from the surface up to a height of 80km. Mean daily data on basin area from the 1st January 2000 to 30th March 2020 are available.

Table 2.2 Summary of precipitation, soil moisture, land surface temperature and vegetation indices satellite dataset

	Source	**Dataset**	**Spatial Resolution**	**Temporal Resolution**
Precipitation	Fixed Stations	2015-2019	Basin scale	hourly
	ECMWF ERA5	2000-2020	Basin scale	daily
SM	ESA CCI Active	2000-2019	25km	daily
	ESA CCI Composite	2000-2018	25km	daily
	SMOS	2010-2020	50km	3days
	SMAP	2015-2020	40km	3 days
	Copernicus	2015-2018	1km	daily
LST	Landsat	2017-2019	30 m	8/15 days
	MODIS	2000-2020	1 km	daily
VIs	Landsat & Sentinel2 *(Fcover, NDVI, NDWI, MSAVI, MSI)*	2014-2019	30 m	8 days
	MODIS *(NDVI, NDWI, EVI, SAVI)*	2000-2020	500 m	8 days
			250 m	16 days

Chapter 3

Ground soil moisture and vegetation indices

In the first part of the thesis spot analysis of observed soil moisture series is carried out. Sensors with high spatial distribution, installed in cultivated field, independently managed, are used for retrieving daily and hourly soil moisture values. Then, continuous soil moisture series are extracted by fixed monitoring stations located in the study area. A research for new parameter or threshold useful in irrigation control is developed. Investigating the ability to capture water stress condition, satellite images of vegetation indices and land surface temperature are considered. At the end, relationship between the variable involved is performed at field scale.

3.1 Sensor in tomato fields

The first step is the analysis of sensors in tomato fields. Tomatoes are sown in spring, grown during summer are harvested between the end of August and the begin of September. So, the analyzed period (22nd of July - 20th of October) corresponds to the growing and harvesting season. Seven tomato fields with 13 working sensors (coordinates in Table 3.1) are investigated, four are located in the eastern part of consortium area and three in the southern. The fields with the corresponding sensors are summed up in Table 3.2.

Table 3.1 Tomato sensors coordinates in UTM 33N

Sensor Code	Coordinates UTM 33N	
	X (est)	Y (nord)
EC9F	557014.8805	4589459.935
EB70	557133.8239	4588889.09
878A	560158.5387	4592706.32
EB04	560111.3962	4592652.634
EB1F	560124.3257	4592603.89
EB8F	560113.7515	4592608.308
EC5F	559512.6468	4592691.217
ED20	560377.6273	4593064.547
91C9	551150.8549	4579238.5126

849E	551167.1206	4579304.1308
ED40	552518.6747	4579319.3449
E864	552559.1344	4579391.8031
7FA0	551266.3162	4577353.7206

Table 3.2 Tomato sensors codes and their fields of installation

Eastern tomato field	**Sensor code**
A	EC9F
	EB70
B	878A
	EB04
	EB1F
	EB8F
C	EC5F
D	ED20

Southern tomato field	**Sensor code**
E	91C9
	849E
F	ED40
	E864
G	7FA0

At the time of setting up the tomato fields have medium/high fractional cover as we can see in Figure 3.1 and Figure 3.2, satellite image of Fcover on 22nd of July is represented. During the last survey Figure 3.1 and Figure 3.2, the sensors are in bare soil, satellite image of Fcover on 10th of October is represented.

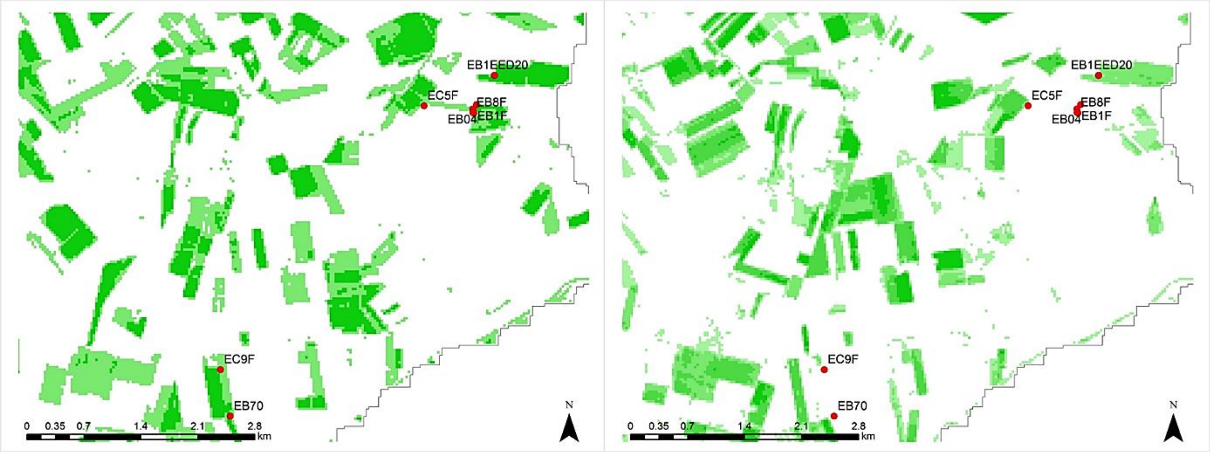

Figure 3.1. Eastern fields with sensors on 22nd of July (on the left) and on 10th of October (on the right)

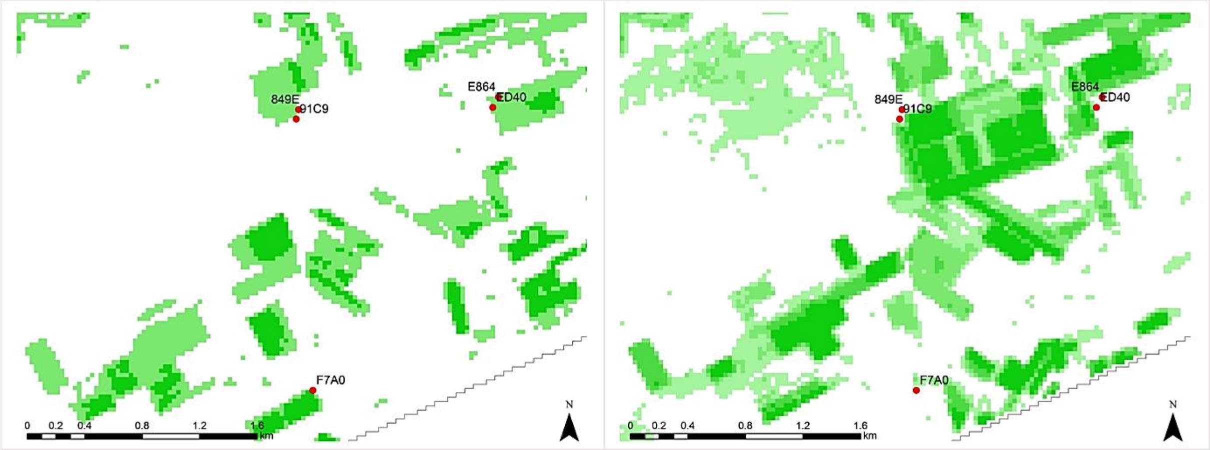

Figure 3.2 Southern fields with sensors on 22nd of July (on the left) and on 20th of October (on the right)

3.1.1 Soil moisture time series

The soil moisture time series for sensors, clustered according to the belonging field, are visible in Figure 3.3. Due to the lack of data between 28th July and 11th August, soil moisture series are shown in most significant period for the analysis (11th - 30th August).

The area is highly irrigated, each peak in soil moisture series corresponds to irrigation, values of soil moisture around 30-40% are observed.

As mentioned before, each field is independently managed by the farmers, this is confirmed by different frequencies and time of irrigation application (Table 3.3)

Table 3.3 Number of irrigations applied on tomato fields

Field	A	B	C	D	E	F	G
N° of irrigations	14	7/11	19	7	10	4	7

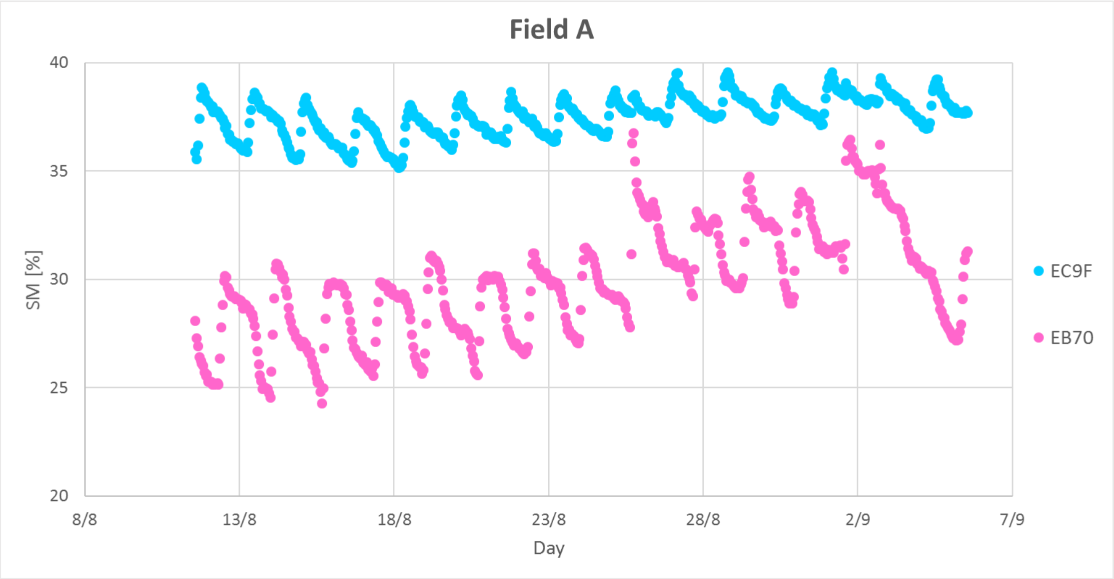

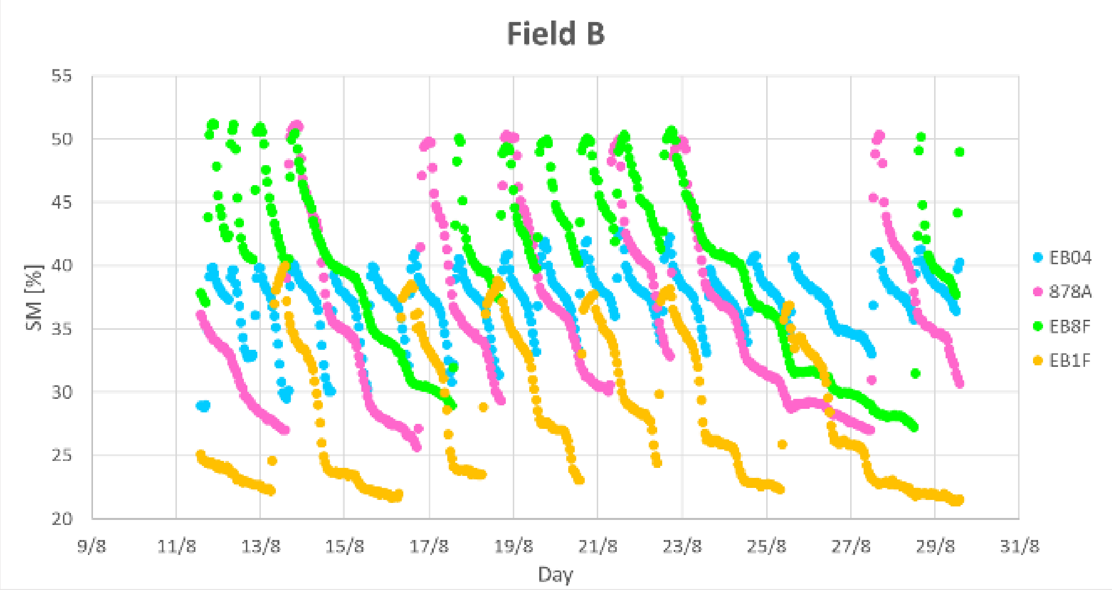
Field B
55
50
45
40
35
30
25
20
SM [%]
9/8
11/8
13/8
15/8
17/8
19/8
21/8
23/8
25/8
27/8
29/8
31/8
Day
● EB04
● 878A
● EB8F
● EB1F

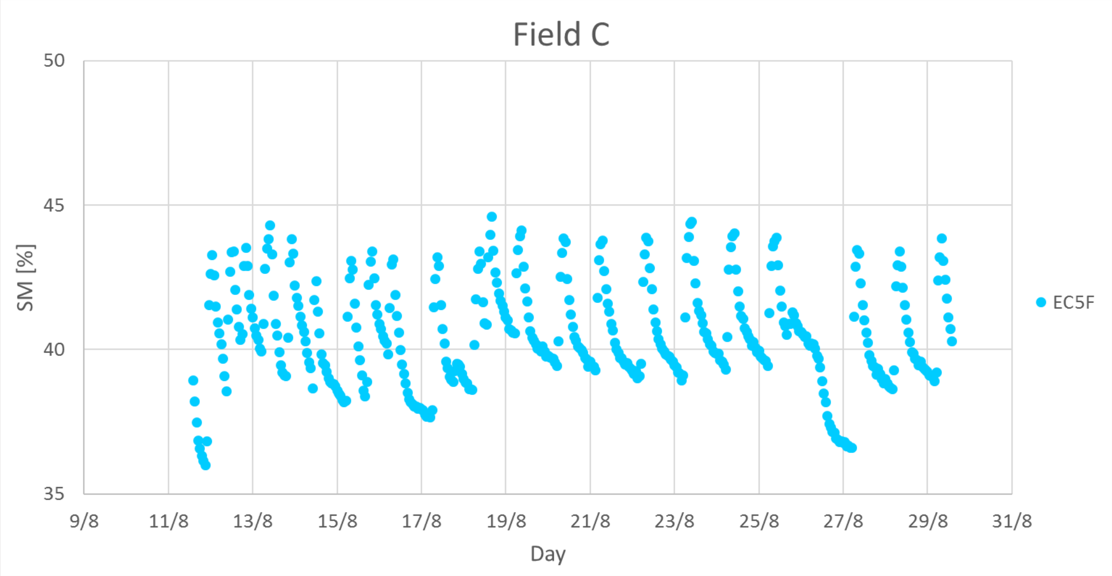
Field C
50
45
40
35
SM [%]
9/8
11/8
13/8
15/8
17/8
19/8
21/8
23/8
25/8
27/8
29/8
31/8
Day
● EC5F

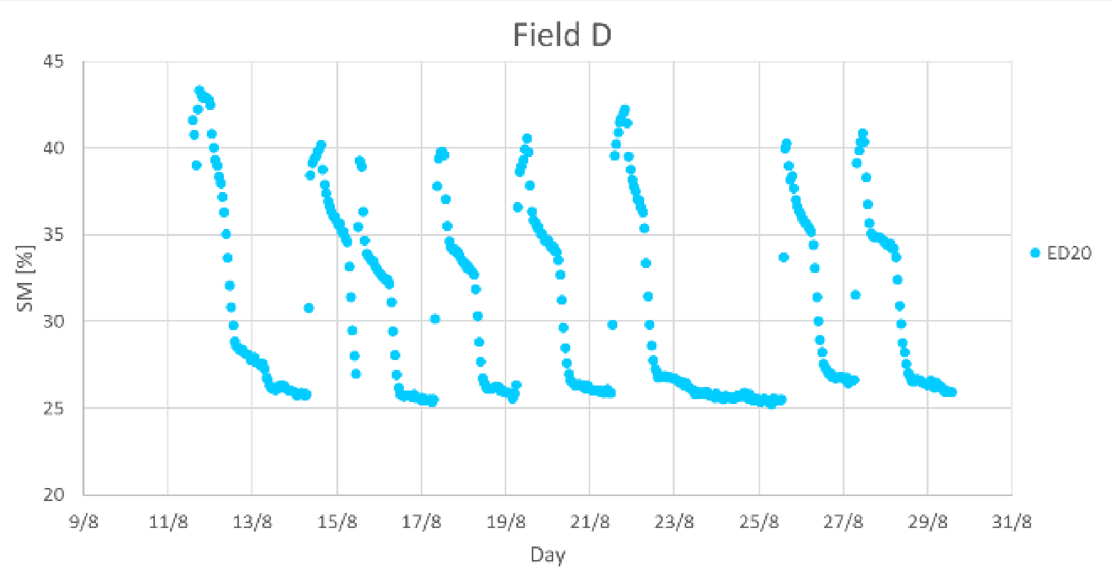
Field D
45
40
35
30
25
20
SM [%]
9/8
11/8
13/8
15/8
17/8
19/8
21/8
23/8
25/8
27/8
29/8
31/8
Day
● ED20

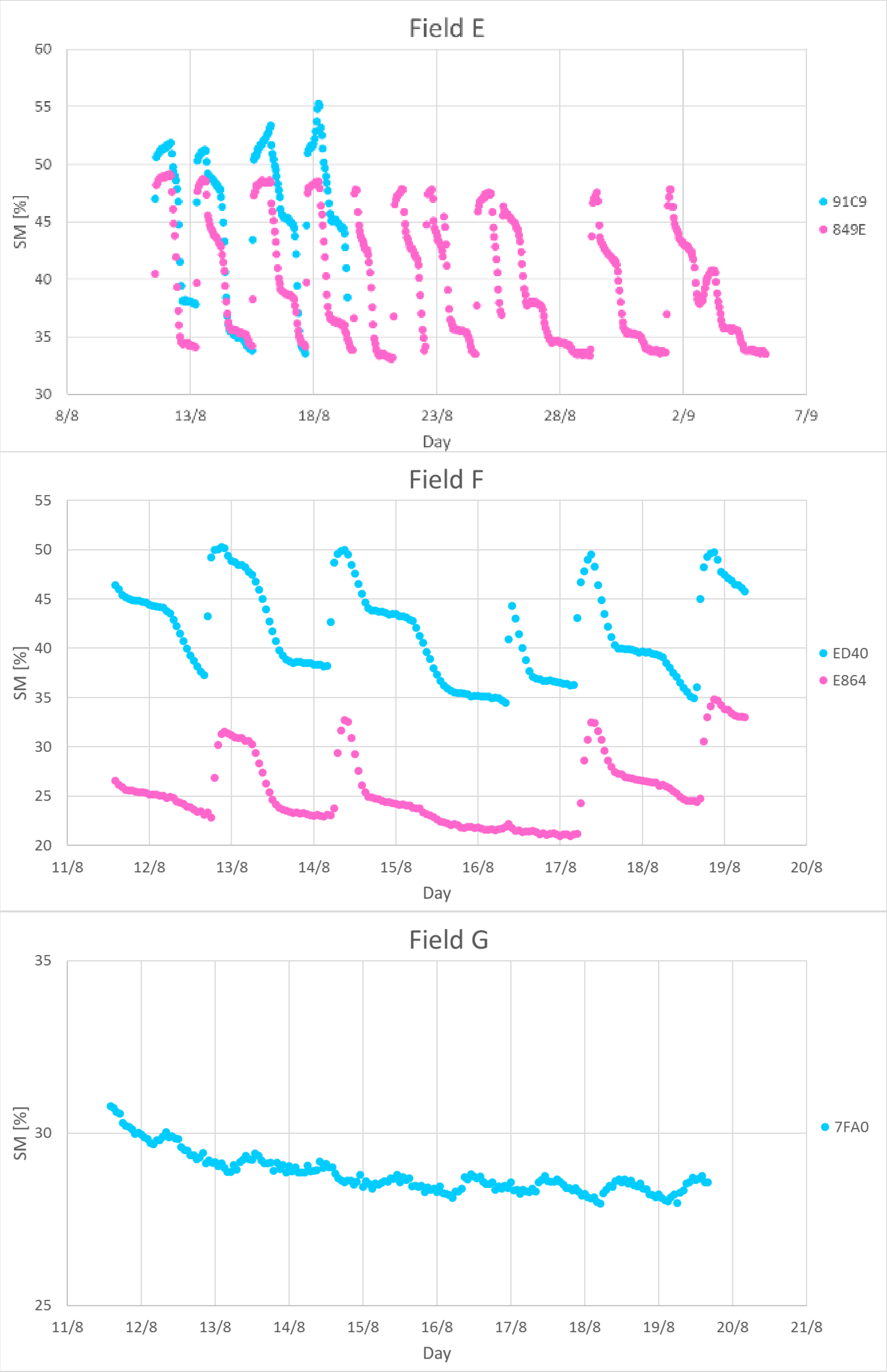

Figure 3.3 Soil moisture time series of GROW sensors

3.1.2 Soil moisture and vegetative indices

The following analysis aims to understand if crop stress conditions can be detected through vegetative indices, and if these indices could be used for the definition on a new water stress threshold for irrigation. Indeed, up to now irrigation thresholds involve parameters such us the wilting point and the field capacity.

Considering the coordinates of each sensor the corresponding vegetative indices values are extracted from satellite images. Landsat (L7 and L8) satellite images are used for retrieving Fcover, MSAVI, NDVI, NDWI values, the available dates are visible in Table 3.4.

Table 3.4 Satellite images used for vegetation parameters recovering

Satellite images days										
22/07	27/07	16/08	26/08	31/08	5/09	20/09	25/09	30/09	10/10	20/10

Therefore, for each sensor soil moisture values corresponding to these 11 dates are related with the values of vegetative indices. Due to lack of data in soil moisture series, not for all the dates soil moisture is available.

As we can see in Figure 3.4, in the early period tomatoes have high values of Fcover , NDVI, NDWI and MSAVI and medium of SM, since the plats are irrigated, then during the growth the indices increase them values, till the end of August when the tomatoes are harvested and all the indices return to zero.

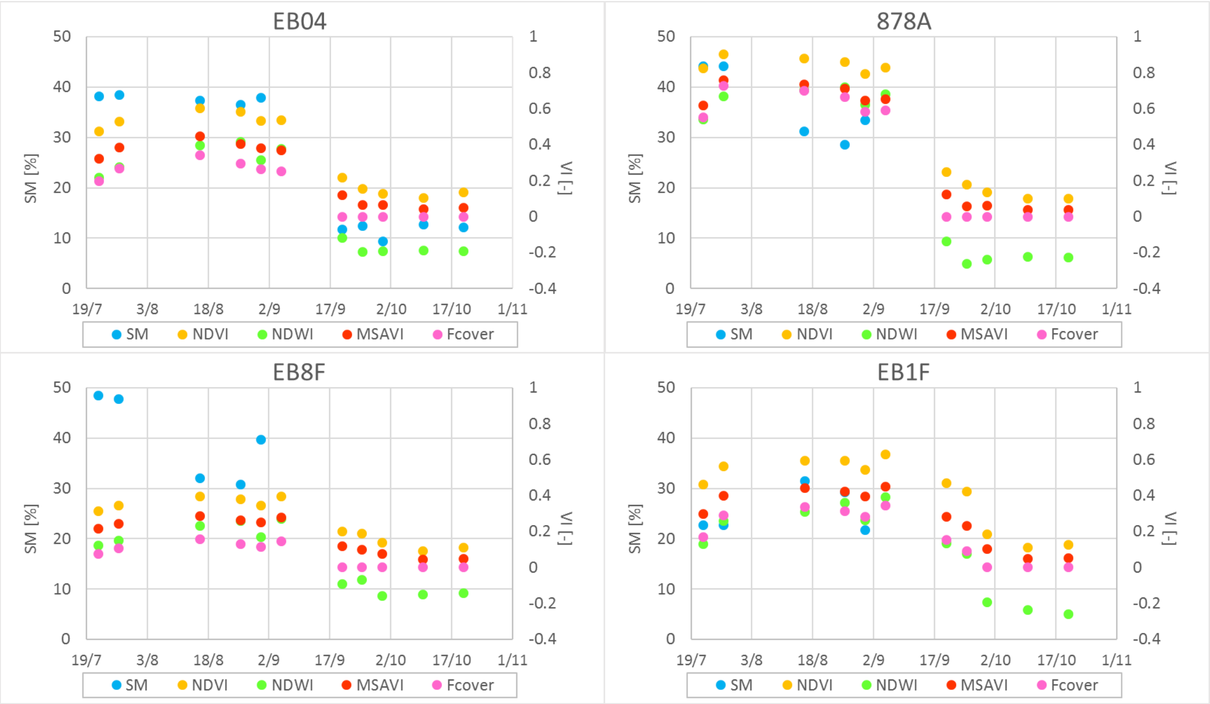

Figure 3.4 Soil moisture, vegetative indices of sensors in tomato fields

3.2 Sensors in asparagus and other vegetables fields

The second step is the analysis of fields, cultivated with asparagus, cabbage, fennel, celery, lettuce. These crops have a different growing and harvesting season.

Asparagus are plurennial crop, harvested in from March to June. Thus, during the analyzed period the asparagus field are cultivated, and the plants are growing. Generally, drip irrigation is performed, to minimize water losses. Being irrigated in deep the sensors, that detect soil moisture in the first 5-10 cm, could not capture the real soil moisture values.

While crops such as fennel, cabbage, lettuce grow from the beginning of September and are harvested from November. The growth from small irrigated plants to vegetables ready for the harvest is monitored by sensors. Some fields are harvested during the analyzed period, hence bare soil is detected at in the last period.

Among the 145 working sensors, 23 are installed in asparagus fields and 42 are in fields of other vegetables. The same analysis, as for tomatoes fields, are carried out. In figure 3.5 and 3.6, four sensors of asparagus field and two of vegetables (one of cabbage and one of celery) are shown, their coordinate are reported in Table 3.5.

As we can see in Figure 3.5, in asparagus field the vegetative indices keep constant during all the period and soil moisture values are around 30% with some peak due to irrigation. In vegetable fields, the sensor 86D2 shows till September not irrigated bare soil (low SM and low VI) and then the spring up of the crop. Instead, the sensor 8C2C shows high values of soil moisture above all the period and an increasing in VI, evidence of the growth from small irrigated plants (high SM and low VI) to bigger ones (high SM and high VI). No information on water stress can be retrieved due to the low amount of available data.

Table 3.5 Vegetables sensors coordinate in UTM 33N

Sensor Code	**Coordinates UTM 33N**	
	X (est)	**Y (nord)**
EFDB	552016.3176	4578572.9799
EFEB	560582.0368	4592980.7684
F070	551981.1860	4578572.7281
E9B4	551414.3538	4578128.6021
86D2	551884.0104	4578958.5832
8C2C	552202.0364	4577591.772

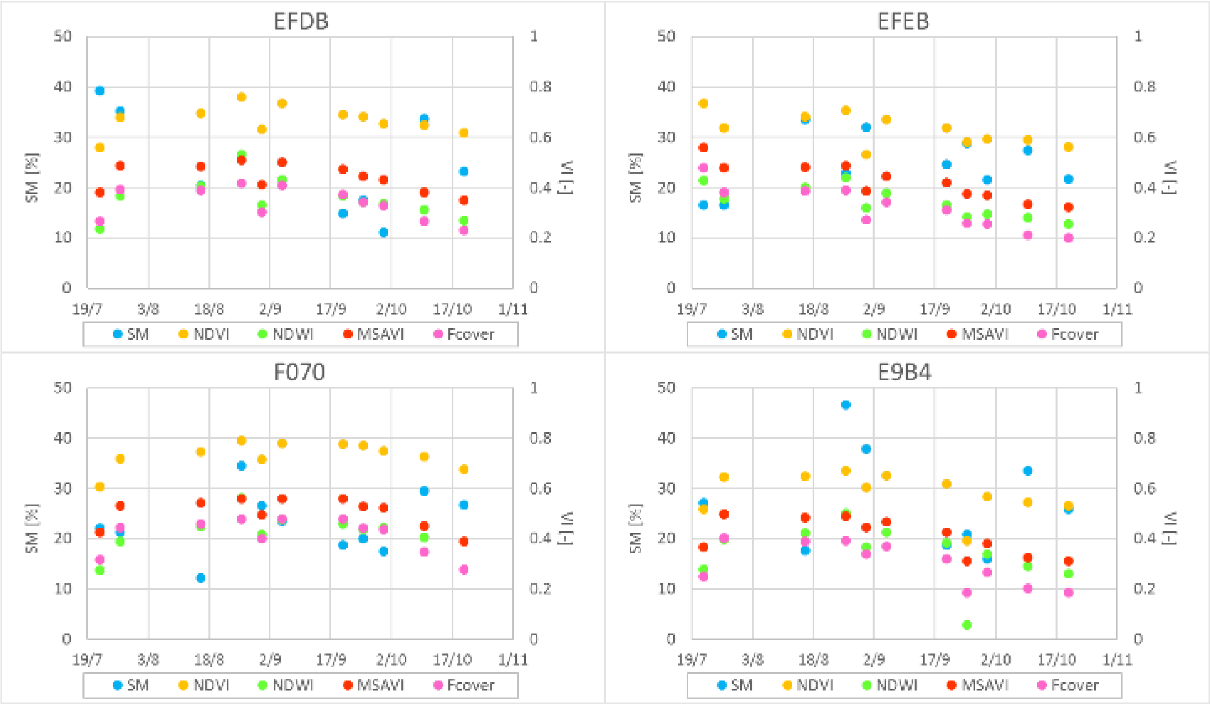

Figure 3.5 Soil moisture and vegetative indices of sensors in asparagus fields

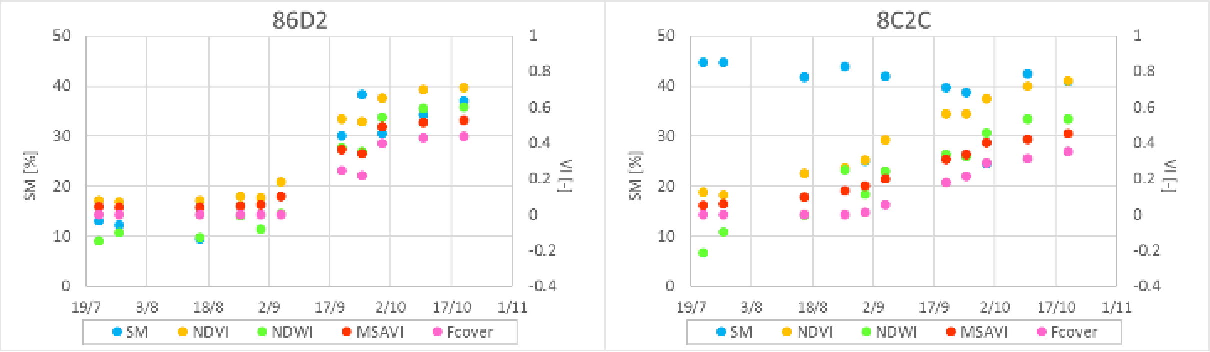

Figure 3.6 Soil moisture and vegetative indices of sensors in vegetable fields

3.3 Fixed monitoring station

Considering low amount of data available from the low cost station is not possible to retrive any other information regarding stress conditon from sensors measuremets. Thus, to perform a more reliable analysis soil moisture from sensors is supported with soil moisture series detected by continuous monitoring eddy covariance stations.

Onoranza filed is cultivated with tomatoes, while De Filippo field is cultivated in the first period with tomato and during the second year with wheat. The coordinate of the center of the field are shown in Table 3.6. As was done for sensors, vegetative indices referred to the central pixel of the fields, are extracted from Landsat and Sentinel2 satellite images. For De Filippo field, only half of the field is cultivated with tomato, as we can see in Figure 3.7, so the coordinate used to retrieve vegetation parameters are related not to the center of the field (orange point) but to the left part.

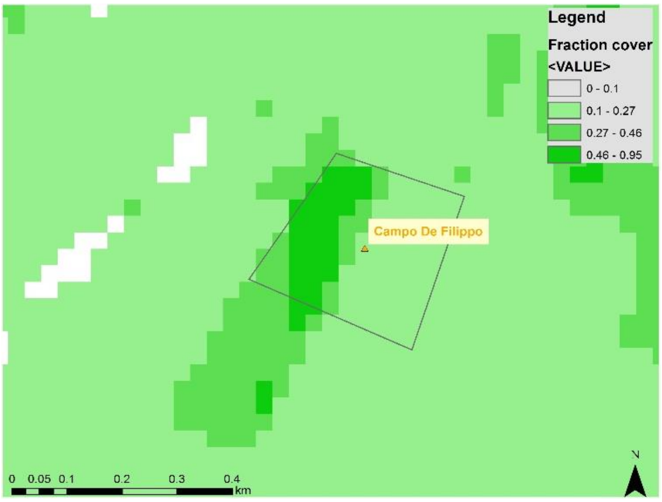

Figure 3.7 De Filippo field during tomatoes cultivation

Table 3.6 Coordinate of field with monitoring stations

Field	Coordinates UTM 33N	
	X (est)	**Y (nord)**
Onoranza	556960.186312	4589173.13454
De Filippo Wheat	556292.47552	4598025.92871
De FilippoTomato	556243.988	4598049.134

The tomato fields are highly irrigated, as we can see from the soil moisture trend no stress condition is reached (Figure 3.8 and 3.9). Fraction cover and the others vegetative indices follow the same behavior, initial growth and then almost constant values, according to irrigation application and crop growth.

Wheat grows in winter and is harvested in June. Two different stages are visible in Figure 3.10. From January to April vegetative indices increase them values following the spring up of the crop. High values of fraction cover (around 1) are reached due to the high density of the grain. Then in May, the grain matures, becoming yellow and no irrigation is applied. The yellowing involves a decrease in NDVI values (from green to yellow band) but the faction cover remains still high. MSAVI and NDWI, following the same trend of NDVI, do not provide any further information about the crop healthy state. Probably having higher amount of satellite data exactly before and after an irrigation event information on water stress could have been retrieved.

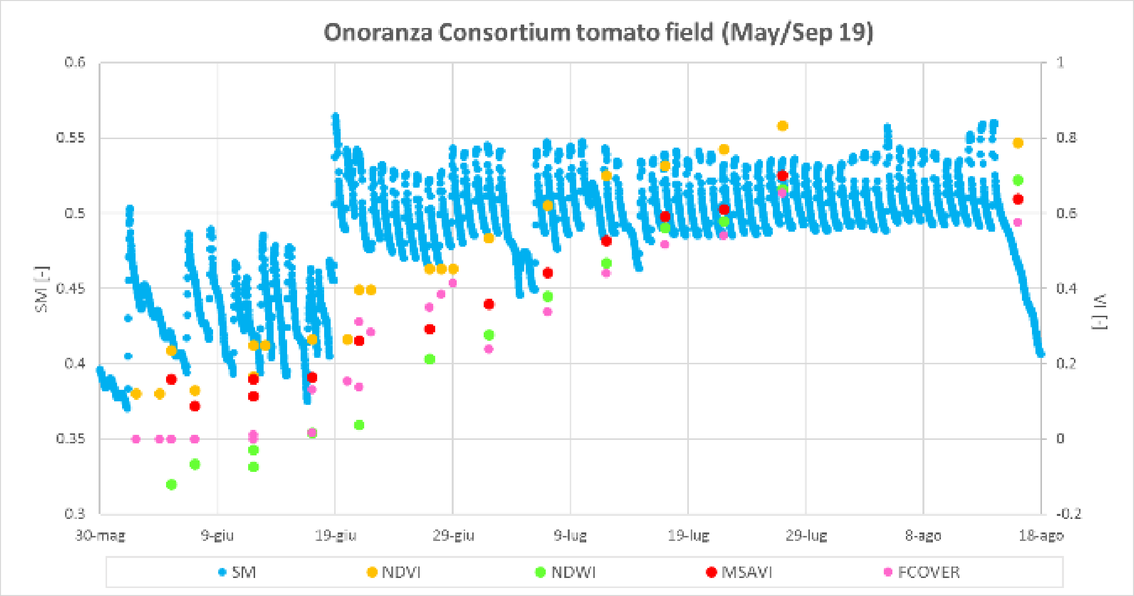

Figure 3.8 Soil moisture and vegetative indices of Onoranza Consortium tomato field

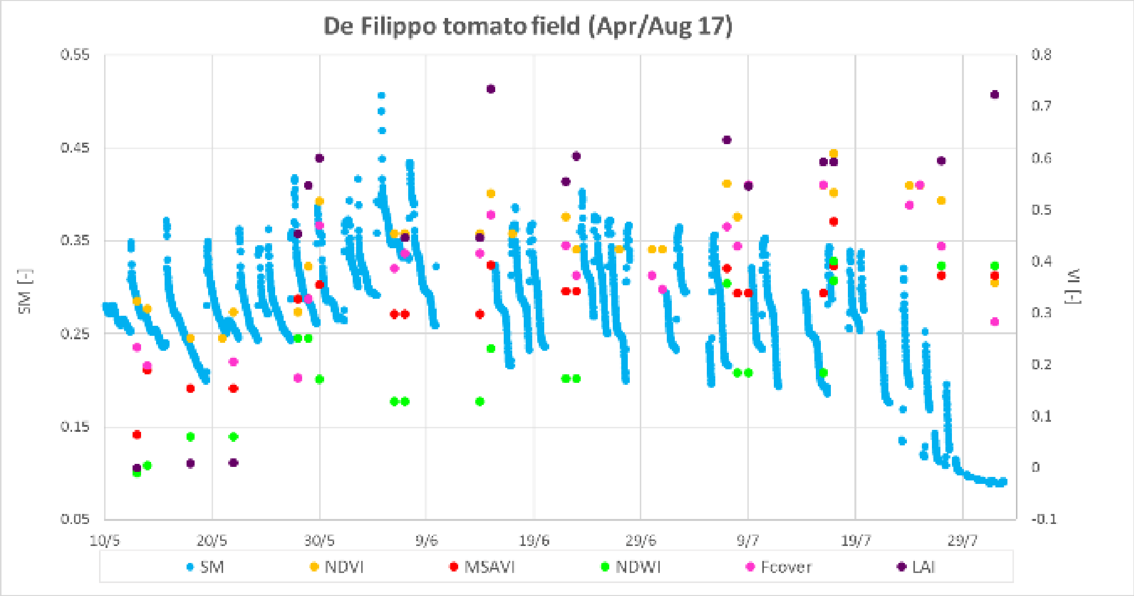

Figure 3.9 Soil moisture and vegetative indices of De Filippo tomato field

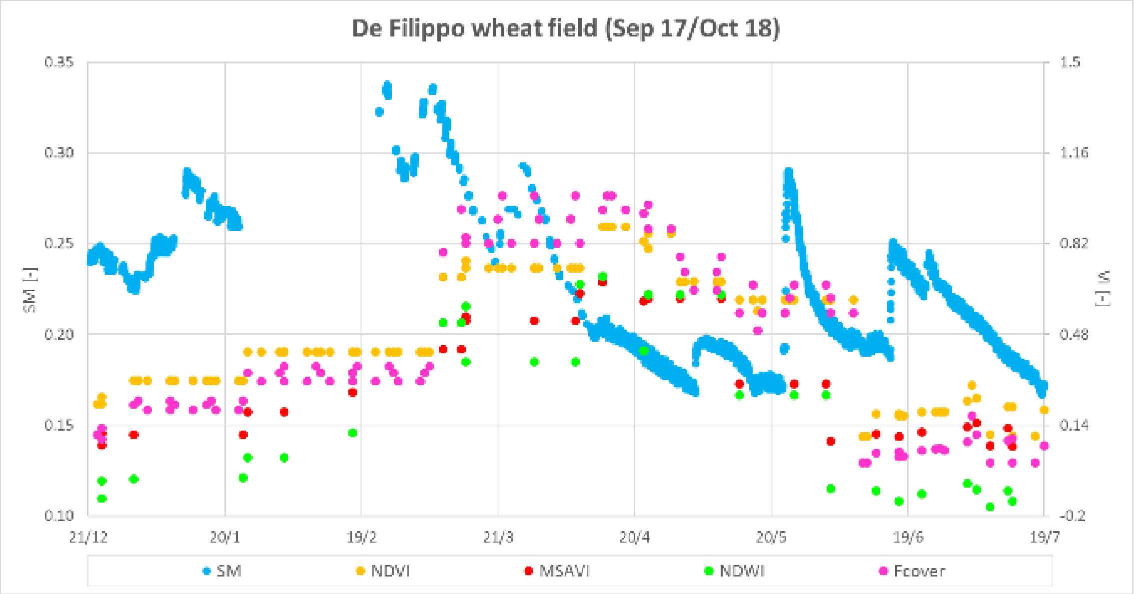

Figure 3.10 Soil moisture and vegetative indices of De Filippo wheat field

3.3.1 Temporal correlations

Correlations between soil moisture, vegetative indices and land surface temperature are computed using Pearson’s correlation coefficient. These correlation coefficients are computed in order to detect the influence of soil moisture on crop status.

Soil moisture and NDVI correlation is performed for all the fields calculating the coefficient using all the dates for those NDVI satellite images are available. While, LST-NDVI and LST-SM correlation are computed only for De Filippo field and not for Onoranza, because not enough LST images of good quality (without clouds, strips, cut) are available for the 2019. The results are shown in Table 3.7. High soil moisture values mean wet soil due to irrigation or precipitation, hence a healthy state of the crop (medium/high NDVI) should be observed. Clearly SM and LST are inversely correlated so if SM-NDVI correlation provide positive values LST-NDVI is the opposite. The response of vegetation health may be delayed with respect to soil moisture increasing, meaning that irrigation/precipitation of the day considered can results in vegetation improvement some time later. This delay must be taken into account in correlation values between SM/LST and vegetative indices, such NDVI. Indeed, if SM and LST are highly correlated, SM/LST and NDVI relationship show lower values.

Table 3.7 Pearson correlation coefficients between SM, LST and NDVI

Field	**SM-NDVI**	**LST-SM**	**LST-NDVI**
Onoranza Consortium	0.33	-	-
De Filippo Tomato	0.11	-0.24	-0.18
De Filippo Wheat	0.18	-0.60	-0.32

Chapter 4

Hydrological Model validation

In this chapter the results of the validation of hydrological model FEST-EWB are presented. The simulation is carried out in the period 2015-2019, statistical indices are calculated to estimate the errors of the model with respect to remote sensing LST observed data and ground eddy covariance data. Spatial autocorrelation and temporal correlations are calculated to assess the spatial distribution of the simulated variables and their relationships.

4.1 Comparison between observed LST and simulated RET

The results of the model are in term of SM, ET and RET distributed maps and averaged values at basin scale from January 2015 to September 2019. The first analysis carried out is the comparison between observed data and simulated ones. Land surface temperature maps, from L7 and L8, e.g. the observed data are compared with RET maps and statistical indices are evaluated. The trend of RET and LST and the seasonal average are shown in Figure 4.1 and Table 4.1, and the absolute mean bias errors are presented in Figure 4.2. As we can notice in some summer days the model underestimates the observed temperature while in winter an overestimation is observed. Furthermore, the comparison between LST maps on the right and RET maps on the left are shown in Figure 4.3.

Table 4.1 Average temperature of LST and FEST

	Average temperature	
	Winter	**Summer**
Observed LST (C°)	18.7	42.6
Simulated RET (C°)	21.7	39.2

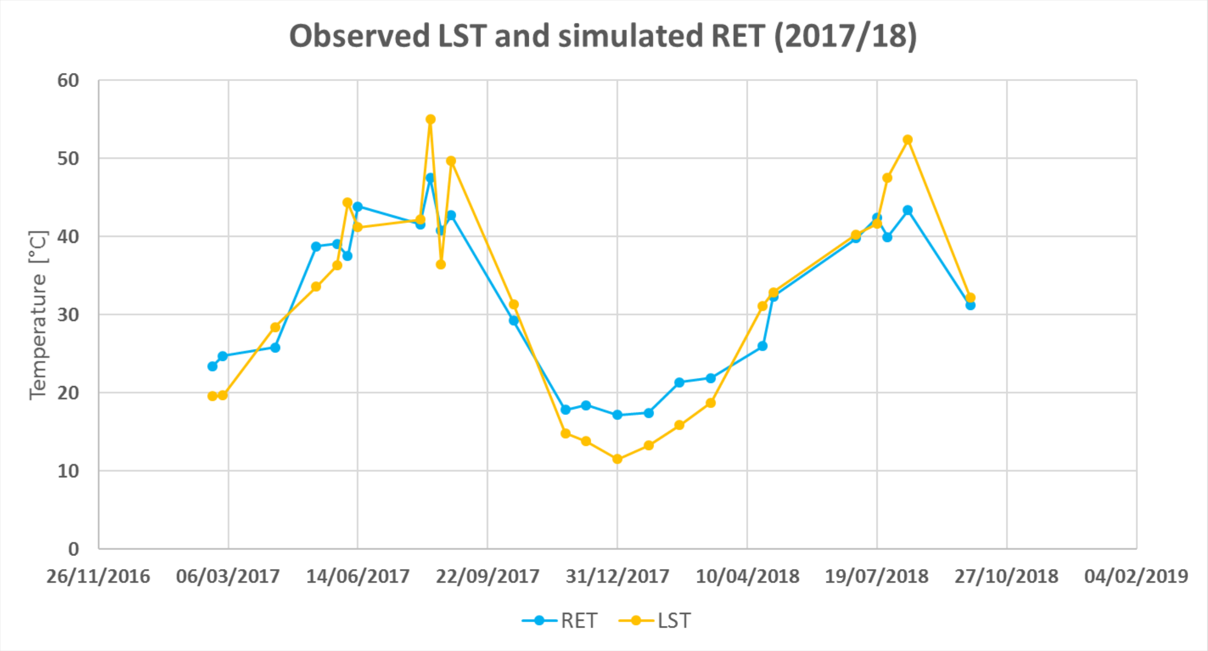

Figure 4.1 Trend of observed LST and simulated RET

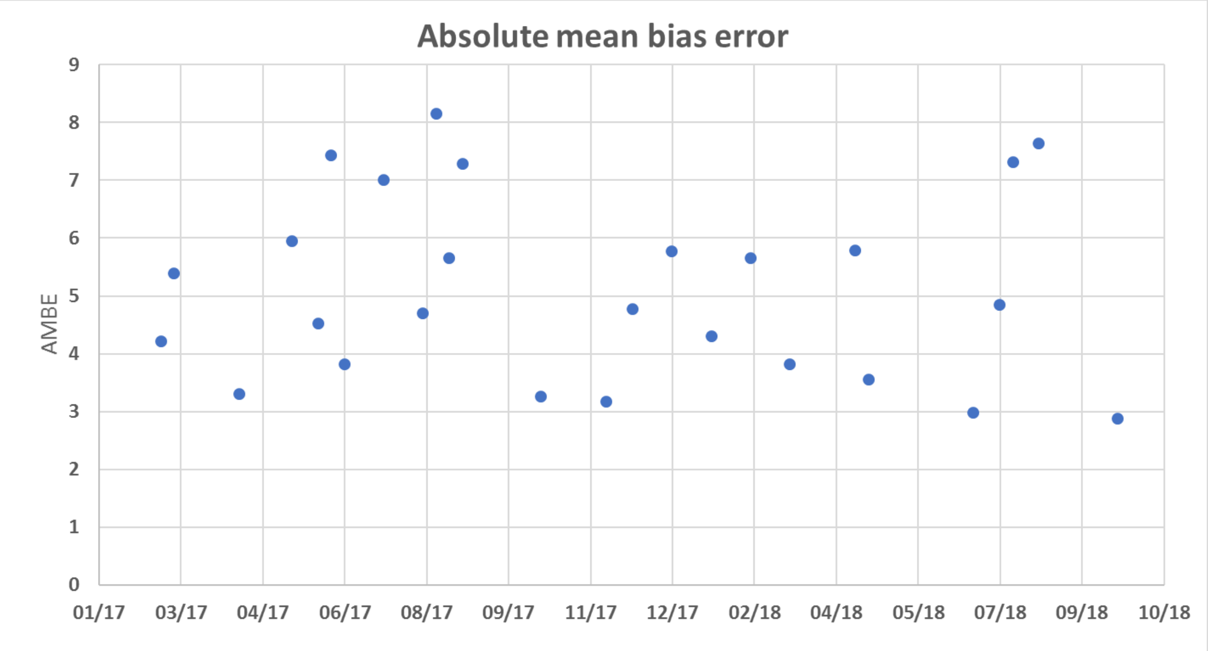

Figure 4.2 AMBE between simulated RET and observed LST from Landsat images

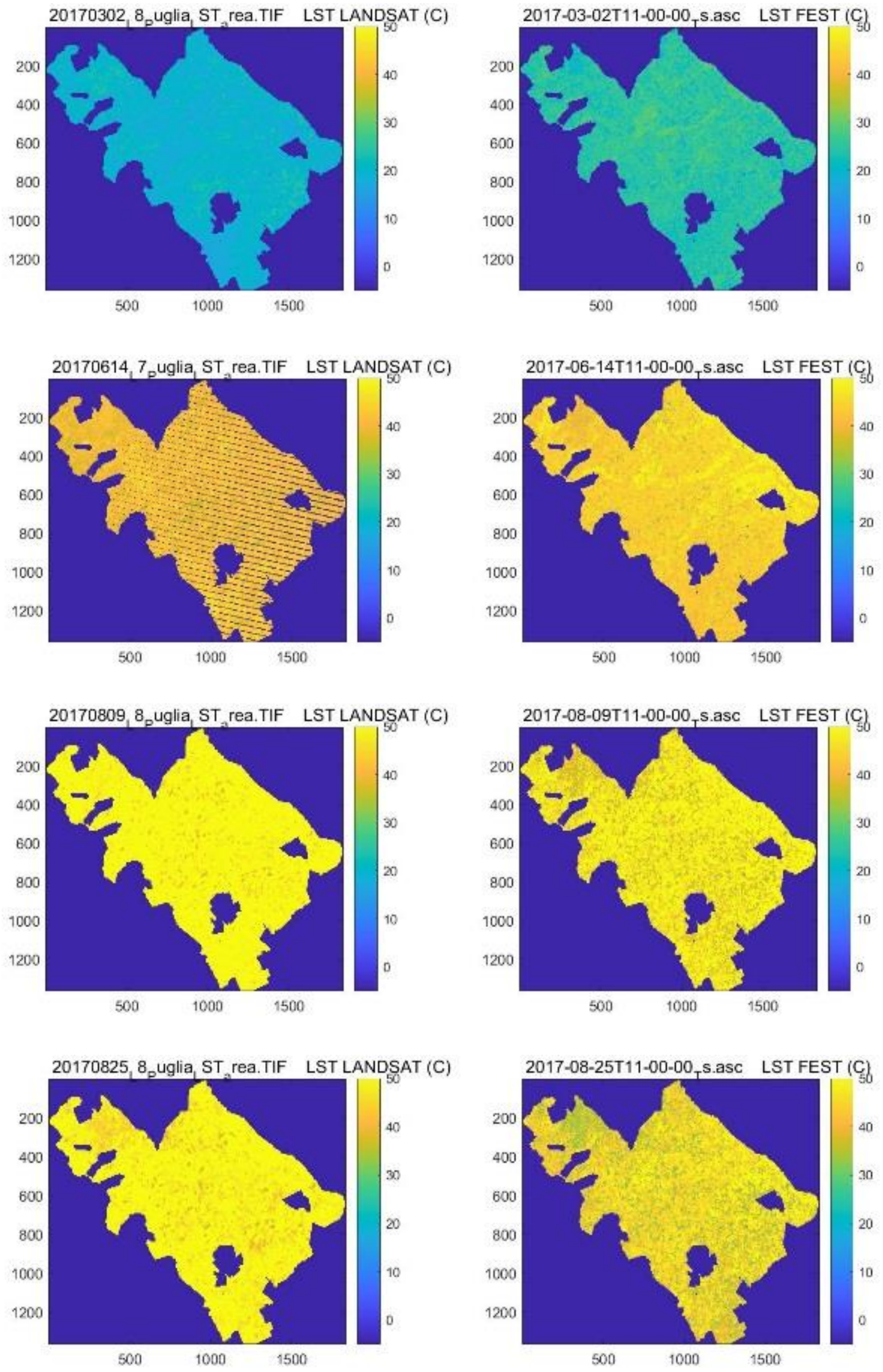
20170302$_L$8$_P$uglia$_L$ST$_a$rea.TIF LST LANDSAT (C)
2017-03-02T11-00-00$_T$s.asc LST FEST (C)
20170614$_L$7$_P$uglia$_L$ST$_a$rea.TIF LST LANDSAT (C)
2017-06-14T11-00-00$_T$s.asc LST FEST (C)
20170809$_L$8$_P$uglia$_L$ST$_a$rea.TIF LST LANDSAT (C)
2017-08-09T11-00-00$_T$s.asc LST FEST (C)
20170825$_L$8$_P$uglia$_L$ST$_a$rea.TIF LST LANDSAT (C)
2017-08-25T11-00-00$_T$s.asc LST FEST (C)
200
400
600
800
1000
1200
500
1000
1500
50
40
30
20
10
0

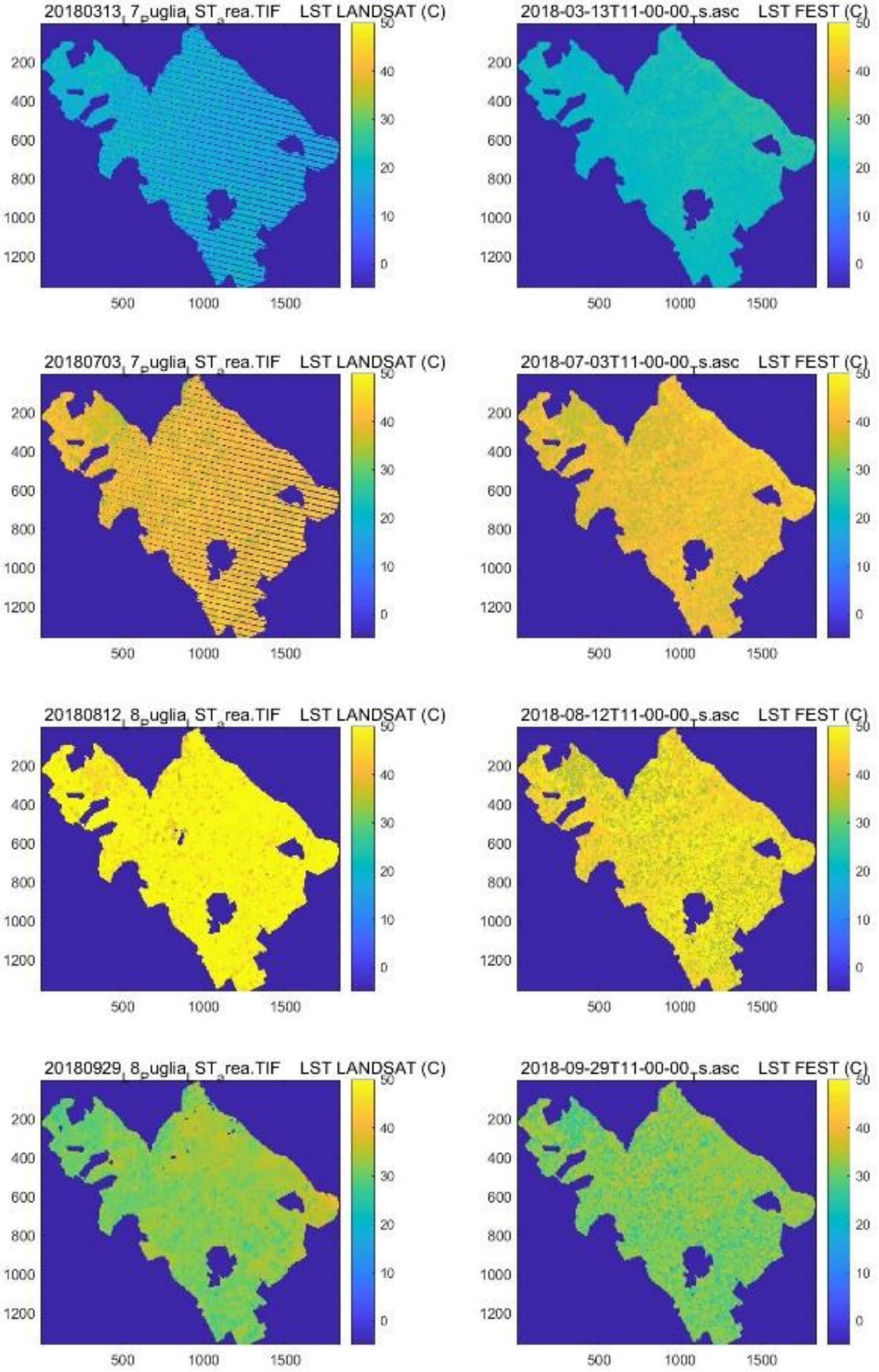

Figure 4.3 Comparison between maps of LST from Landsat and RET from FEST-EWB

4.1.1 Spatial autocorrelation

Autocorrelation curves are calculated for simulated variables, such us ET, RET and SM, for NDVI, LST satellite images and for soil parameters maps, such us FC and K_{sat}.

As we can see in Figure 4.4, ET, RET, SM, NDVI and LST autocorrelation curves show the same trend both for winter and summer period. So, the correlation between pixels keep constant values that means that the fields do not change their shape during the year.

Then, the consistency between RET and satellite LST confirm the ability of the FEST-EWB model to reproduce the correct shape of the fields. Instead, FC and K_{sat} autocorrelation show less correlation probably due the spatial heterogeneity of the soil parameters.

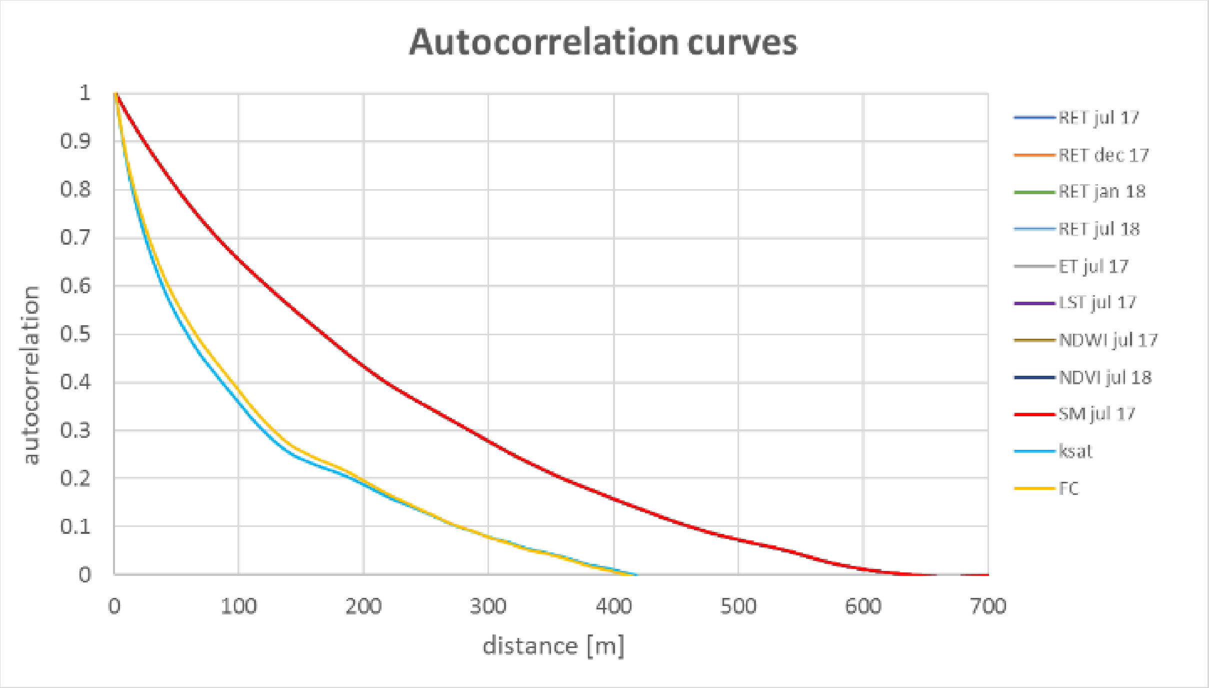

Figure 4.4 Autocorrelation curves of hydrological variables and soil parameters

4.1.2 Temporal correlations

Correlation between SM, ET and RET maps retrieved from the model and the Landsat satellite images of NDVI and LST are computed. A 3D matrix is built stacking the maps of the variable on the dates chosen: in this way giving a (x, y) position is possible to extract all the values in the z direction so that a vector containing the time evolution of the variable is obtained. Each pixel (x, y) of the correlation map is a Pearson correlation coefficient, which is calculated by using the time evolution vectors in position (x, y) of the two variables to be correlated. That means, that the time evolution of a variable in each pixel is correlated with the time evolution of another variable in the same pixel. Thus, each pixel of the correlation map represents the temporal correlation of the chosen variables, i.e. LST and NDVI. Correlation maps are calculated for 2017 and 2018 subdividing winter and summer period, considering Fcover higher than 0.1. Dates used for the correlations are visible in Table 4.2 and 4.3.

Table 4.2 Dates used for temporal correlation year2017

	Correlation 2017							
Summer	29 May	6 Jun	14 Jun	8 Jul	1 Aug	9 Aug	17 Aug	25 Aug
Winter	22 Feb	2 Mar	21 Nov	7 Dec	12 Dec			

Table 4.3 Dates used for temporal correlation year 2018

	Correlation 2018					
Summer	30 Apr	3 Jul	11 Jul	19 Jul	27 Jul	12 Ago
Winter	24 Jan	17 Feb	13 Mar			

In Table 4.4 the interpretations of Pearson’s correlation coefficients sign between the variables in rows and columns are shown. Depending on the variable being correlated the sign of Pearson’s coefficient (positive/negative) could indicate the fields being irrigated or not.

Table 4.4 Pearson's coefficient signs and their interpretation

Correlation (no irrigation /irrigation)	**ET**		**SM**		**NDVI**	
RET	+ No Irr.	- Irr.	+ No Irr.	- Irr.	+ No Irr.	- Irr
LST	+ No Irr.	- Irr.	+ No Irr.	- Irr.	+ No Irr	- Irr.
NDVI	+ Irr.	- No Irr.	+ Irr.	- No Irr		

Figure 4.5 show correlation between NDVI, RET and LST for summer, only cultivated field, Fcover>0.1 on the 25th of August, are considered, then a zoom (Figure 4.6) at field scale is reported in figure.

Fields that show negative correlation (blue fields) can have high values of NDVI and low values of LST/RET that indicates irrigated vegetation (high values of SM), or low values of NDVI and high values of LST/RET that indicate bare soil (low values of SM). While, fields that shows positive correlation (red fields) have high values of NDVI and high values of LST/RET representative of not irrigated crops or brushwood of wheat or trees, such as olives.

Furthermore, making a comparison between summer and winter correlation, opposite behaviour is observed. LST (or RET) and ET show positive correlation in winter and negative in summer, indeed high values of evapotranspiration means healthy state of the crop that in summer means irrigation, low temperature and high SM (Figure 4.7). This comparison prove that the model is able to simulate the irrigation and the spatial variability of the fields.

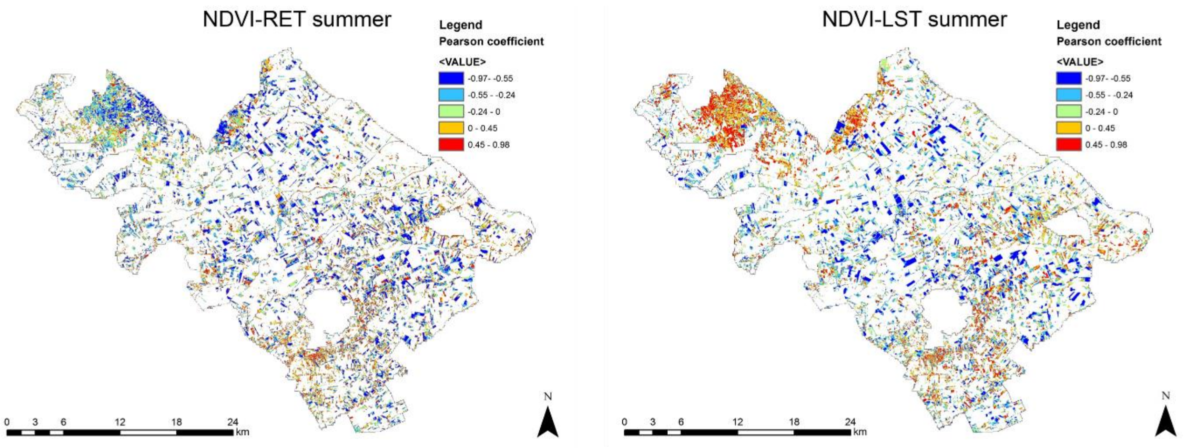

Figure 4.5 NDVI-RET and NDVI-LST correlation maps

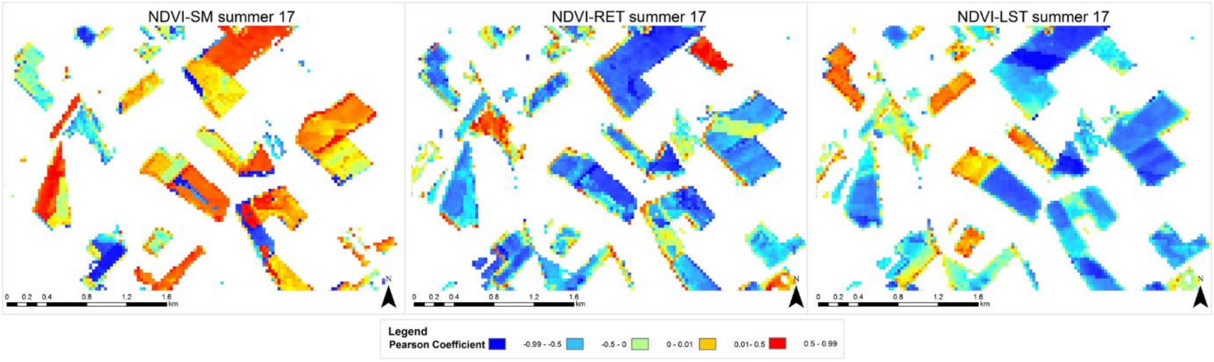

Figure 4.6 Zoom at field scale of NDVI-SM, NDVI-RET, NDVI-LST correlation maps

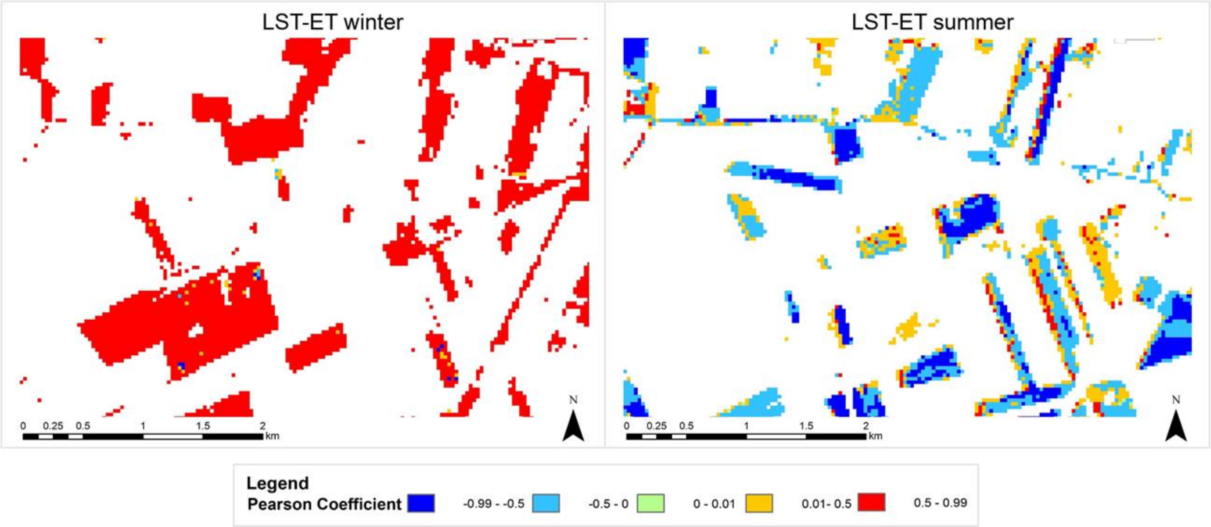

Figure 4.7 Comparison at field scale of LST-ET correlation maps in winter and summer period

4.2 Spatial LST – NDVI relationship

The relationship between LST and a VI, is also analysed, which is of interest for understanding crop stress.

The shape in the LST – VI feature space results to be a triangle (or trapezoid) (Figure 4.8), because of the low sensitivity of LST to soil moisture variations over vegetated areas, and an increased sensitivity (and thus greater spatial variation) over areas of bare soil ((Petropoulos, Carlson, Wooster, & Islam, 2009). The basis (wet edge) corresponds to the set of cooler pixels that have varying amounts of vegetation cover and have the maximum soil water content. Variation along the left edge of the triangle is assumed to reflect the combined effects of soil water content and topography variations across areas of bare soil. The remaining points within the triangular space correspond to pixels with varying vegetation cover, somewhere between bare soil and dense vegetation. For pixels with the same VI, those with minimum LST represent the case of the strongest evaporative cooling, while those with maximum LST represent those with the weakest evaporative cooling. Hence, the triangle’s (or trapezoid’s) ‘dry edge’ is considered to represent the upper limit of evaporation for the different vegetation conditions.

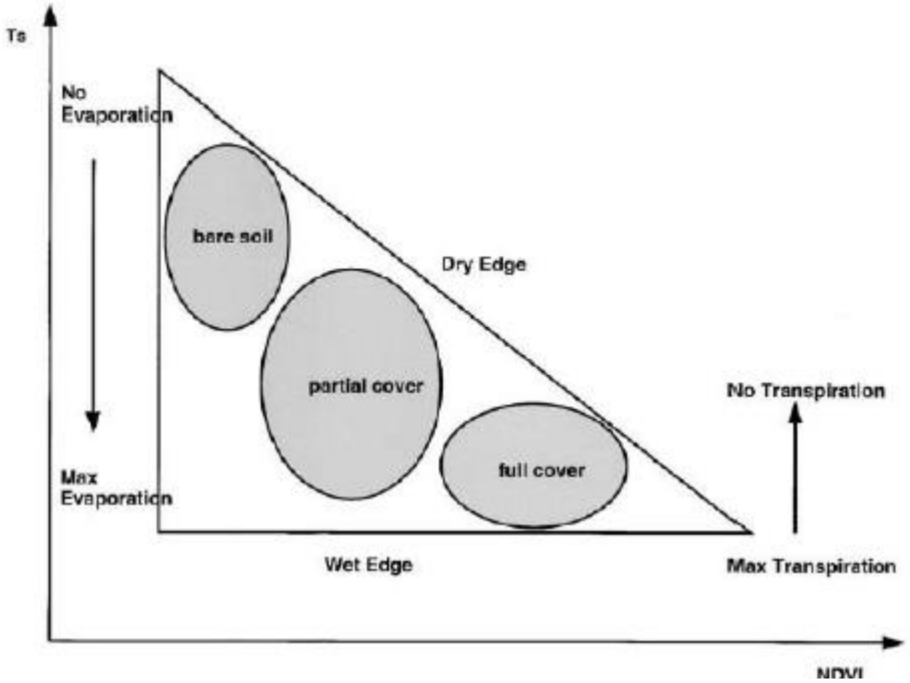

Figure 4.8 Spatial LST-NDVI relationship

The LST-NDVI and RET-NDVI relationship are calculated for the period of simulation. LST and NDVI values are extracted by Landsat satellite images, in Table the selected dates are visible. As we can see, some days are more spread than others but overall, all the plots show the typical shape of LST-NDVI relationship (Figure 4.9).

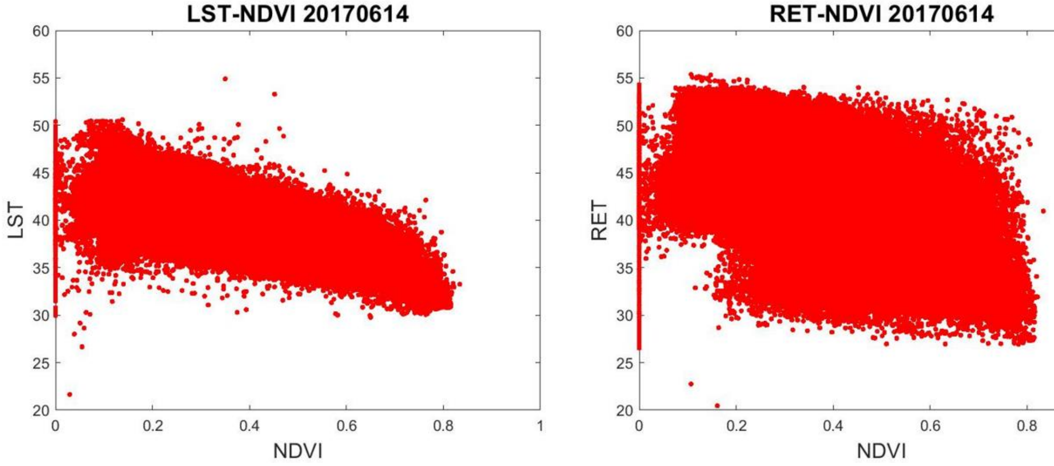

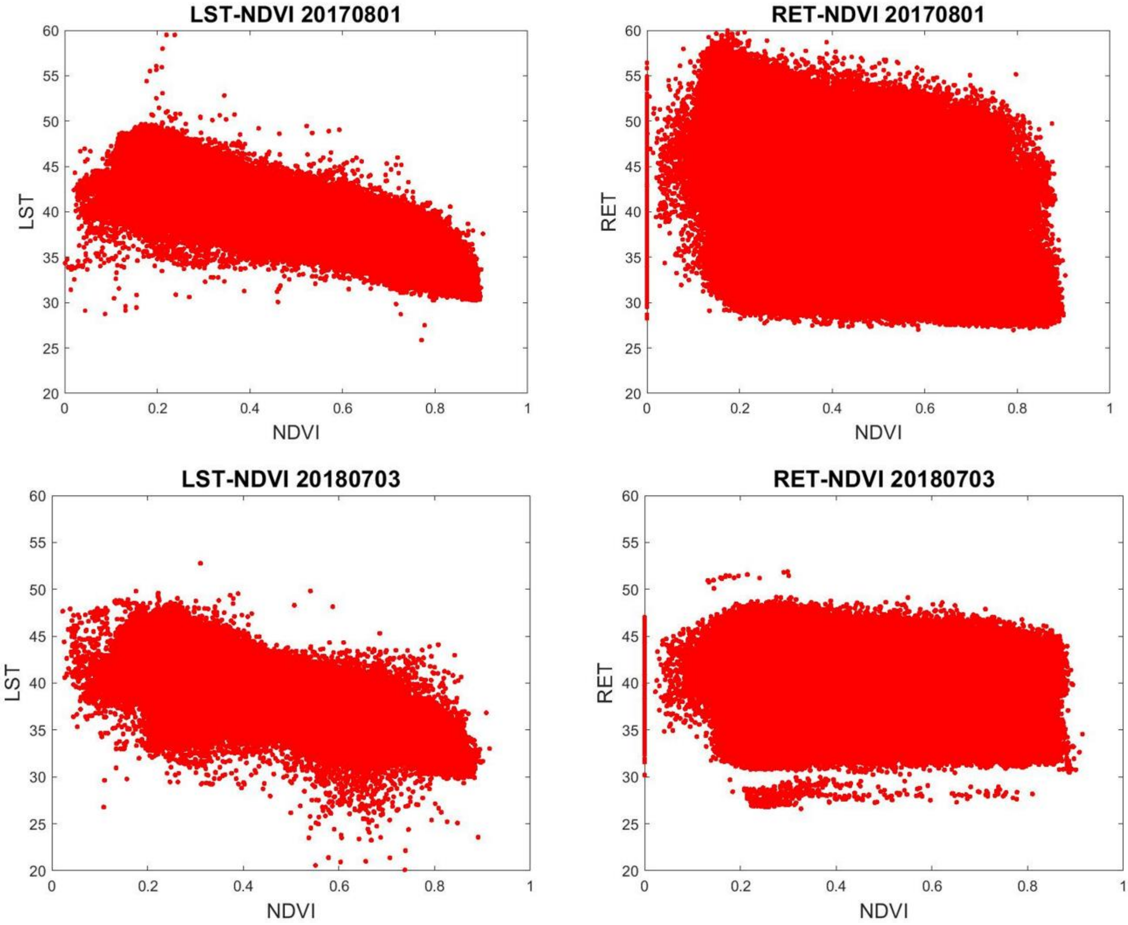

Figure 4.9 LST- NDVI and RET-NDVI spatial relationship

Chapter 5

Anomalies and a combined agricultural drought index

The objective of this chapter is to show the results of anomalies computation and combined drought index assessments for water stress monitoring. Long time series from 2000 to 2020 of precipitation, SM, LST and VIs satellite retrieved are considered for anomalies computation. Moreover, short period from 2015 to 2019 is analysed using high-resolution observed data and simulated variables from FEST-EWB. Therefore, the differences in terms of anomalies and correlation coefficients of the variables involved are discussed. The combined drought index is tested on different datasets and its reliability is assessed for different years comparing the levels of dryness with the irrigation aqueduct volumes of Capitanata consortium.

5.1 Long time series analysis (2000-2020)

In this first part historical series from 2000 to 2020 are analysed. Precipitation series extracted from ERA5 database, SM from ESA CCI active/combined, SMOS and SMAP products, MODIS vegetative indices and LST from MODIS are used to compute anomalies. The combined drought index is validated and compared with irrigation volumes and news from local newspaper.

5.1.1 Anomalies

5.1.1.1 Precipitation anomaly and SPI1

Precipitation anomaly (PA) and SPI1 are calculated using precipitation time series from 1st January 2000 to 30th March 2020 of ERA5 database.

As we can see in Figure 5.1, PA has a low boundary equal to 0.4, that represent the anomaly for all the no raining day (zero precipitation value), this negative anomaly does not represent always an effective precipitation deficit. Hence, PA should be carefully used, taking into account the possibility of an overstimation of drougth conditions.

On the other hand, the SPI (Figure 5.2) is the result of a statistical prosess where precipitation is fitted with gamma distribution not considering zero values (see 1.3.1). For dry climate where zero precipitation values are common, such in our case, the calculation of SPI is skewed (Wu, Svoboda, Hayes, Wilhite, & Wen, 2007). Therefore, the application of SPI is critial and its interpretation must be done properly.

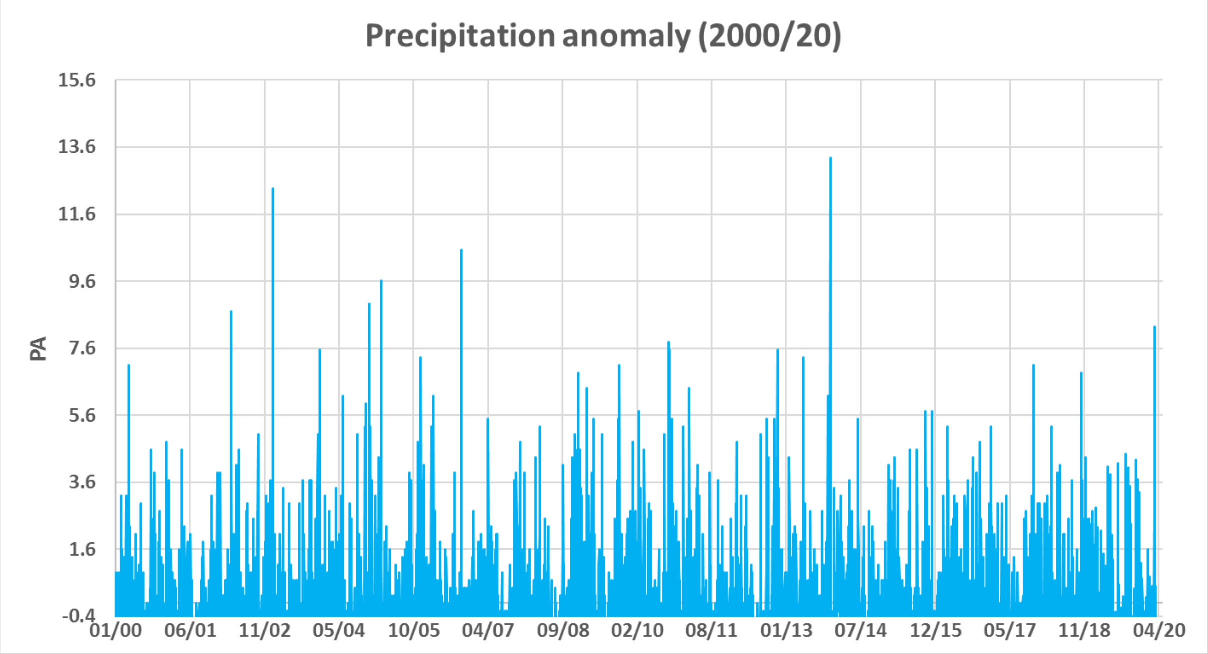

Figure 5.1 PA of ERA5 precipitation

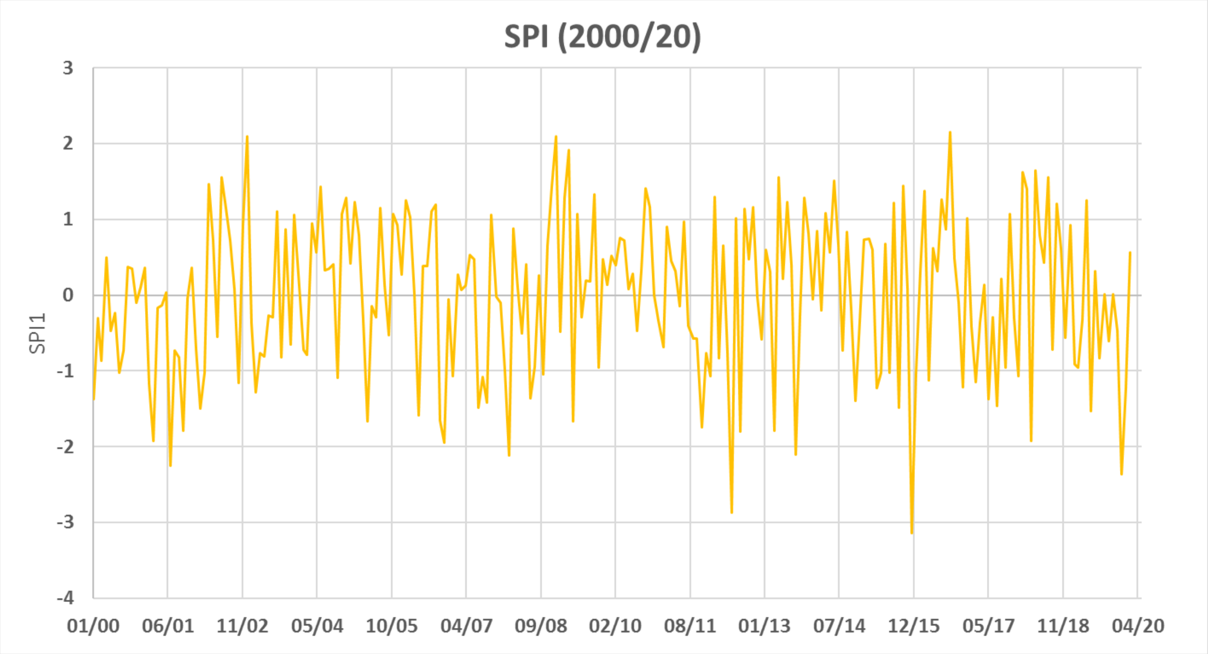

Figure 5.2 SPI of ERA5 precipitation

5.1.1.2 Soil moisture anomalies

Soil moisture total and monthly anomalies are calculated using SMOS, SMAP and ESA CCI (active and combined) satellite products. ESA CCI are the most complete series from 2000 to 2019, instead SMOS and SMAP start from 2010 and 2015 respectively. In Figure 5.3, 5.4, 5.5 and 5.6 the comparisons between monthly and total anomalies for each soil moisture product are visible and the values of RMSE are reported in Table 5.1. Monthly anomalies will be chosen in the combined drought index computation because can reproduce in the best way the daily variation of soil moisture.

Table 5.1 RMSE between monthly and total anomalies for each soil moisture satellite product

	Monthly vs total SMA			
	ESA CCI active	**ESA CCI Combined**	**SMOS**	**SMAP**
RMSE	0.79	1.0	0.76	1.04

Furthermore, a comparison between the different soil moisture products is carried out, considering the ESA CCI Combined the RMSE are calculated between the anomalies. Considering the difference in spatial resolution (25km for ESA CCI, 40/50km for SMAP and SMOS) good agreement is obtained as we can see in Table 5.2.

At the end, in the view of combined drought index evaluation, the average of the monthly soil moistures anomalies is computed to have the most complete series (Figure 5.7).

Table 5.2 RMSE between soil moisture products anomalies

	Combined-Active	**Combined- SMOS**	**Combined- SMAP**
RMSE (SMA)	0.58	0.76	0.71
RMSE (monthly SMA)	0.78	1.06	1.03

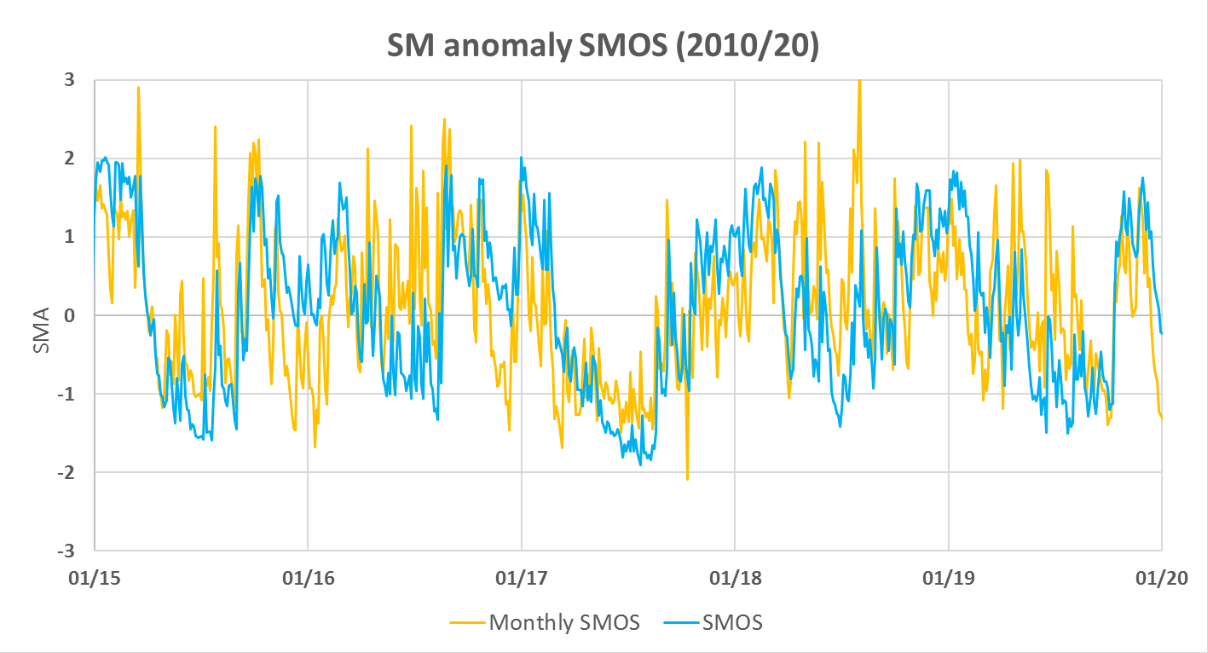

Figure 5.3 Comparison between monthly and total anomaly of SMOS soil moisture

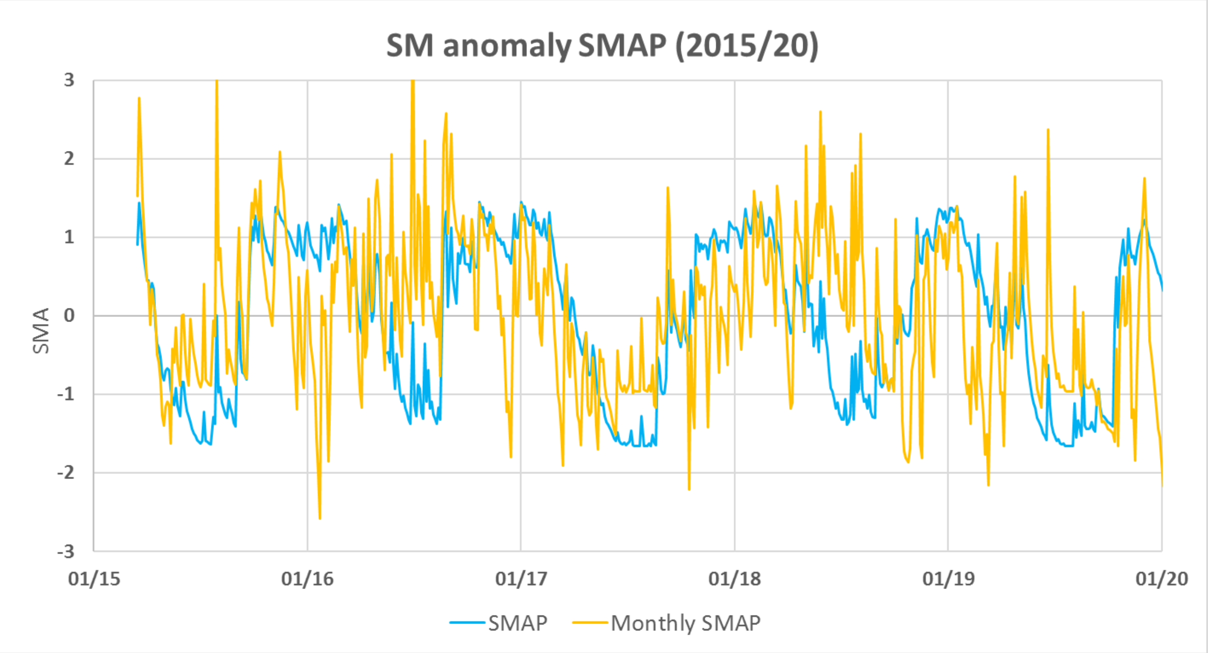

Figure 5.4 Comparison between monthly and total anomaly of SMAP soil moisture

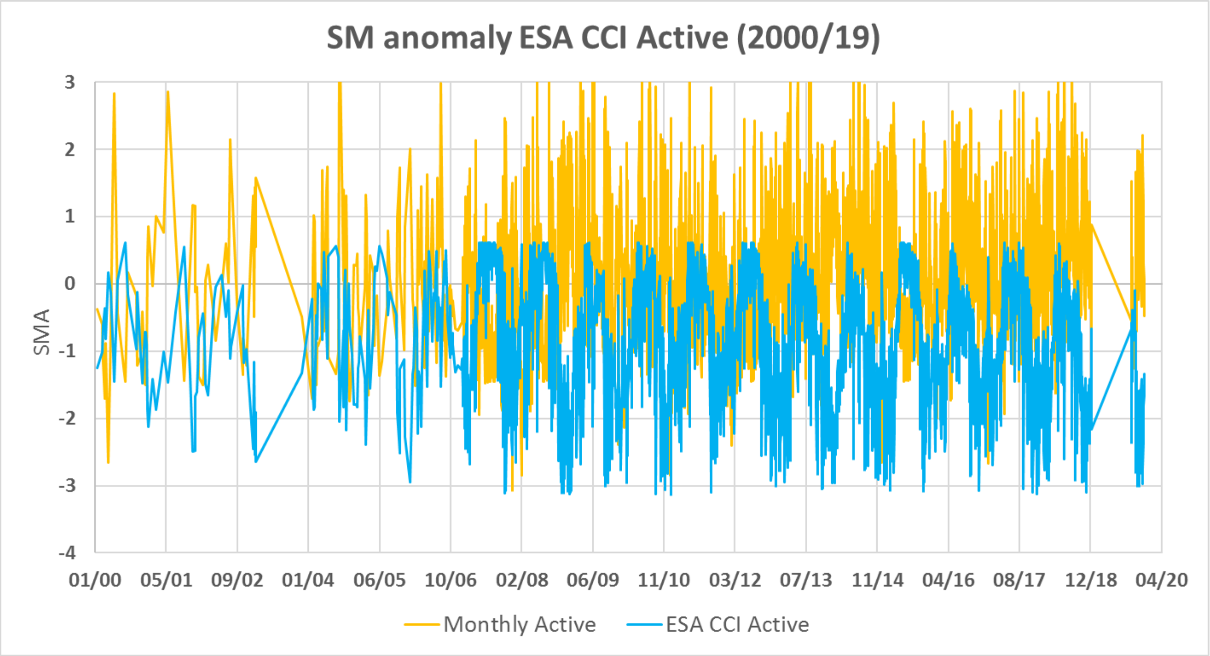

Figure 5.5 Comparison between monthly and total anomaly of ESA CCI Active soil moisture

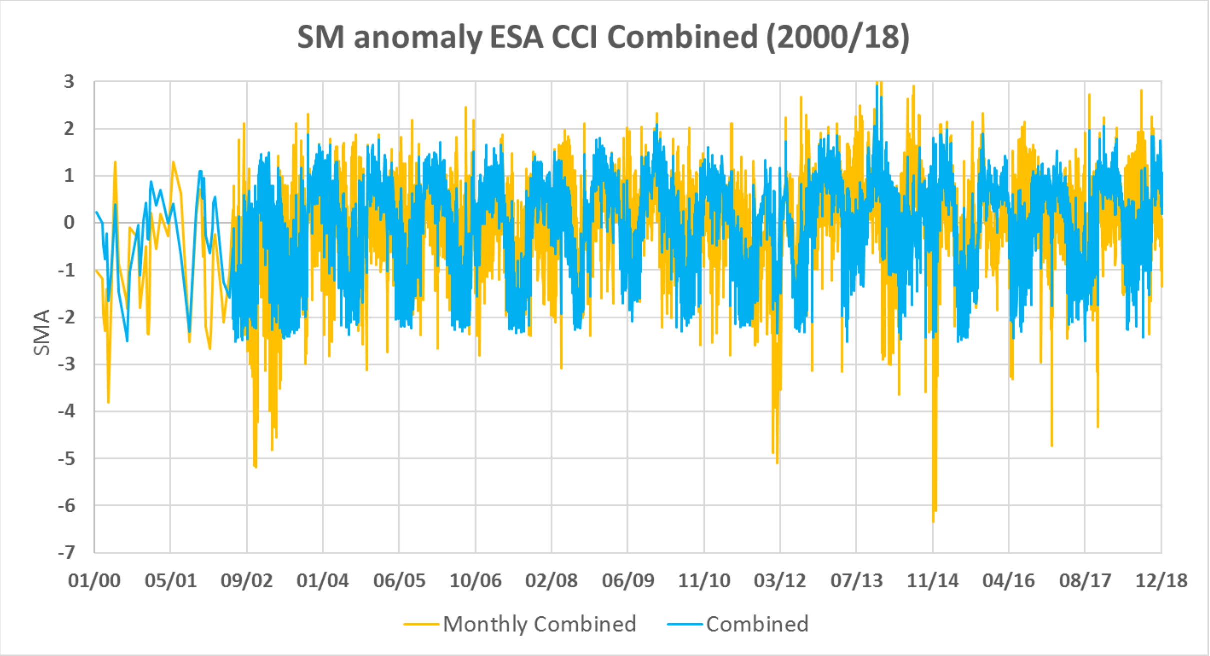

Figure 5.6 Comparison between monthly and total anomaly of ESA CCI Combined soil moisture

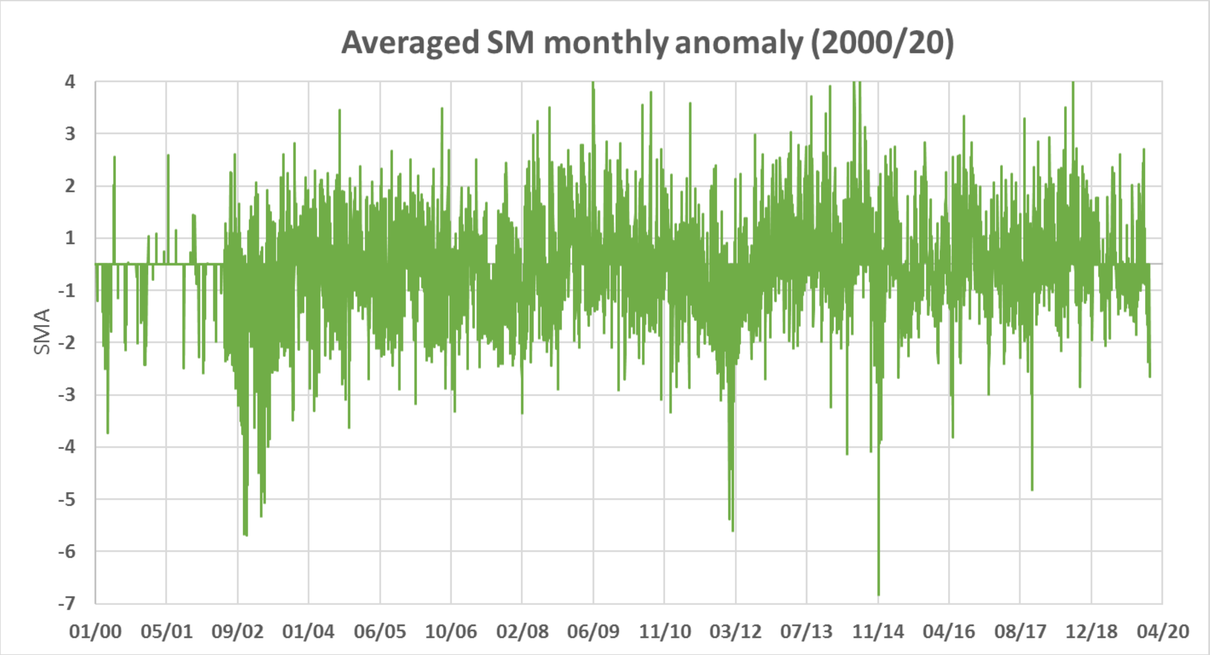

Figure 5.7 Soil moisture anomaly averaged of SMOS, SMAP, ESA CCI Active and Combined anomaly

5.1.1.3 Land surface temperature anomalies

LST series retrieved from MODIS (1km of spatial resolution) are used to calculate LST anomaly (Figure 5.8). Positive values of LSTA represent warm days, where the LST is higher than the mean, so water stress could occur, instead negative values are the colder day. A seasonality is visible in the plot, low values in autumn/winter and high values in spring/summer.

With a view to test the drought indicator, monthly anomalies are computed. Indeed, using anomalies among all the series is difficult to capture day by day the water stress, the natural high summer temperature can involve an overestimation of warm days. As visible from the comparison between total and monthly anomalies, that shows a RMSE equal to 1.06 °C, the seasonality is removed, and the summer peaks are damped.

The same procedure will be carried out also for vegetative indices and ET anomalies, because even these parameters show a seasonality that must be removed to have reliable values for drought index computation.

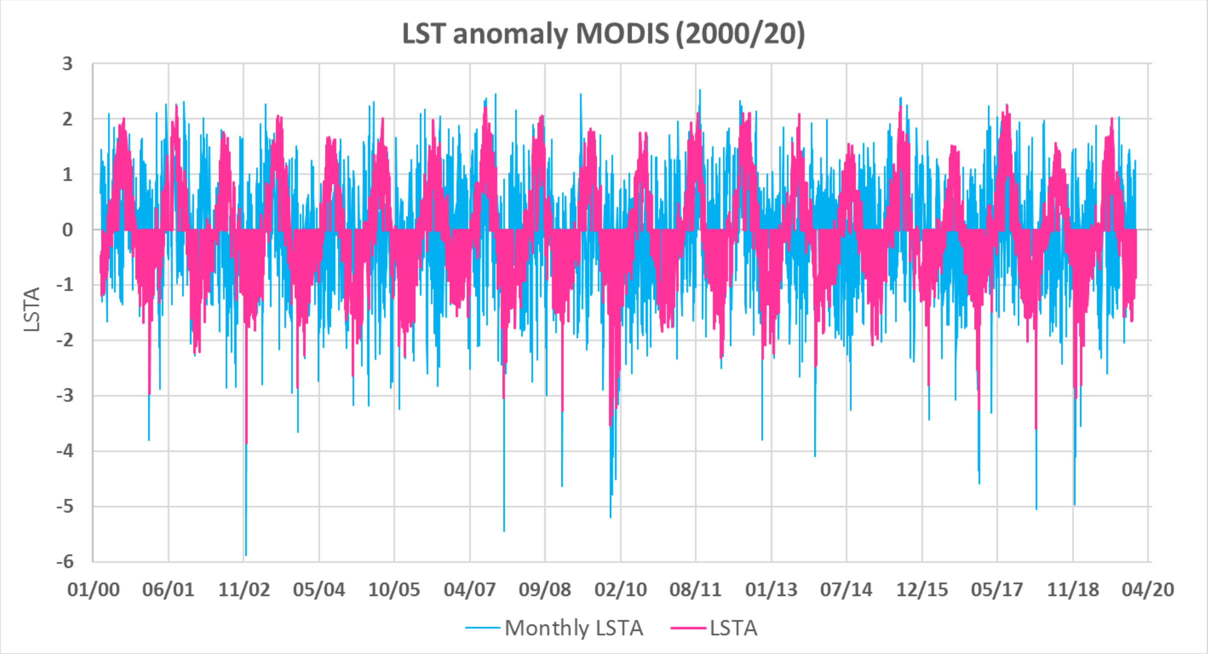

Figure 5.8 Comparison between monthly and total LST anomaly from MODIS

5.1.1.4 Vegetative indices anomalies

Vegetative indices series extracted from MODIS database contain 4 indices: NDVI, NDWI, EVI and SAVI. EVI and NDVI are available at 250 meters every 16 day and at 500 meters every 8 days, small difference is observed between the datasets with different spatial and temporal resolution, a RMSE of 0.44 is obtained. Thus, in the following analysis both the indices are considered at 500m every 8 days in order to have more data.

Anomalies are calculated for all the indices and as we can see in Figure 5.9 the anomalies show the same trend. NDVI and SAVI has a good agreement with a RMSE equal to 0.12, while NVDI and EVI e NDVI and NDWI show RMSE of 0.77 and 0.71 respectively (Table 5.3).
But if the peak between NDVI and EVI agree, comparing NDVI and NDWI anomalies peaks in opposition are observed (Figure 5.10). Therefore, since NDVI, SAVI and EVI show the same behavior only NDVI, the commonest index, will be considered in the following analysis together with the NDWI.

Table 5.3 RMSE between vegetative indices total anomalies

Anomalies	**NDVI-SAVI**	**NDVI- EVI**	**NDVI- NDWI**
RMSE	0.12	0.76	0.71

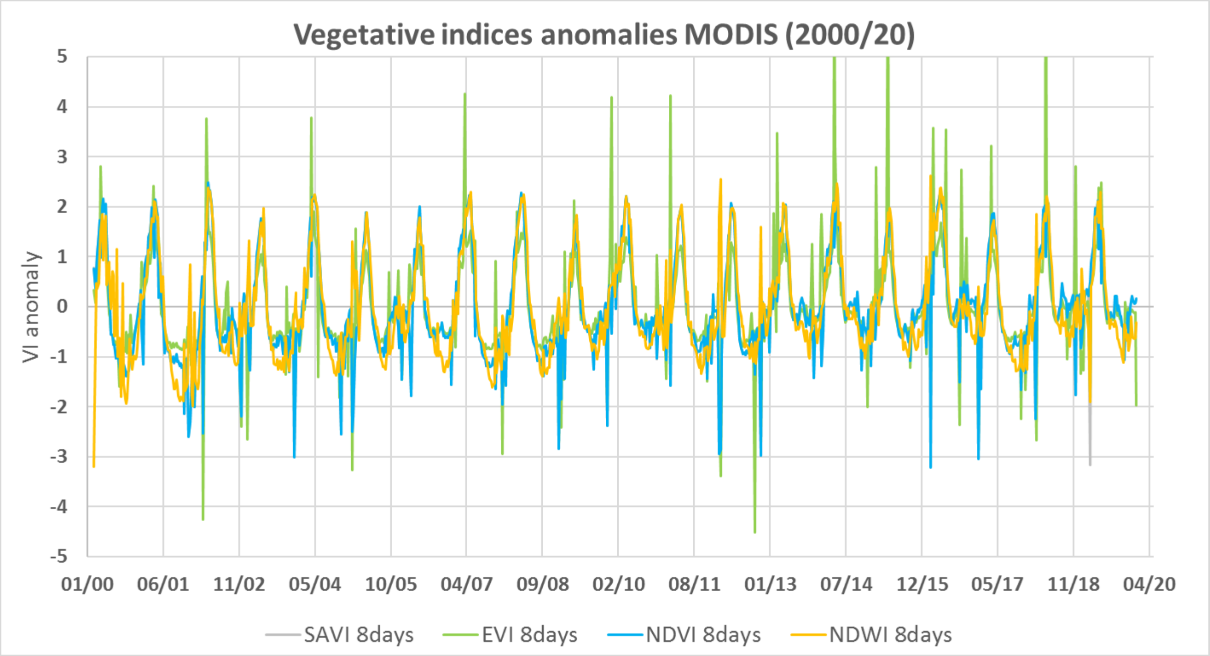

Figure 5.9 Comparison between total anomalies of vegetative indices from MODIS

Looking at the zoom figure, we can notice that at positive peaks in NDWIA (orange dots) correspond with negative peaks in NDVIA (blue dots). As is well known, NDVI is strongly correlated to leaf area index while NDWI is link with the moisture of the crop. The opposite peaks are caused by precipitation events, that increase immediately the NDWI values but not the NDVI, that is always affected by a delay in the response. As a matter of fact, precipitation events occurred during the 3 dates in question, PA is reported in Table 5.4.

Table 5.4 PA values for the days corresponding to NDVI and NDWI opposite peaks

Day	**PA**
10/10/2011	+0.9
16/11/2012	+1.15
18/02/2016	+1.61

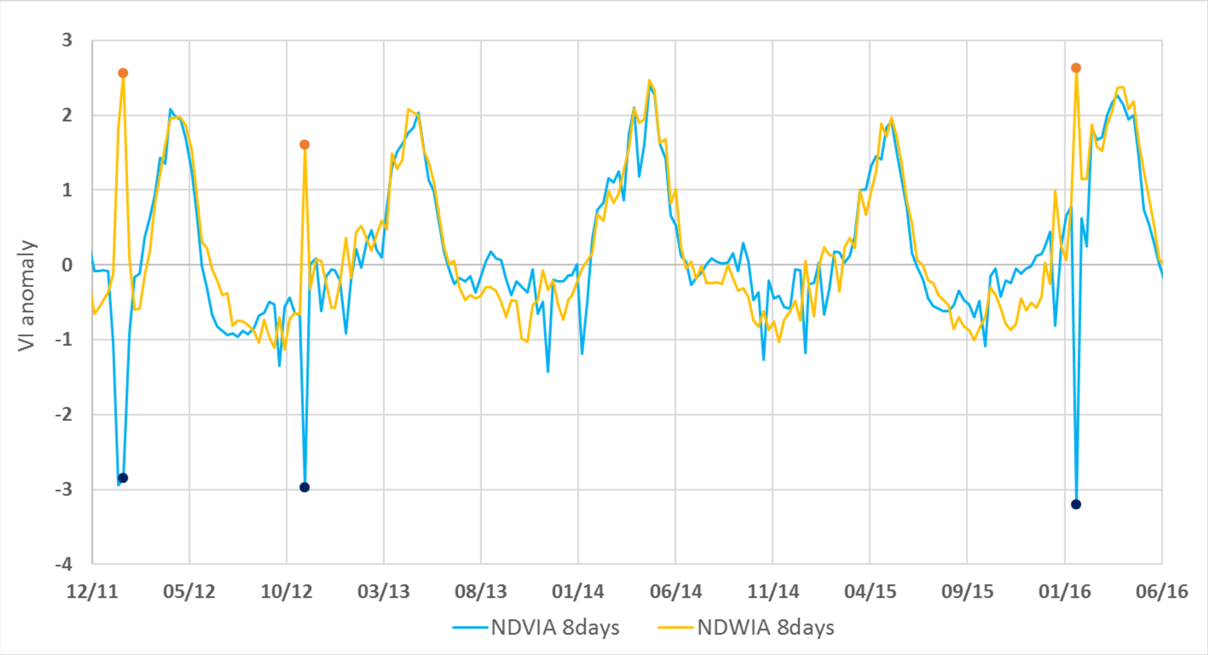

Figure 5.10 Zoom on opposite peaks observed in NDVI and NDWI anomalies

For both the indices chosen, NDVI and NDWI, monthly anomalies, are computed (Figure 5.11). Seasonality is removed but the opposite peaks remain as a proof the different meaning of the indices. The seasonal anomalies are compared to the annual ones and RMSE equal to 0.93 is obtained for NDVI and RMSE equal to 1.01 for NDWI.

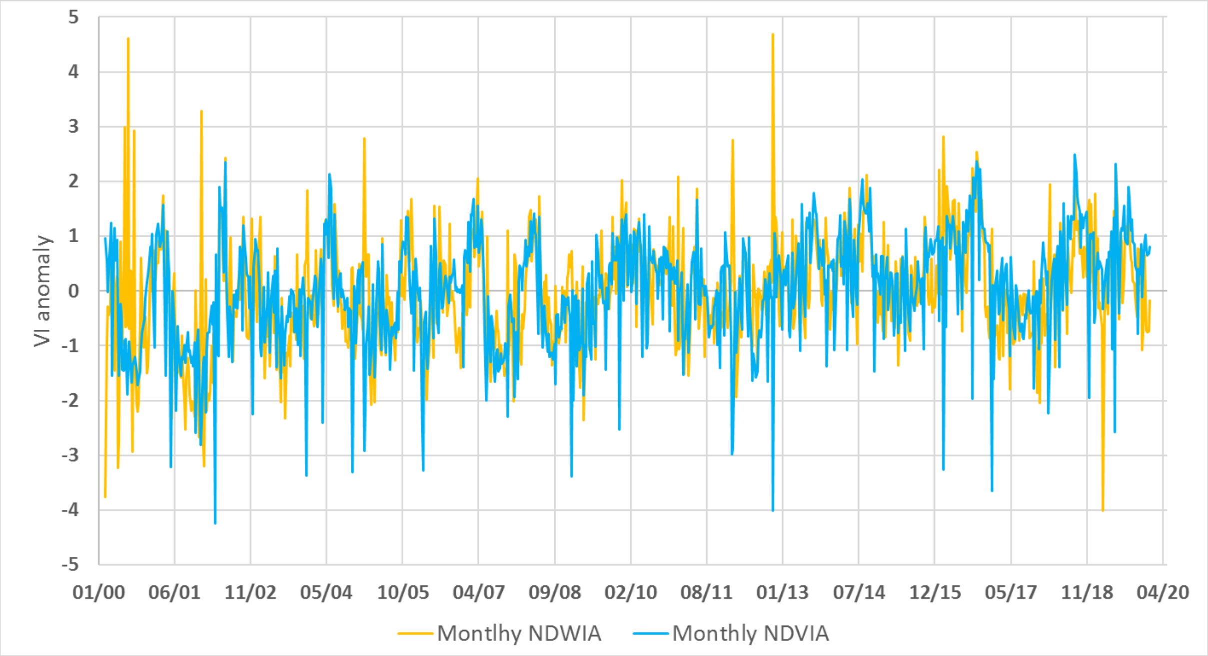

Figure 5.11 Comparison between monthly anomalies of NDVI and NDWI

5.1.2 Correlation between anomalies

Pearson's correlation coefficients are computed between the anomalies at basin scale; averaged SM monthly anomaly (Figure 5.7) and monthly anomalies of LST and NDVI from MODIS are considered (Figure 5.8 and 5.11).

As we can see from Table 5.5 SPI and SMA have positive correlation. The correlation coefficient shows positive but low value because, when precipitation deficit occurs, e.g. negative values of SPI are observed, the fields are irrigated so SM increases and SMA takes positive values.

The other variable correlations show the correct sign: positive correlation between SPI and NDVAI, SMA and NDVIA while negative correlation between SPI and LSTA, LSTA and SMA, LSTA and NDVIA, however, the values are low. This low correlation between anomalies is caused by different factors involved.

Firstly, correlation coefficients are calculated on anomalies and not on real variable value, thus the relation is weaker due the uncertainties introduce in the computation of the anomaly itself, and can also be related to the different time response of the index to drought (e.g. precipitation is the first while vegetation is the last).

Secondly, a scale problem is evident due to the different spatial resolution of each variable. SM products retrieved at 25/50 km are correlated with NDVI and LST at 1 km, even though the values are averaged for the same area.

Furthermore, the coefficients are calculated above all the series, from 2000 to 2020, so both summer and winter period are included. If it is true that LSTA and NDVIA are negatively correlated in summer, in winter the opposite relation is verified. As we can see in Table 5.6 computing LST and NDVI correlation considering only winter months positive value results, instead considering spring/summer negative value is obtained. Moreover, as mentioned before, vegetation stress response delays with respect water deficit and high temperature, this process implies a further decreasing in correlation values.

Table 5.5 Correlation coefficients between anomalies

Long Series 00-20					
SPI-SMA	SPI-LSTA	SPI-NDVIA	LSTA-NDVIA	SMA-LSTA	SMA-NDVIA
0.20	-0.20	0.18	-0.05	-0.19	0.10

Table 5.6 Correlation coefficients between LST and NDVI anomalies for winter and summer period

LSTA-NDVIA winter	**LSTA-NDVIA summer**
0.33	-0.2

5.1.3 Agricultural combined drought Index

Combined drought index is evaluated using the anomalies previously calculated. To study the reliability and the response on different input data of drought index values, different combinations of anomalies are used:

- Case 1: drought index with SPI1, averaged SMA, monthly LSTA and monthly NDVIA
- Case 2: drought index with PA, averaged SMA, monthly LSTA and monthly NDVIA

Case 1 and 2

To compare how the level of dryness changes in time, cumulative drought index curve is evaluated for each year. As we can see in Figure 5.12, all the curves have a common trend: from the begin of the year till March (100 Julian Day) the curves have gentle slope, then from March to October (250 JD) they are very steep due to drought conditions and at the end of the year return flat. This behavior agrees with the crop seasonality and with the irrigation period.

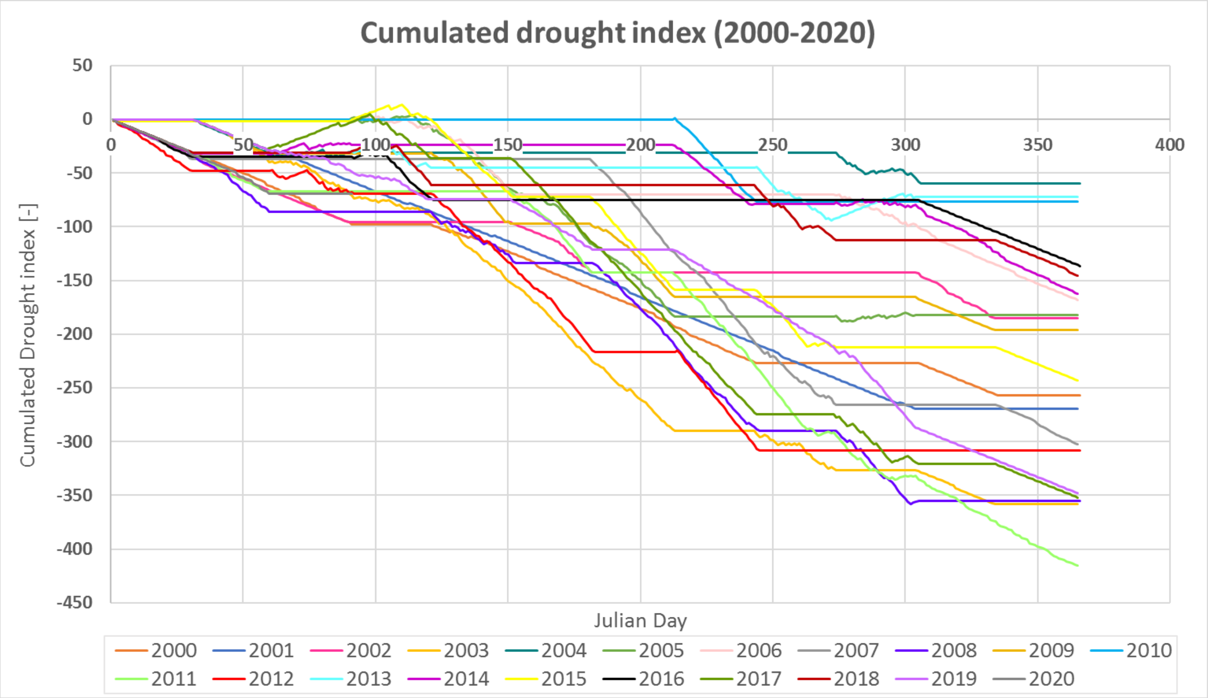

Figure 5.12 Cumulated drought index of long time series analysis

Furthermore, in Figure 5.13 are shown the values of the cumulated indices of each year useful to estimate the level of drought on the entire year and compare it with the others. Considering the drought index with SPI1 the driest years are 2003, 2008, 2011, 2017 and 2019, instead considering the one with PA the driest years are 2003, 2007, 2008, 2011, 2012 and 2017.

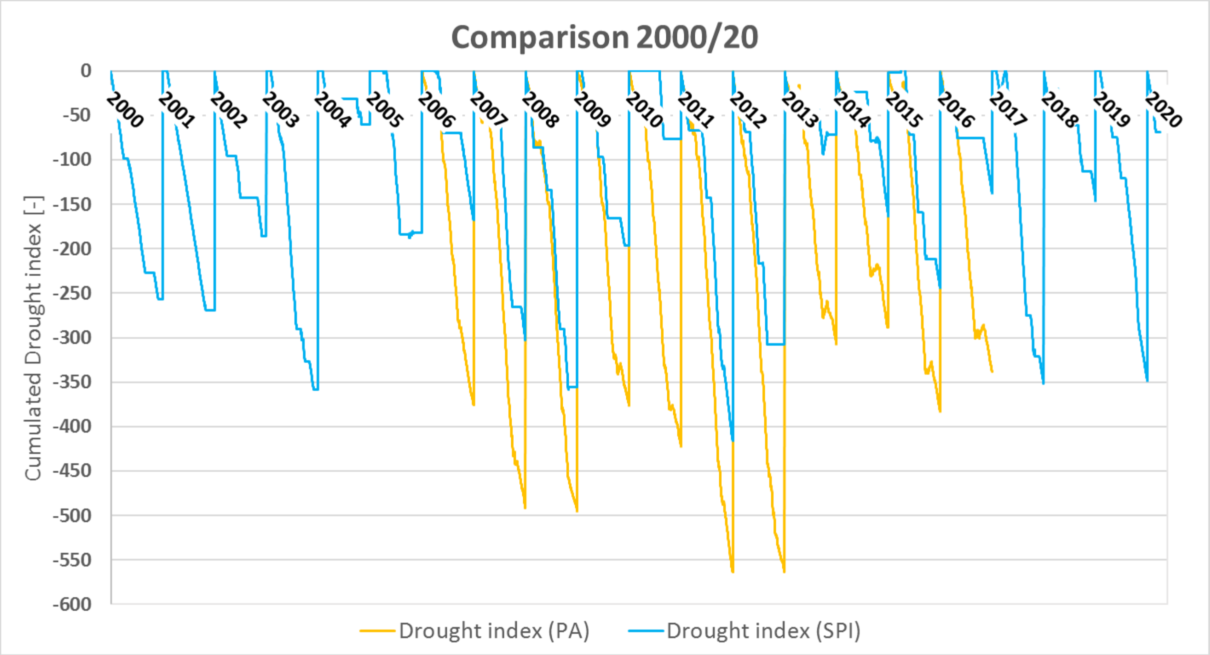

Figure 5.13 Comparison between cumulated drought index computed using PA and SPI1

As we can see, comparing the drought index in case 1 and 2, a great difference is observed. The case 1 shows lower values, so fewer days with drought conditions are detected from the drought index based on SPI1, with respect to the case 2 that shows more days with extreme dryness. Firstly, this difference is caused by the differences and the issues regarding PA and SPI1 computation, already explained in 1.3.1.1 and 5.1.1.1.

Remembering that the index takes zero values (no drought conditions- green index) for each day with SPI1 higher, a check on the SMA values for these days (SPI1 >0) is performed and results that in some months SMA is less than zero. This inconsistency is caused by the fact that the SPI1 is a monthly index while the drought index is daily, so the monthly SPI1 values are replicated for every day of the month in question. Can be happen that a great precipitation events during a dry month leads to positive value of SPI1 which, however, is not significant for the entire month. In Table 5.7 the months affected by this problem are visible. Plotting PA, SPI and SMA for some of these months the problem is observed (Figure 5.14). For this analysis PA and SPI from observed precipitation is also considered (see Paragraph 5.2.1.1).

In July 2017 and in May 2018 SPI1 values is positive but looking at PA and SMA negative values are observed for most of the time. Hence, it’s clear that the strong precipitation events occurred (corresponding to the peaks in PA) have affected the SPI1 values, that is no more trustworthy.

In April 2017 there is also a difference between SPI1 from observed precipitation and SPI1 from ERA, the former is higher than 1 probably influenced by the strong precipitation event observed in the first half of the month. While the latter, is less than zero, agreeing with SMA trend.

The same check is made even for drought indicator computed with PA, as we can from the Table 5.8 the number of days with this kind of inconsistency, e.g. SPI1>0 or PA>0 and SMA<0, are many more when SPI1 is taken into account.

For all the days where the average SMA is less than zero, also a check on the single values of SMA from SMOS, SMAP, ESA CCI, is carried out, a decrease of 2% in the number of inconstancies is noticed.

Table 5.7 Months with inconsistency in term of SPI and SMA, comparison between SPI from observed and ERA5 precipitation

Months for those SPI1>0 and SMA<0	SPI1 obs prec.	SPI1 ERA5 prec.
April 2017	>0	<0
July 2017	>0	>0
May 2018	>0	>0

Table 5.8 Comparison between the number of days with inconsistency observed in the drought index calculated with PA and SPI

Index	n° of days with inconsistency	% among the series
PA	80	1
SPI1 (averaged SMA)	1372	18
SPI1 (checked)	1187	16

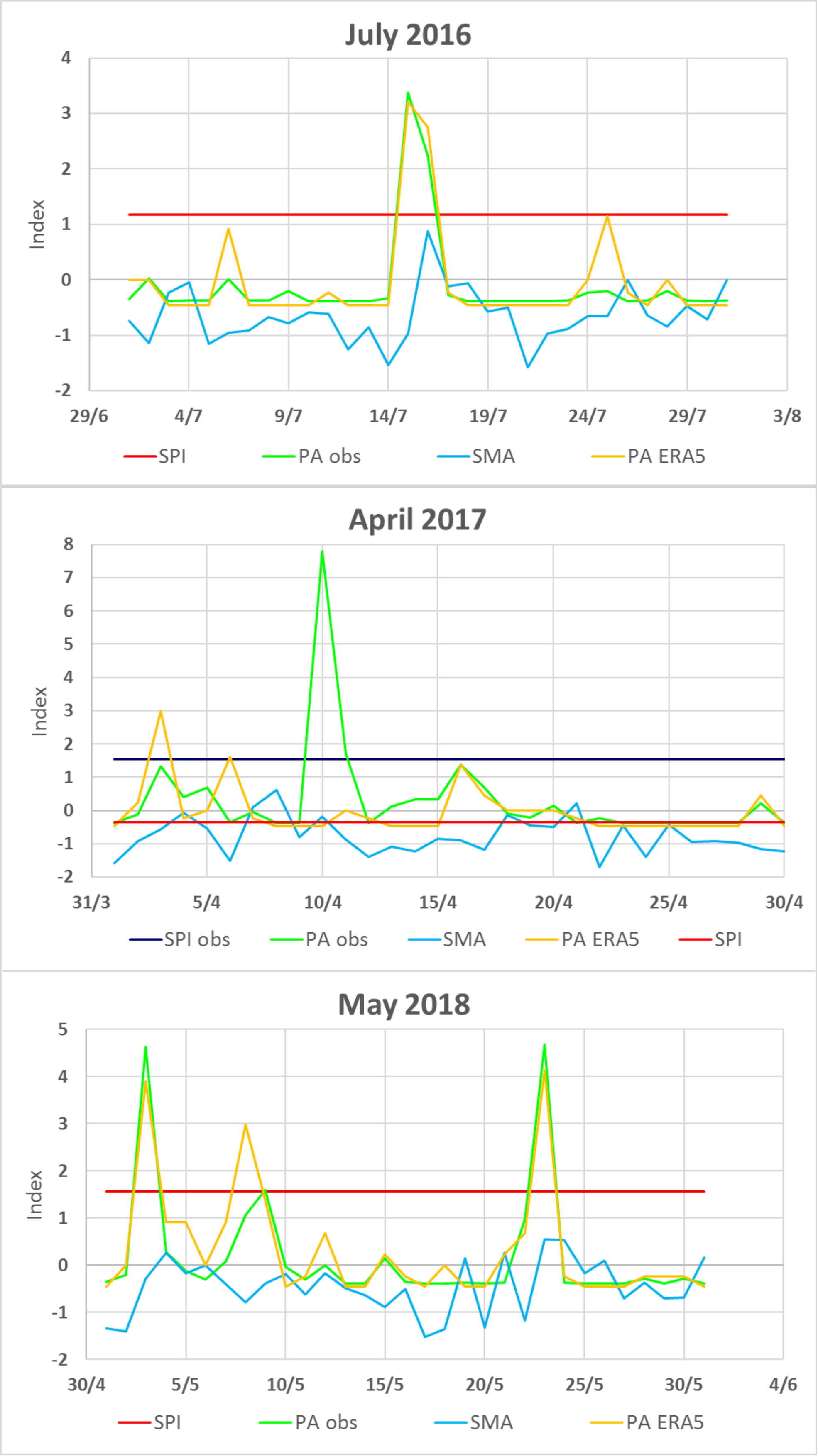

Figure 5.14 Comparison between SPI, PA and SMA of the months for those inconsistency is observed

In the end, a zoom is done for 2020. Water stress conditions are detected from the Capitanata Consortium in the first months of 2020, as confirmed by low values of water availability in the consortium dams. Indeed, an available volume equal to 126,140,400 mc is measured on 7th April 2020 that compared with the volume of the same data last year, equal 207,483,400 mc, corresponds on a decrease of 40%. Therefore, having ERA5 precipitation, SMOS and SMAP database, LST and NDVI from MODIS available till the 31st of March 2020 drought index is calculated. The index assesses drought conditions for several day (Figure 5.15), as in the other case the index with SPI1 shows less drought conditions with respect the one with PA (8 vs 12 days of severe drought conditions).

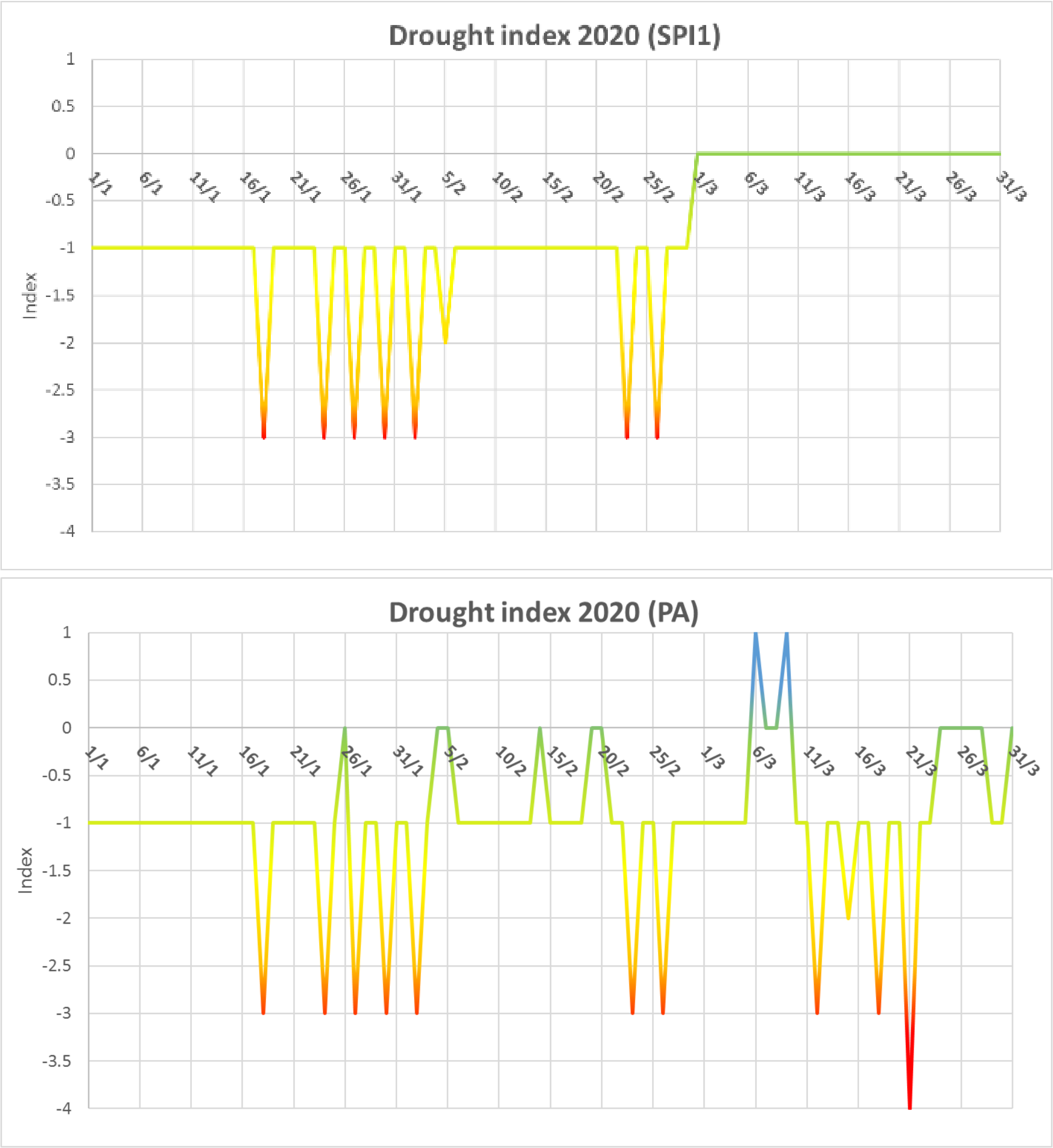

Figure 5.15 A zoom on 2020: comparison between the drought index calculated with SPI and PA

5.1.4 Drought index validation

<u>5.1.4.1 Comparison with irrigation aqueduct volume (2006/16)</u>

Irrigation volume are used to provide a reliable assessment of drought index values, previously calculated. Irrigation values from 2006 to 2016, except for 2008 and 2009, are available, so the drought index based on long series is used for the following analysis. Daily values at consortium scale are provided from the 1st of April to 31st December for each year. As we can see between the most irrigated year, e.g. 2012 and the one, e.g. 2009, there a difference of 20,000,000 mc (Figure 5.16). Considering the drought index with PA, it is confirmed that 2012 and 2011 are the driest years and the other years are in good agreements with cumulative irrigation volume.

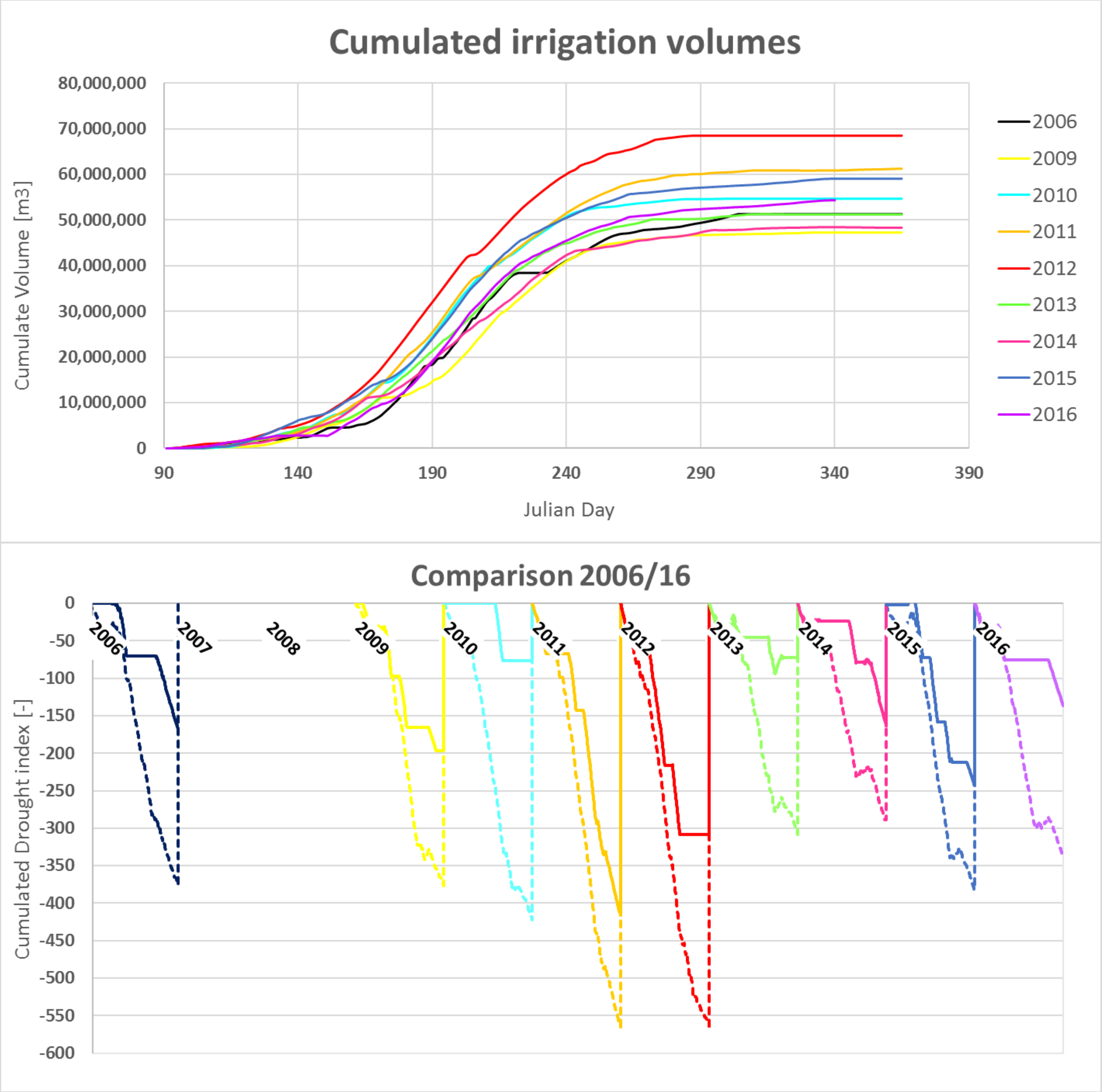

Figure 5.16 Irrigation aqueduct volumes and drought index comparison (dashed lines drought index with PA, continuous lines drought index with SPI)

The scatterplot of cumulative drought index values and irrigation volume at the end of the year is visible in Figure 5.17. The scatterplot shows good agreement with high R^2 values in both the case (index with SPI and PA). Positive correlation is observed, because of an increase in the drought index means an increase of dryness condition so more irrigation is required.

The scatterplot of cumulative drought index and irrigation volume summed with precipitation volume, calculated multiplying ERA5 precipitation values by the basin are, shows lower values of R$^{2.}$ Negative correlation is observed, indeed, if strong precipitation events occur (increase in irrigation + precipitation volume) drought index keeps a constant value. This means that more or less the farmers provide similar "water" (irrigation + precipitation) to their fields.

Table 5.9 Angular coefficients and R^2 between drought index and irrigation volume (and precipitation)

	Index with SPI			**Index with PA**		
	Angular coeff. [10^{6}mc]	**Intercept [10^{6}mc]**	**R^2**	**Angular coeff. [10^{6}mc]**	**Intercept [10^{6}mc]**	**R^2**
Irrigation volume	-0.038	50	0.4148	-0.054	30	0.6746
Irrigation+ precipitation volume	0.52	900	0.3054	0.36	900	0.1098

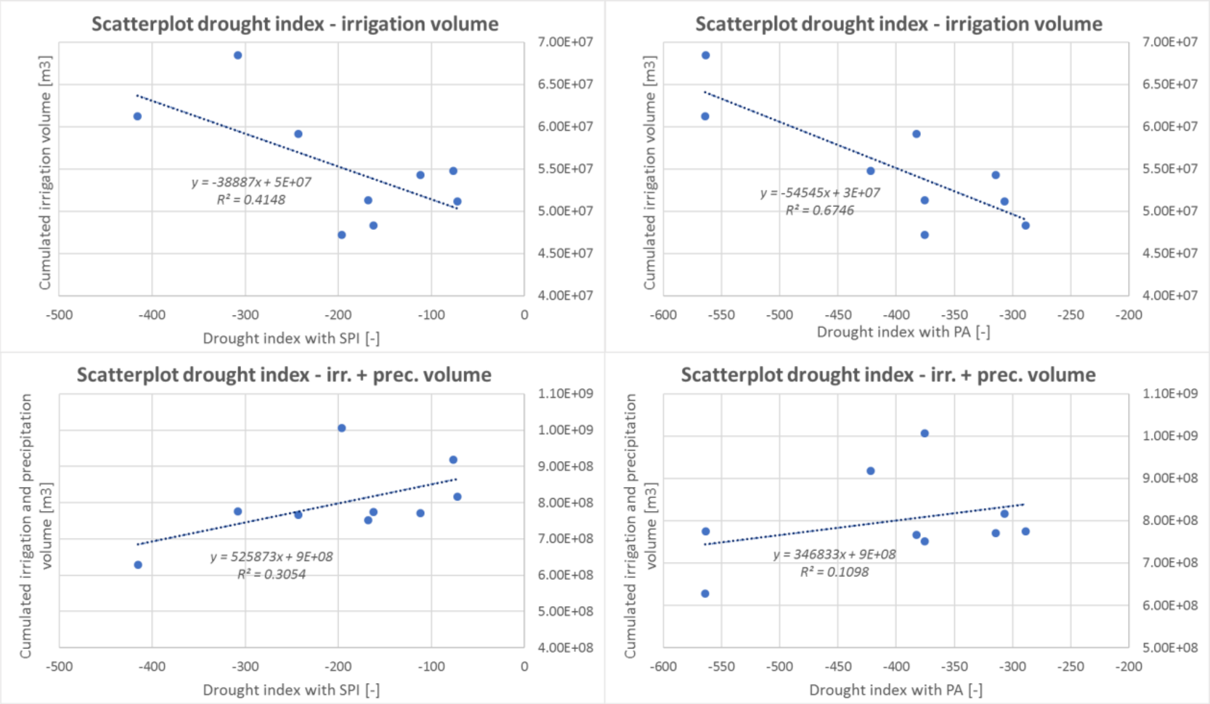

Figure 5.17 Scatterplot between drought index and irrigation volumes and between drought index and irrigation plus precipitation volumes

5.1.4.2 Comparison with news from local newspaper

As a further confirmation of the capability of the combined drought index to detect agricultural drought conditions, a comparison with news from local newspaper is provided.

In the news article (1) problems on Capitanata Consortium tomato cultivation because of high temperature and water stress conditions are mentioned*: very high temperatures recorded in recent days in Puglia and throughout Southern Italy are affecting the production of tomatoes, especially in the areas of Capitanata, the estimated data suggest a reduction in yield that exceeds 20-25% (August 2012).*

In the news article (2) water crisis of 2017 and 2003 are mentioned: *Coldiretti has, in fact, found that in June 2017 the temperature in Italy was «well 3.22 degrees higher than the reference average. An anomaly that has been the worst for 217 years, with the exception of 2003, the historic year for heat and drought».*
The account of the damages - the Coldiretti specifies - «has exceeded the billions of euro in the Italian campaigns interested for beyond the 2/3 from a situation of serious water crisis» (July 2017).

5.2 High resolution analysis (2015-2019)

In this second part, daily anomalies using high resolution data and simulated variable are computed. Observed precipitation, SM and RET resulting from the hydrological model, LST and vegetative indices from Landsat images are analysed. Then, SPI1, SWDI, SPEI and evapotranspiration deficit are calculated to explore water stress indices. Anomalies maps are evaluated to investigate the spatial distribution of anomalies among the area and correlations between anomalies are performed. Anomalies only in cultivated fields are compared with anomaly at basin scale. At the end, drought index is developed, and the comparisons with irrigation aqueduct volumes and SWDI are performed.

5.2.1 Anomalies and water stress indices

5.2.1.1 Precipitation anomaly and SPI1

PA and SPI1 are calculated using precipitation series measured from meteorological stations located in the basin area (Figure 5.18 and 5.19). SPI is compared with the SPI of ERA5 precipitation, good agreements is obtained between the series, RMSE of 0.33 and a Nash index of 0.52 are obtained.

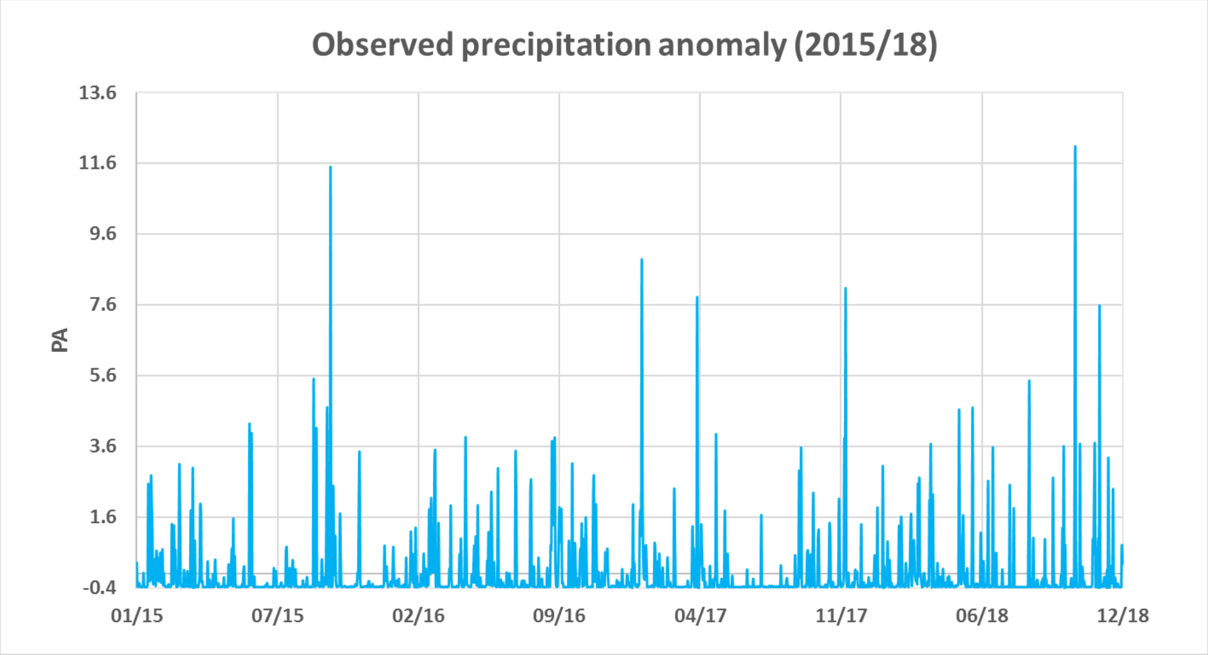

Figure 5.18 PA of observed precipitation

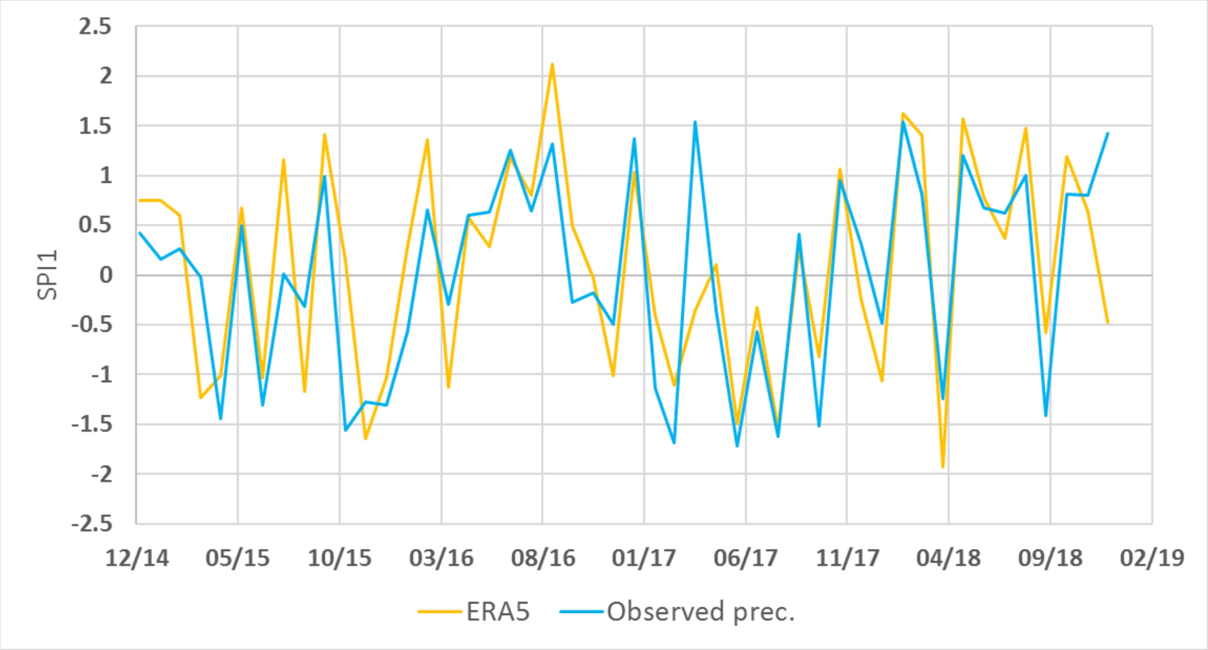

Figure 5.19 Comparison between SPI of observed and ERA5 precipitation

5.2.1.2 Soil moisture anomaly

Anomaly resulting from the simulated SM is visible in Figure 5.20. As we can see, for 2015 SMA has negative values, initial condition imposed in the hydrological model could have affect the SM values for the first years of simulation. Both monthly and total anomalies are represented in figure, show a RMSE equal to 0.44, and as done before for long series, monthly anomalies are chosen because are able to reproduce the soil moisture variation in particular during the summer period. Moreover, Copernicus SM anomaly, that is at high resolution (1km) is compared with SMA from FEST, a RMSE equal to 1.3 and a Nash of -1.08 are obtained (Figure 5.21).

Furthermore, SM monthly anomaly from FEST is compared with SM monthly anomaly from satellite products in the period 2015-2019, RMSE and Nash index are visible in Table 5.10.

Table 5.10 Nash index and RMSE between simulated and remote sensed soil moisture monthly anomaly

	ESA CCI Combined-FEST	**ESA CCI Active-FEST**	**SMOS-FEST**	**SMAP- FEST**
RMSE	1.15	1.18	1.22	1.28
Nash index	-0.78	-0.60	-0.80	-0.76

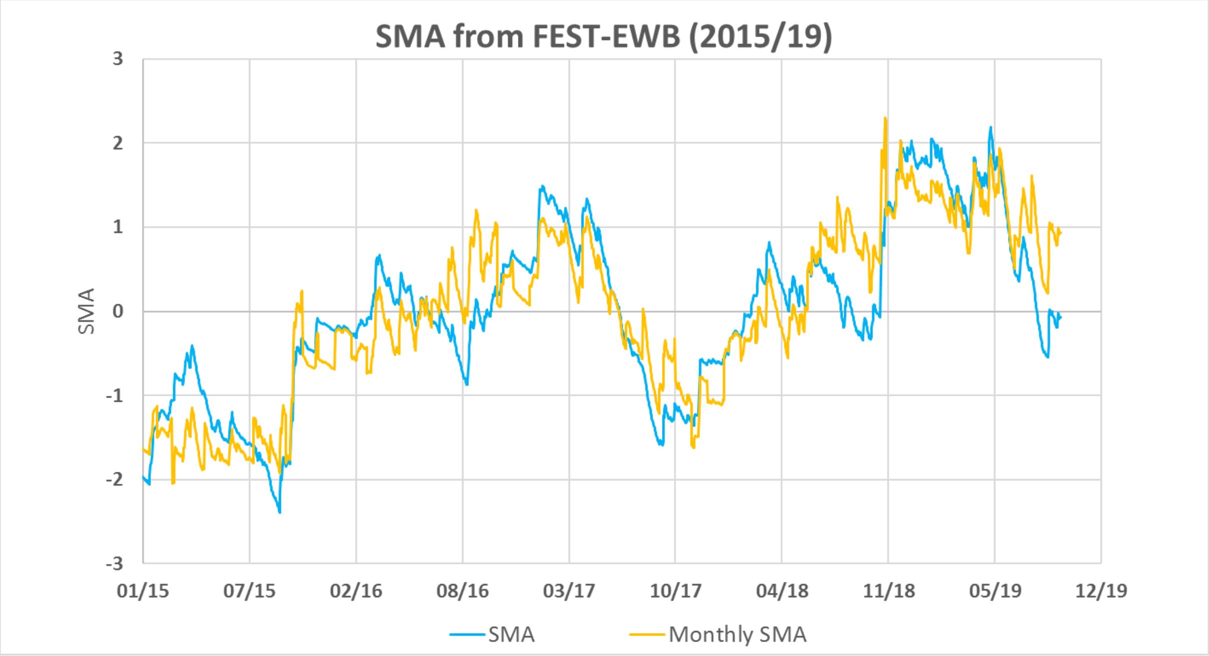

Figure 5.20 Comparison between monthly and total anomaly of simulated SM

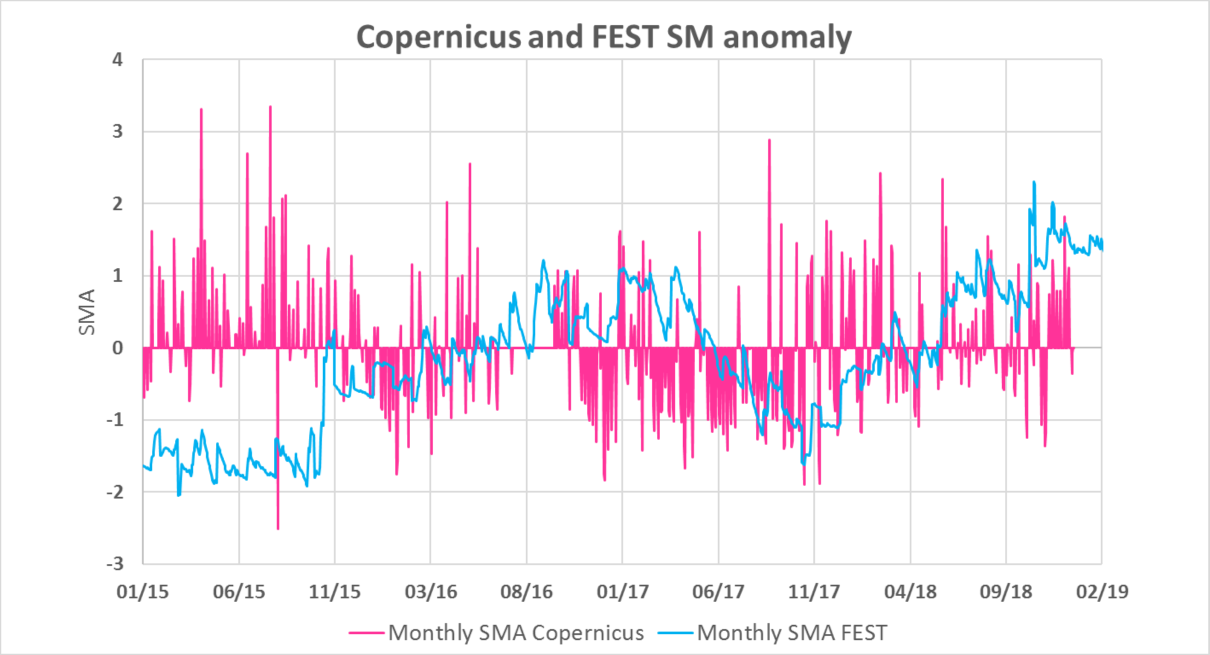

Figure 5.21 Comparison between Copernicus and FEST SMA

5.2.1.3 LST and RET anomaly

LST monthly anomaly is calculated using the average at basin scale of Landsat (L7 and L8) images from February 2014 to November 2019. In Figure 5.22 is visible the comparison between high resolution Landsat (30 meters) and MODIS (1 km) anomalies, RMSE equal to 1.0 and Nash index equal to -0.2 are obtained. Furthermore, RET monthly anomaly (RETA) is calculated and will be implemented in the drought index with SMA from FEST (Figure 5.23). A comparison with LST anomalies from Landsat and MODIS is provided, RMSE and Nash indices are visible in Table 5.11.

Table 5.11 Nash index and RMSE between RET and LST anomaly

	LSTA(MODIS)-RETA	LSTA(Landsat)- RETA
RMSE	0.8	0.89
Nash Index	0.31	0.15

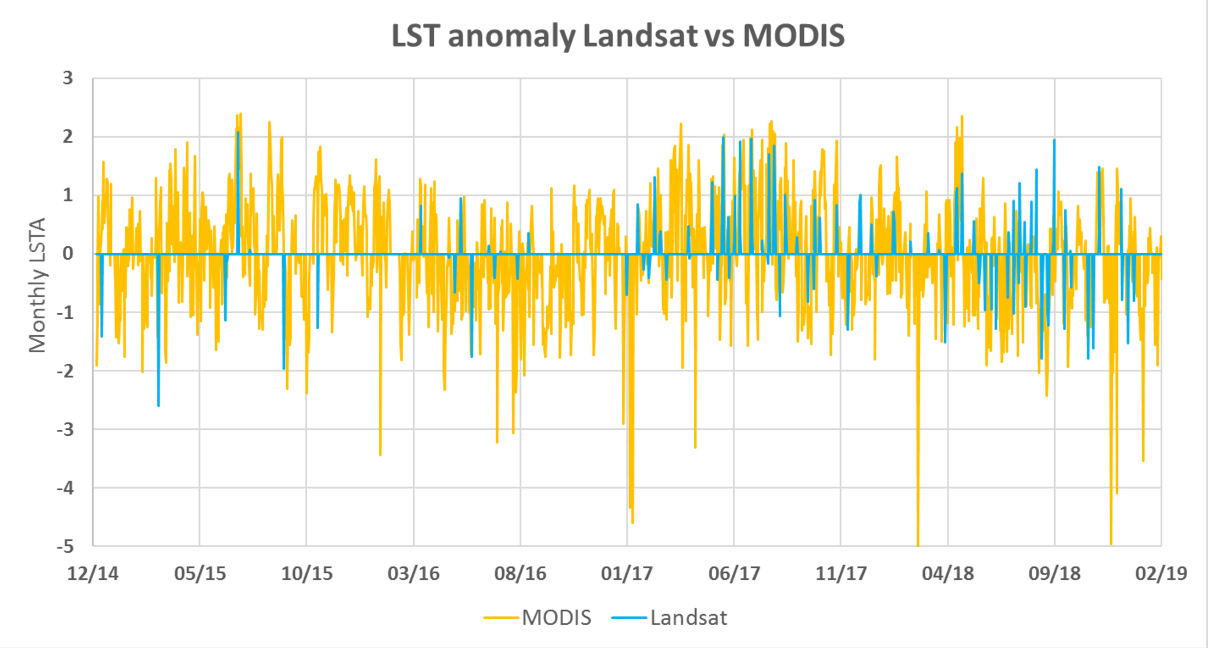

Figure 5.22 Comparison between LST monthly anomaly from MODIS and Landsat

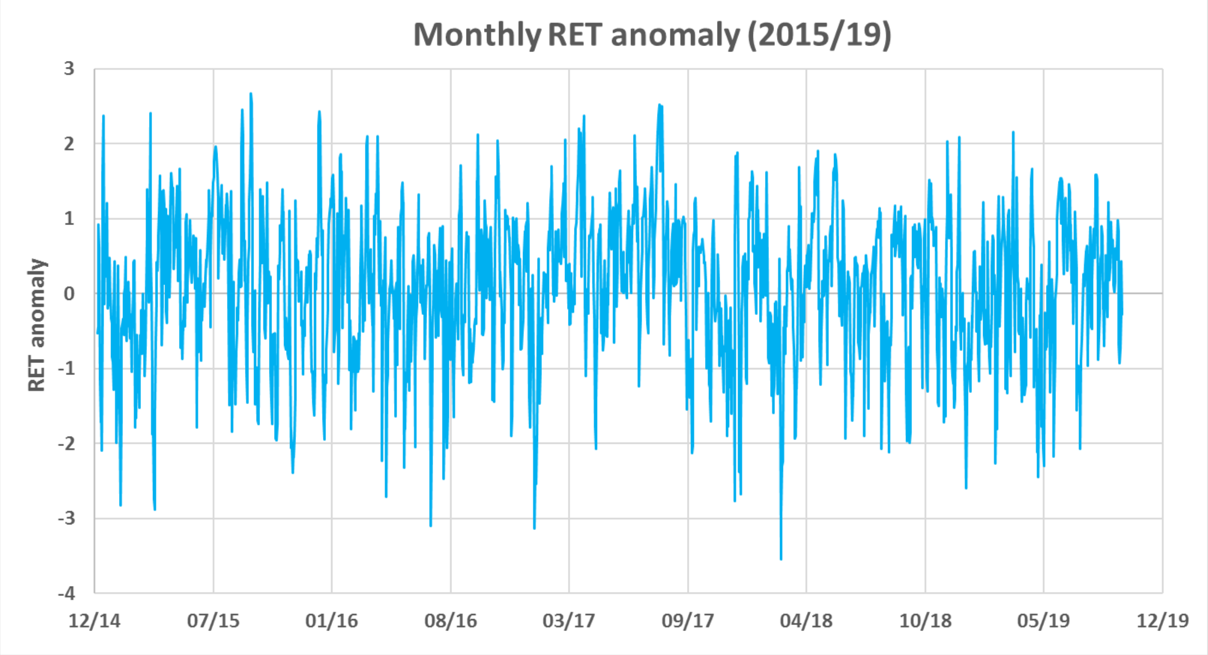

Figure 5.23 RET monthly anomaly

5.2.1.4 Vegetative indices anomaly

Vegetative indices, such as NDVI and NDWI, anomalies are calculated using the average at basin scale of Landsat (L7 and L8) images from February 2014 to June 2019 for NDVI and from February 2017 to December 2018 for NDWI. Total anomalies are affected by the same problem of seasoning trend, as LSTA, so even in this case monthly anomalies are calculated, a

RMSE of 1.06 is obtained between NDVI monthly and total anomaly and a RMSE of 1.08 for NDWI, comparisons are visible in Figure 5.24 and 5.25.

Moreover, the comparison between Landsat (30 meters) and MODIS (500 meters) NDVI monthly anomaly is provided (Figure 5.26) and the statistical indices are shown in Table 5.12.

Table 5.12 Nash index and RMSE between NDVI monthly anomaly from MODIS and Landsat

	NDVIA Landsat- MODIS
NASH index	0.20
RMSE	0.99

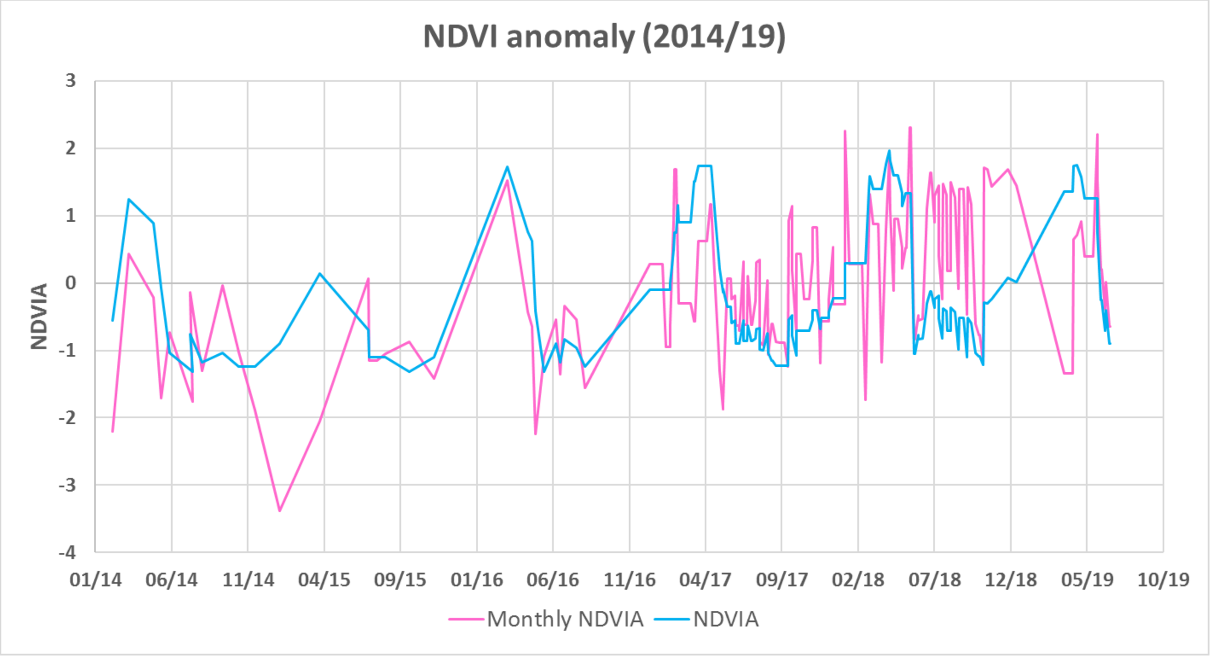

Figure 5.24 Comparison between monthly and total NDVI anomaly form Landsat

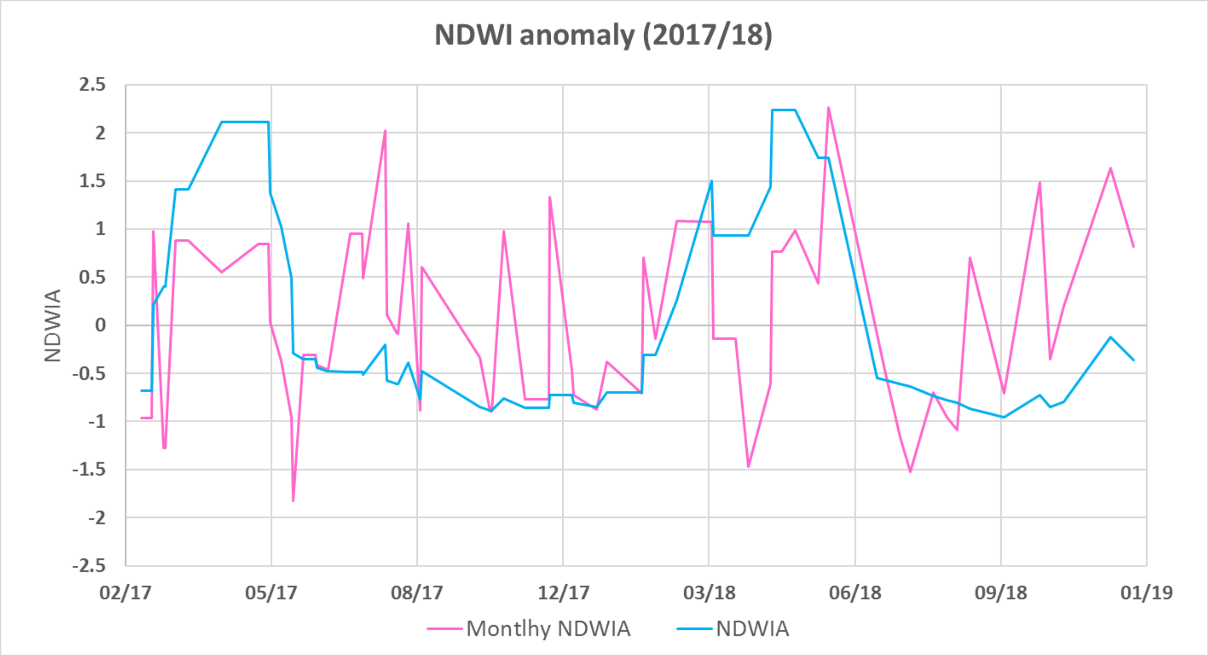

Figure 5.25 Comparison between monthly and total NDWI anomaly form Landsat

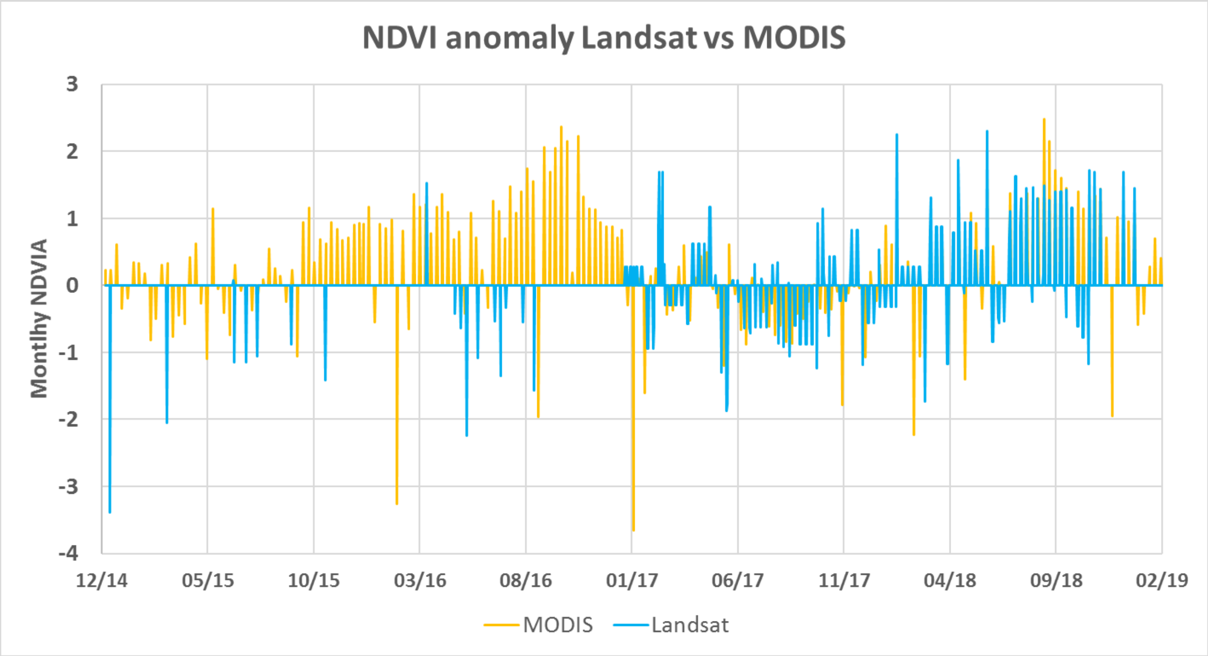

Figure 5.26 Comparison between NDVI monthly anomaly from Landsat and MODIS

5.2.1.5 Evapotranspiration deficit anomaly

Evapotranspiration anomaly is computed in term of deficit (ET_{def}) with respect the potential evapotranspiration (ET_p). The potential evapotranspiration is computed using the Penman-Monteith equation using meteorological forcing of the 45 stations spread in the case study area (the same used as input for hydrological model). The actual evapotranspiration is the simulated one. Thus, making the daily difference between actual e potential ET the ET deficit is obtained and the anomalies of the deficit are computed. Therefore, negative values of anomaly represent low deficit, actual evapotranspiration close to the potential one, on the contrary high values of anomaly mean stress conditions Anomalies are calculated both on total and monthly scale with a RMSE equal to 0.98. Even in this case to remove the seasonality monthly anomaly is chosen for the analysis (Figure 5.27).

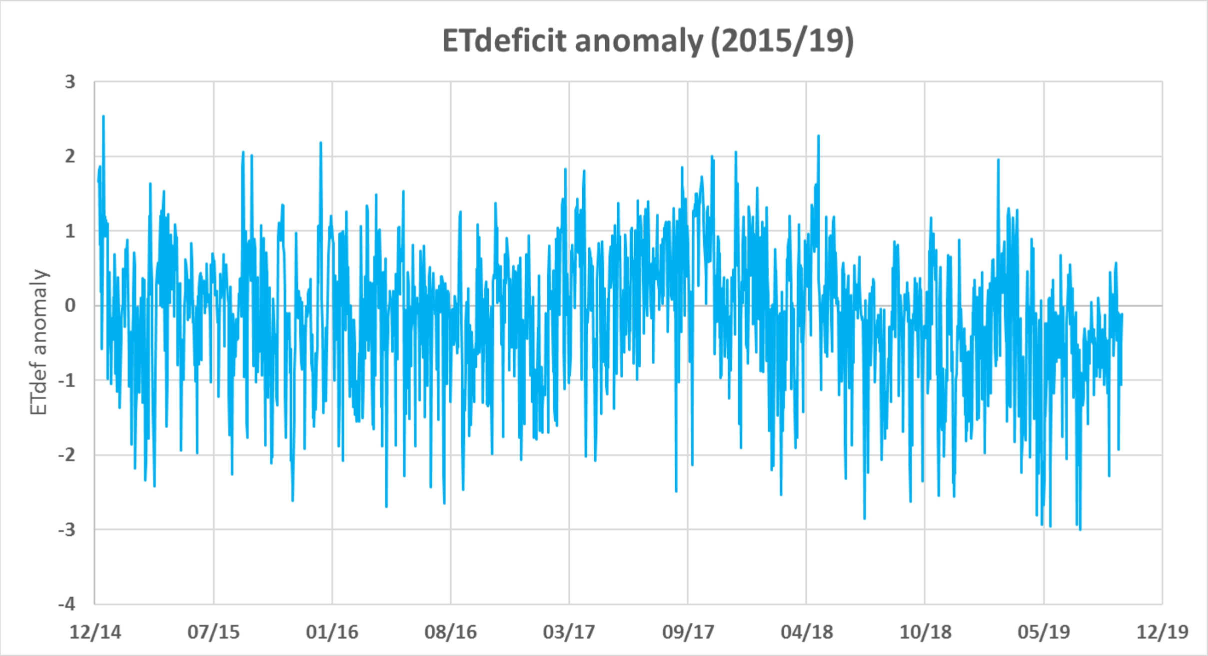

Figure 5.27 ET deficit monthly anomaly

5.2.1.6 SPEI

The SPEI is calculated using observed precipitation and potential evapotranspiration from P-M equation. In Figure 5.28 SPEI from January 2015 to 2018 is visible. Negative values are observed during summer period and positive in winter, the same trend observed in SPI1 calculation (Paragraph 5.2.1.1).

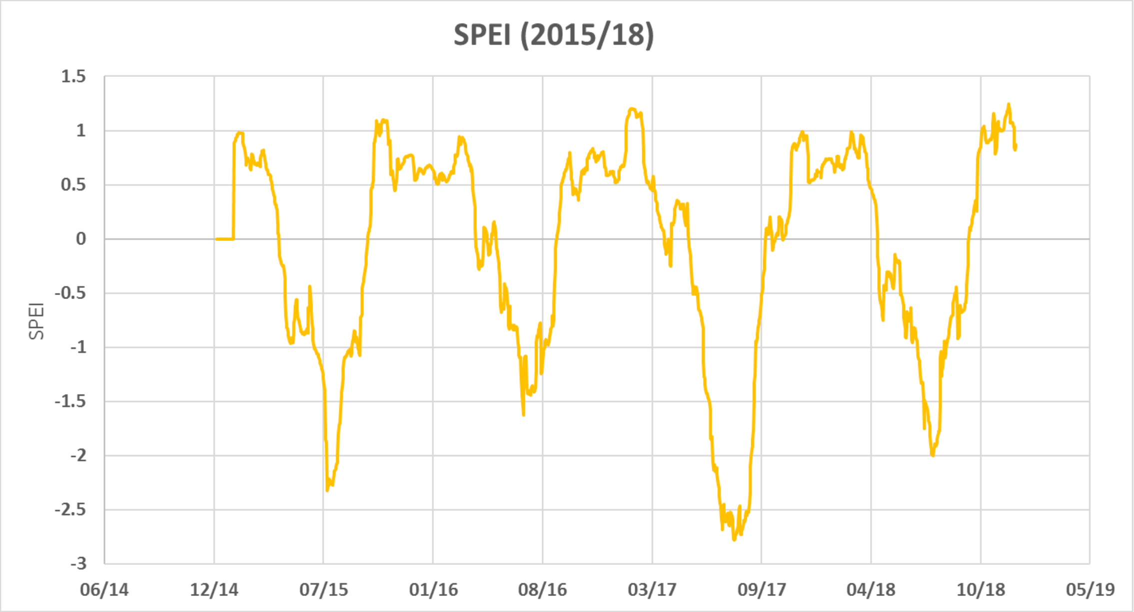

Figure 5.28 SPEI of observed precipitation

5.2.1.7 SWDI

The SWDI is computed using the FC and WP values at basin scale (visible in Table 5.13) and the SM series from FEST. A comparison between the trend of SWDI and SM monthly anomaly is reported in Figure 5.29. A correlation coefficient equal to 0.88 is obtained, SWDI evolution adequately follows the deficit periods observed using the SMA.

Table 5.13 Wilting point and field capacity at basin scale

WP [m^3/m^3]	**FC [m^3/m^3]**
0.1634	0.2769

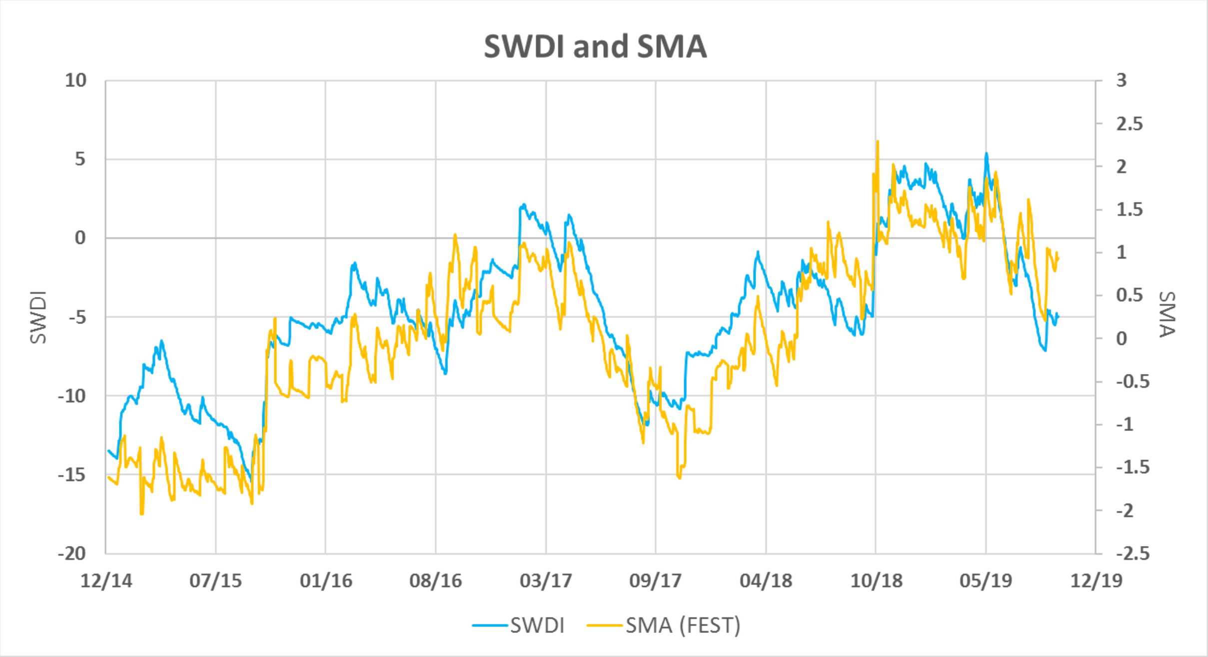

Figure 5.29 SWDI and SM monthly anomaly comparison

5.2.2 Anomaly on cultivated fields

In order to understand how the cultivated and irrigated fields affect the variation of SM, RET, NDVI, thus the anomalies, a comparison between averaged anomalies above all the consortium area (e.g. anomalies calculated in the previous paragraphs) and averaged anomalies only on cultivated fields in July is done. This is done to extract the only main cultivation during summer which are tomatoes.

Considering for each year only the pixels with Fcover higher than 0.1 in July (Table 5.14) of SM, RET maps retrieved from FEST and NDVI from Landsat, averaged values of SM, RET and NDVI are calculated. Then, on these values monthly anomalies are computed as done for the previous analysis.

Table5.14 Satellite images of Fcover in July for the years 2015-2018

	2015	**2016**	**2017**	**2018**
Fcover	3 July	5 July	8 July	3 July

The scatterplot in Figure 5.30 is built considering all the dates for those SM maps from FEST-EWB area available, thus, each point, represent for a fixed data the values of SM monthly anomaly averaged on the total basin area in x axis and the values of SM monthly anomaly averaged on only cultivated fields in y axis.

Analyzing the scatterplot is possible to observed different responses: the point in the fourth quadrant are the dates for those positive SMA are observed at basin scale while negative (e.g. SM deficit) at field scale, that means that cultivated areas, i.e. tomatoes field, suffer stress conditions. Instead, the point in the second quadrant show the opposite behavior, negative values of SMA are observed at basin scale while at field scale no deficit conditions are detected; in this case irrigation, applied on cultivated fields, increases the SMA values, cancelling the deficit condition at basin scale, probably effect of bare soils. The remaining points, in first and the third quadrant have the same sign of anomaly at field and basin scale. For that points shifted toward the vertical axis (e.g. higher/lower SMA values on cultivated fields) the same consideration of second/fourth quadrant can be done.

The scatterplot in term of RET and NDVI monthly anomaly are built in the same way considering RET maps from FEST and NDVI maps from Landsat (Figure 5.31 and 5.32). Both the scatterplots show less points in the second and fourth quadrant, that have the same meaning (e.g. irrigation/water stress in fields) of SMA scatterplot. This is a further prove of the agricultural drought process and the delay in response of vegetation stress. In fact, vegetation shows the higher angular coefficient and R^2 values equal to 0.75 and 0.52 respectively (Table 5.15).

Table 5.15 Angular coefficient and R2 between monthly anomaly on cultivated field and basin area

Monthly anomaly	**Angular coefficient**	**R^2**
SM	0.41	0.1
RET	0.60	0.35
NDVI	0.75	0.52

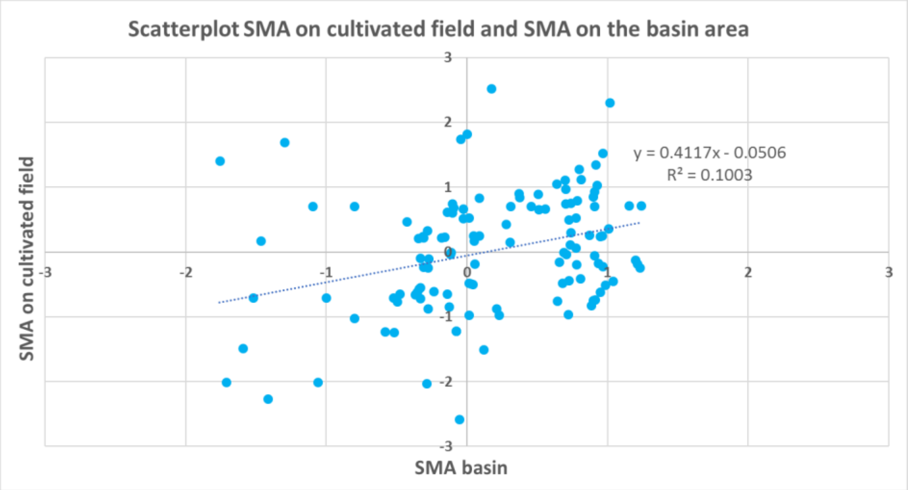

Figure 5.30 Scatterplot between SMA on cultivated fields and SMA on basin area

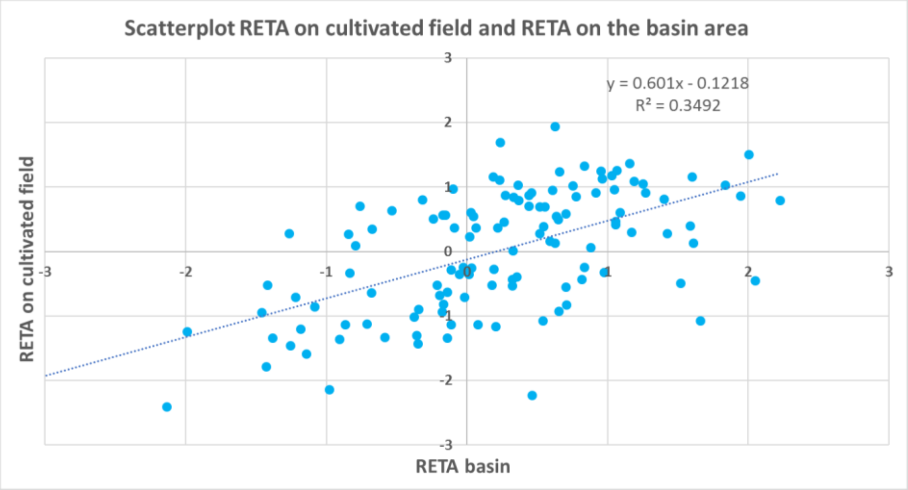

Figure 5.31 Scatterplot between RETA on cultivated fields and RETA on basin area

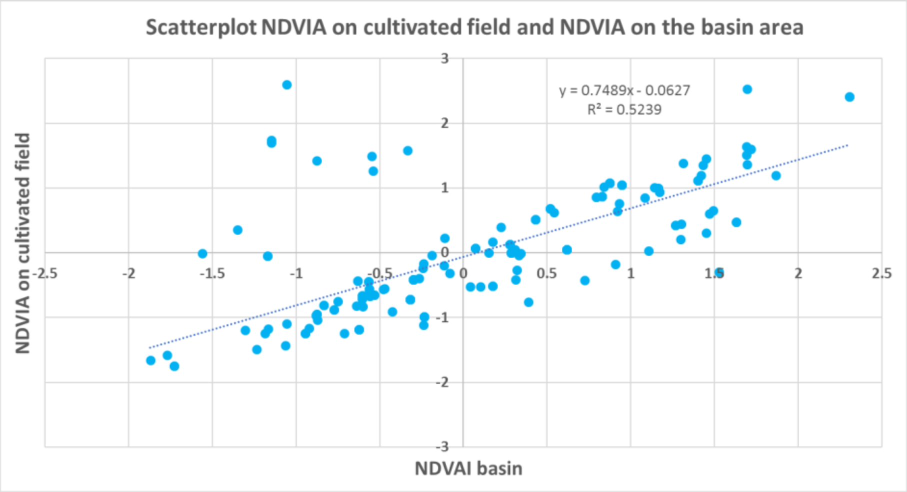

Figure 5.32 Scatterplot between NDVIA on cultivated fields and NDVIA on basin area

5.2.3 Anomaly maps

Anomalies time series based on one daily value averaged over the whole area, are useful to represent the trend of variables (precipitation, SM, LST, Vis) at basin scale in time.

Instead, anomaly maps calculated in different periods of the years give the possibility to focus on the spatial distribution of anomaly. Irrigated and not irrigated fields can be retrieved analyzing the values of anomaly at field scale.

The anomaly maps are computed in the irrigation season using an average and a standard deviation maps of SM, RET, LST and NDVI above all the years of simulation, then pixel by pixel the anomaly is calculated only for cultivated fields, e.g. only the pixels with Fcover higher than 0.1 are considered. The driest years of the simulated period are analyzed, 2015 and 2017. Looking at the SM, LST and RET anomaly, irrigated fields and fields in drought conditions can be detected. In Figure 5.33, in the red fields with negative values of SMA, and positive values of LSTA/ RETA drought conditions are observed, instead the blue fields are the irrigated ones. As we can see in Figure 5.34, the RET anomalies are lower than the LST anomalies because as see in Chapter 4, the model is colder than the observed temperature in summer period. Moreover, NDVI anomaly maps are computed, a comparison between 2017 and 2018 is visible in Figure 5.35. Notice that some parts of the consortium area, such us the woods (high values of NDVI) in the southern part and areas near the cities (not cultivated area), have negative values of NDVI that are not representative of drought. These areas can influence the values of mean and standard deviation on all the basin area, therefore even the anomalies computation.

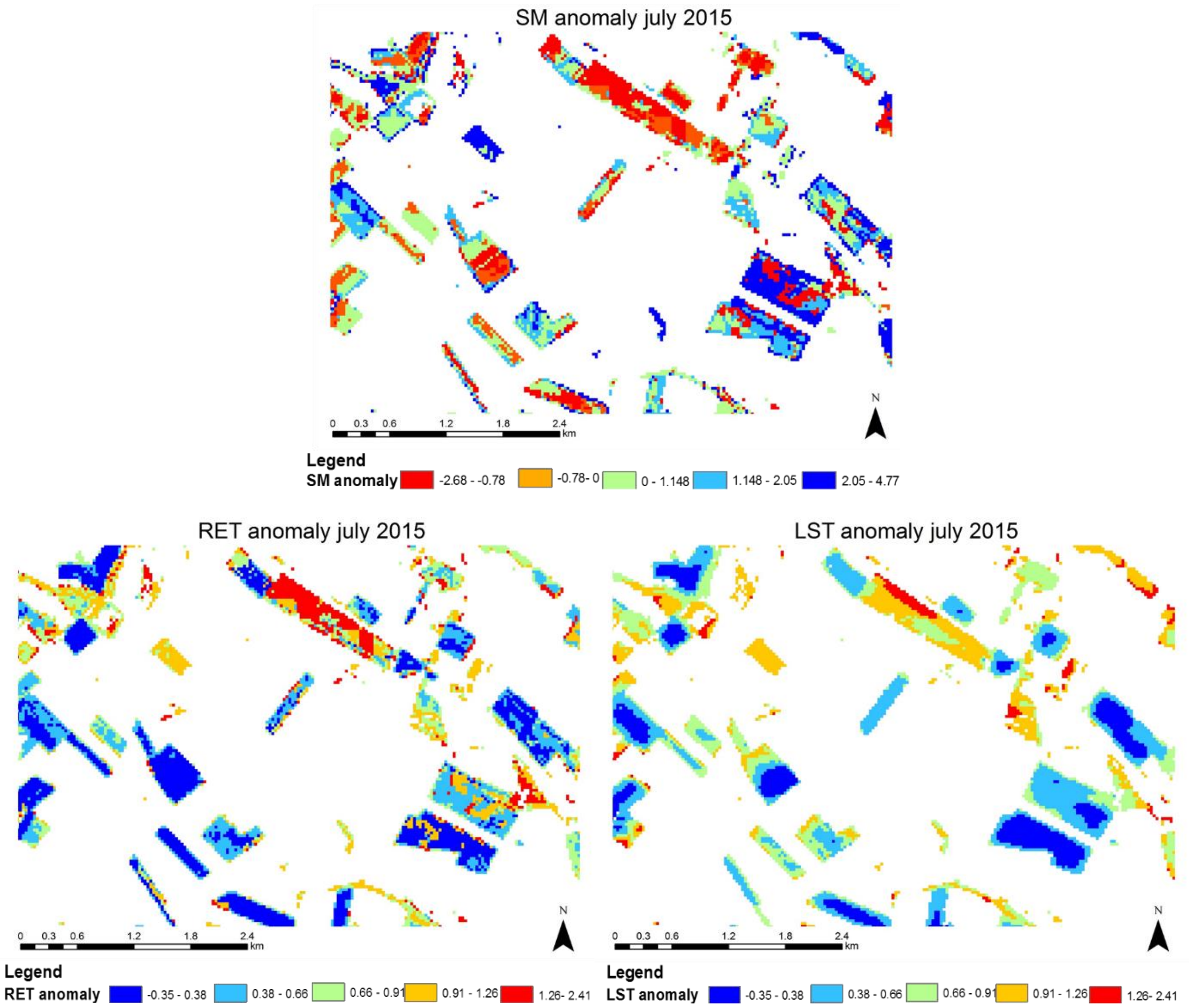

SM anomaly july 2015

RET anomaly july 2015

LST anomaly july 2015

Figure 5.33 Zoom on anomaly maps of SM, RET and LST at filed scale

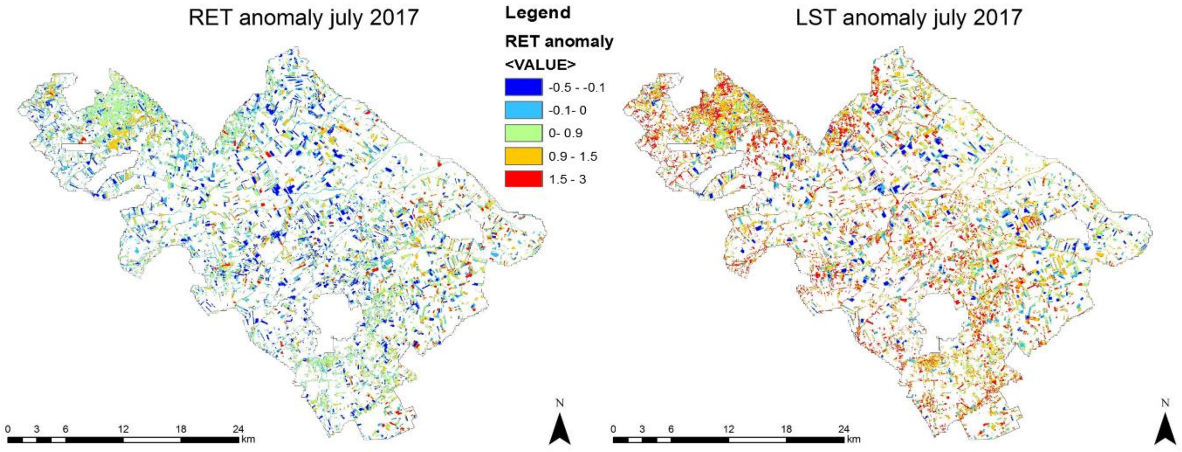

Figure 5.34 RET and LST anomaly maps at basin scale

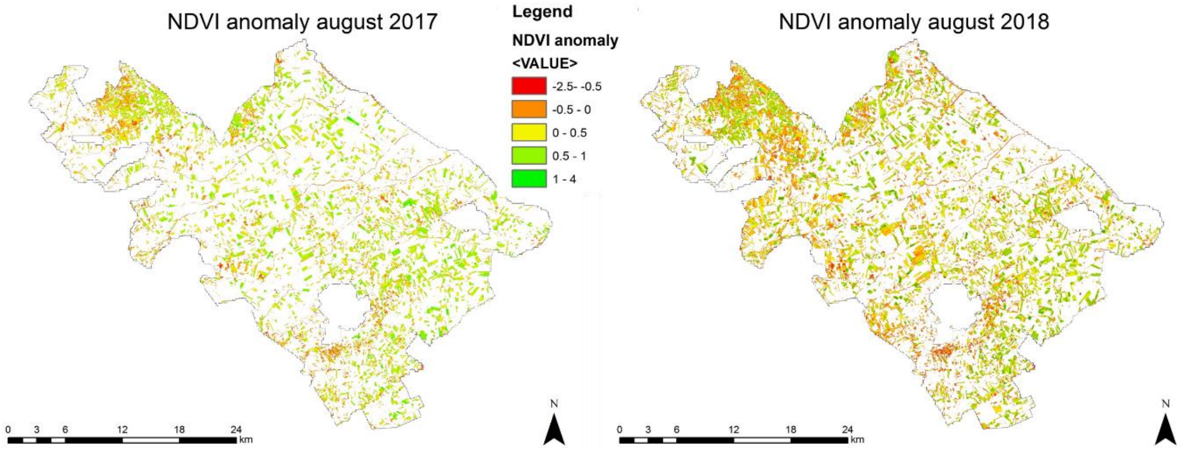

Figure 5.35 NDVI anomaly maps for summer 2017 and 2018

5.2.4 Correlation between anomalies

Pearson's correlation coefficients are computed between the anomalies at basin scale Table 5.16. SM, RET and ET deficit are the monthly anomalies from FEST, LST and NDVI are from Landsat also in term of monthly anomalies.

As we can see SMA and LSTA/RETA shows negative values of correlation, thus correlation coefficient between SPI or NDVI and SMA and coefficients between SPI or NDVI and LSTA/RETA will have the opposite sign. NDVI and LSTA shows positive values instead of a negative one, this incongruence is related to the different time response of the index to drought, as explained in Paragraph 5.1.2. ET deficit anomaly and SMA (LSTA/RETA) correlation is negative (positive) because high deficit in evapotranspiration means low values of soil moisture (high value of temperature) and vice versa.

Table 5.16 Pearson's correlation coefficients

Detailed Series 15-19								
SPI-SMA	SPI-LSTA	SPI-RETA	SPI-NDVIA	SMA-LSTA	SMA-RETA	NDVIA-SMA	NDVIA-RETA	*NDVIA-LSTA*
0.25	-0.26	-0.36	0.14	-0.16	-0.10	0.36	-0.01	0.14

ETdef-SMA	ETdef- LSTA	ETdef-RETA
-0.25	0.27	-0.64

5.2.5 Combined drought index

Combined drought index is evaluated using monthly anomaly of SM from FEST, monthly anomaly of RET and monthly anomaly of NDVI from Landsat (Figure 5.36). To easily compare the result with the index calculated using long time series, annual cumulated values of the indices are computed. Comparison between this index and the index calculated using SPI from ERA5, SM averaged monthly anomaly of satellite products, LST monthly anomaly from MODIS and NDVI monthly anomaly from MODIS is visible in Figure 5.37. As we can see, for the 2015 great difference is observed, probably due to the low values of the SM simulated with the hydrological model. Instead for the other years the indices agree.

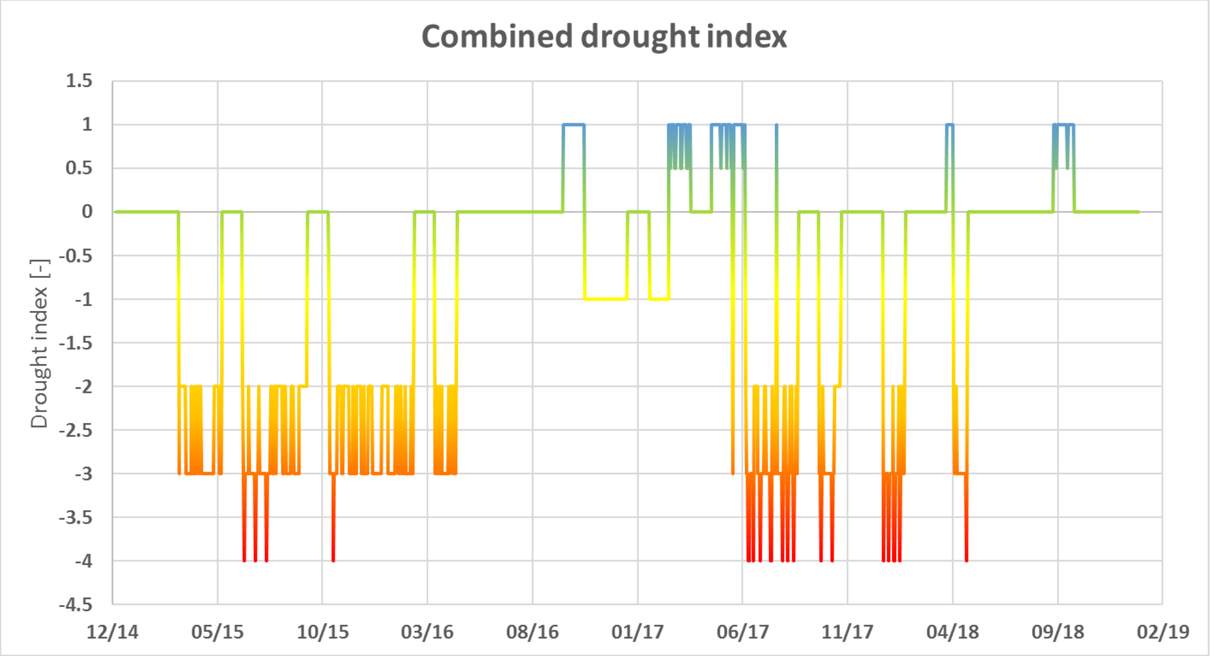

Figure 5.36 Combined drought index of high resolution analysis

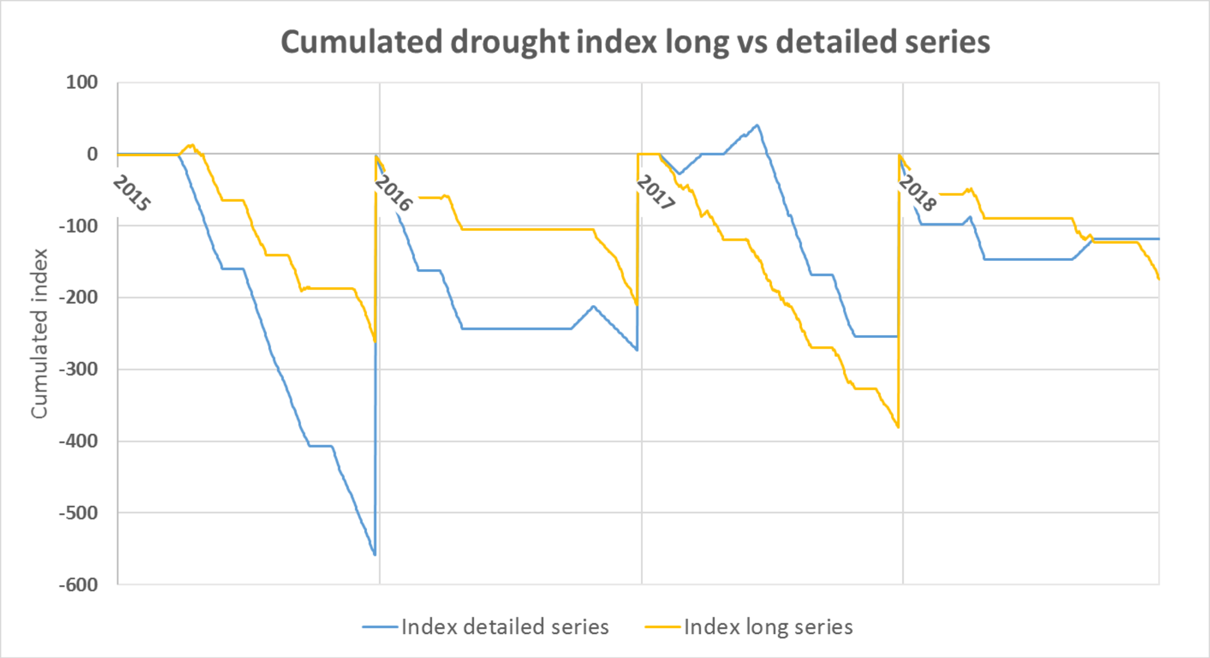

Figure 5.37 Comparison between combined drought index of high- and low-resolution data

Even in this case, a comparison with irrigation aqueduct volumes is provided (Table 5.17). The cumulated drought indices resulting for the years 2015 and 2016 agree with cumulated irrigation volumes (higher index, higher volume) and with cumulated irrigation and precipitation volumes (higher index, lower volume), as in the case of long time series analysis.

Table 5.17 Comparison between drought index and irrigation aqueduct volumes

Year	**Cumulated drought index [-]**	**Cumulated irrigation volume [m3]**	**Cumulated irrigation + precipitation volumes [m3]**
2015	-559	591,530,27	767,112,299
2016	-273	543,142,23	771,064,277

Furthermore, to have another prove of the capability of water stress condition detecting of the combined index a comparison between the SWDI is provided. Even the indices are not comparable in term of values, a comparison in term of cumulated indices is possible. As we can see in Figure 5.38, good agreement between the indices is observed.

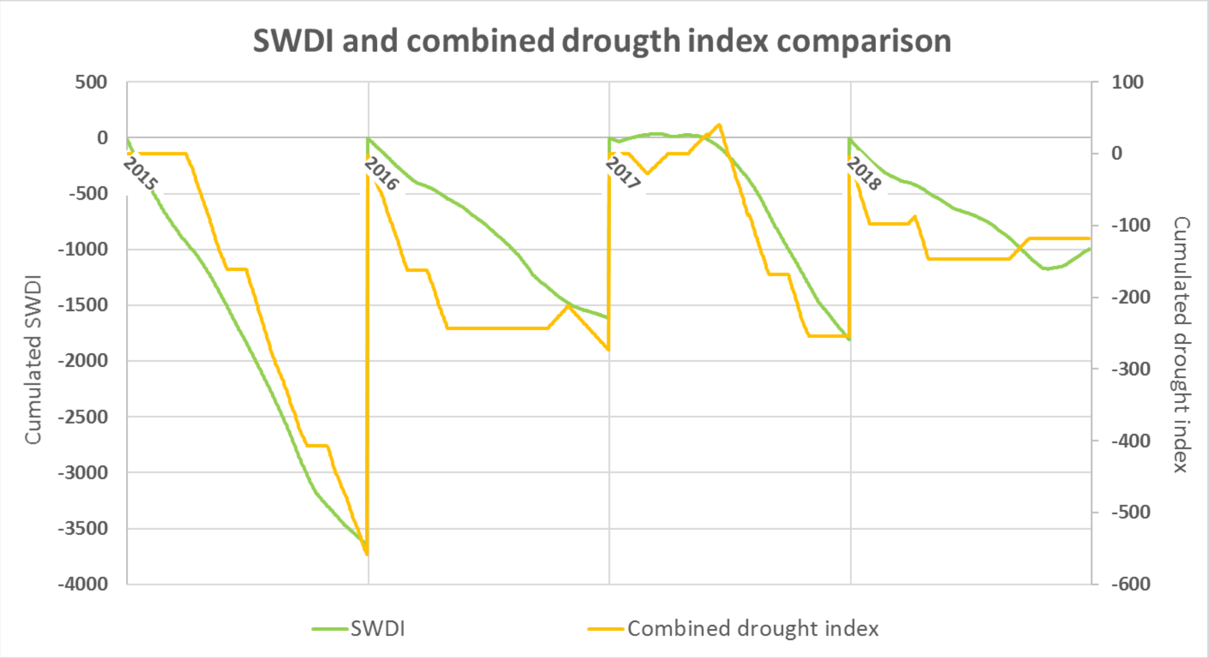

Figure 5.38 Comparison between combined drought index and SWDI

Conclusion

The case study area, Capitanata irrigation Consortium in Puglia, is characterized by flourishing agricultural activity but suffers water scarcity problems, especially during summer, thus an efficient water resource management is required. In this thesis a tool for water stress monitoring based on distributed hydrological model, ground observation and remote sensing data has been developed.

Firstly, soil moisture ground measurements retrieved from sensors and eddy covariance stations located in fields of tomato, wheat, asparagus and other vegetables have been analysed in combination with remotely sensed vegetation indices. Developing a research for new parameter or threshold useful in irrigation control, the results show that the vegetation indices follow the irrigation application and crop growth but no information on water stress could be retrieved due to the low amount of available satellite data exactly before and after an irrigation event.
Furthermore, correlating soil moisture, vegetative indices and land surface temperature at field scale, the low values of correlation obtained can be derived from the delay of vegetation status with respect to soil moisture variability.

Then, the same analysis is performed at basin scale using Landsat and Sentinel2 images and the soil moisture estimates from hydrological model FEST-EWB, which has been validated with Land Surface Temperature (LST) images from Landsat for the years 2015-2019. The results prove that the model is able to simulate the observed land surface temperature with low errors, hence, to correctly distribute the irrigation and to represent the spatial variability of the fields in term of LST, soil moisture and evapotranspiration. Indeed, investigating the spatial and temporal correlation between simulated and observed variables, depending on the sign of Pearson’s coefficient irrigated and not irrigated fields have been detected.

Then, this thesis proposed a combined drought index for agricultural drought process analysis at irrigation consortium scale. Two analysis at different spatial and temporal scale are performed: long time series analysis from 2000 to 2020 using remote sensing data of precipitation, SM, LST and vegetative indices at low spatial resolution (1km to 25 km), and a detailed analysis considering observed precipitation, simulated SM, RET and ET form FEST and high-resolution satellite images of LST and vegetative indices (30m). Firstly, for both precipitation series SPI and anomalies have been calculated. Between SPI values of observed and ERA5 precipitation a RMSE of 0.52 in obtained. Then, comparing the anomalies of SM from FEST and from the soil moisture satellite products (ESA CCI combined/active, SMOS and SMAP) RMSE equal to 1.15, 1.18, 1.22 and 1.28 are obtained respectively. Comparing monthly anomalies of RET from FEST and LST from Landsat and MODIS a RMSE equal to 0.80 and 0.89 are calculated. At the end comparing NDVI monthly anomaly from MODIS and Landsat/Sentinel2 data RMSE of 0.99 results.

The reliability of anomalies in detecting water stress conditions has been discussed analyzing two main issues: the differences between total and monthly anomalies and how anomalies of hydrological variables are correlated in the agricultural drought processes. The results show that monthly anomaly, being deprived of seasonality, are able to reproduce better the daily variation of the hydrological variables. Furthermore, the different time response of index of drought is highlighted, e.g. precipitation deficit is the first while vegetation stress is the last.

Therefore, the combined drought indicator based on the standardize precipitation index and monthly anomalies was computed. The results show that the indicator based on meteorological, soil moisture, evapotranspiration, land surface temperature and vegetation stress information at different spatial and temporal scale, is able to monitor agricultural drought and its evolution in space and time. In particular, the reliability of the developed tool has been discussed comparing the level of drought obtained with the values of irrigation aqueduct volumes of consortium. For the index based on the long time series, an angular coefficient of -38887 mc and an intercept $5x10^7$ of is obtained between drought index and irrigation volumes and an angular coefficient of 525873 mc and an intercept $9x10^8$ of between drought index and irrigation plus precipitation volumes. Instead, for index based on high resolution series a comparison with SWDI is provided, with a correlation coefficient equal to 0.88. Therefore, the anomalies and the agricultural combined drought index result good indicators able to capture the agricultural drought evolution in time and space.

Bibliography

Al Bitar, A., Leroux, D., Kerr, Y. H., Merlin, O., Richaume, P., Sahoo, A., & Wood, E. F. (2012). Evaluation of SMOS Soil Moisture Products Over Continental U.S. Using the SCAN/SNOTEL Network. *IEEE Transactions on Geoscience and Remote Sensing*, *50*(5), 1572–1586. https://doi.org/10.1109/TGRS.2012.2186581

Bastiaanssen, W. G. M., Noordman, E. J. M., Pelgrum, H., Davids, G., Thoreson, B. P., & Allen, R. G. (2005). SEBAL model with remotely sensed data to improve water-resources management under actual field conditions. *Journal of Irrigation and Drainage Engineering*, *131*(1), 85–93. https://doi.org/10.1061/(ASCE)0733-9437(2005)131:1(85)

Bauer-Marschallinger, B., Paulik, C., Hochstöger, S., Mistelbauer, T., Modanesi, S., Ciabatta, L., … Wagner, W. (2018). Soil Moisture from Fusion of Scatterometer and SAR: Closing the Scale Gap with Temporal Filtering. *Remote Sensing*, *10*(7). https://doi.org/10.3390/rs10071030

Bindlish, R., & Barros, A. P. (2001). Parameterization of vegetation backscatter in radar-based, soil moisture estimation. *Remote Sensing of Environment*, *76*(1), 130–137. https://doi.org/https://doi.org/10.1016/S0034-4257(00)00200-5

Brocca, L., Tarpanelli, A., Filippucci, P., Dorigo, W., Zaussinger, F., Gruber, A., & Fernández-Prieto, D. (2018). How much water is used for irrigation? A new approach exploiting coarse resolution satellite soil moisture products. *International Journal of Applied Earth Observation and Geoinformation*, *73*, 752–766. https://doi.org/https://doi.org/10.1016/j.jag.2018.08.023

Cammalleri, C., Ciraolo, G., La Loggia, G., & Maltese, A. (2012). Daily evapotranspiration assessment by means of residual surface energy balance modeling: A critical analysis under a wide range of water availability. *Journal of Hydrology*, *452–453*, 119–129. https://doi.org/10.1016/j.jhydrol.2012.05.042

Ceppi, A., Ravazzani, G., Corbari, C., Salerno, R., Meucci, S., & Mancini, M. (2014). Real-time drought forecasting system for irrigation management. *Hydrology and Earth System Sciences*, *18*(9), 3353–3366. https://doi.org/10.5194/hess-18-3353-2014

Corbari, C., Ravazzani, G., & Mancini, M. (2011). A distributed thermodynamic model for energy and mass balance computation: FEST-EWB. *Hydrological Processes*, *25*(9), 1443–1452. https://doi.org/10.1002/hyp.7910

Corbari, C., Salerno, R., Ceppi, A., Telesca, V., & Mancini, M. (2019). Smart irrigation forecast using satellite LANDSAT data and meteo-hydrological modeling. *Agricultural Water Management*, *212*(August 2018), 283–294. https://doi.org/10.1016/j.agwat.2018.09.005

Cui, C., Xu, J., Zeng, J., Chen, K. S., Bai, X., Lu, H., … Zhao, T. (2018). Soil moisture mapping from satellites: An intercomparison of SMAP, SMOS, FY3B, AMSR2, and ESA CCI over two dense network regions at different spatial scales. *Remote Sensing*, *10*(1). https://doi.org/10.3390/rs10010033

Del Pilar Jiménez-Donaire, M., Tarquis, A., & Vicente Giráldez, J. (2020). Evaluation of a combined drought indicator and its potential for agricultural drought prediction in southern Spain. *Natural Hazards and Earth System Sciences*, *20*(1), 21–33. https://doi.org/10.5194/nhess-20-21-2020

Dorigo, W., Wagner, W., Albergel, C., Albrecht, F., Balsamo, G., Brocca, L., … Lecomte, P. (2017). ESA CCI Soil Moisture for improved Earth system understanding: State-of-the art and future directions. *Remote Sensing of Environment*, *203*, 185–215. https://doi.org/https://doi.org/10.1016/j.rse.2017.07.001

Droogers, P. (2000). Estimating actual evapotranspiration using a detailed agro-hydrological model. *Journal of Hydrology*, *229*(1–2), 50–58. https://doi.org/10.1016/S0022-1694(99)00198-5

Entekhabi, D., Njoku, E. G., O'Neill, P. E., Kellogg, K. H., Crow, W. T., Edelstein, W. N., … Van Zyl, J. (2010). The Soil Moisture Active Passive (SMAP) Mission. *Proceedings of the IEEE*, *98*(5), 704–716. https://doi.org/10.1109/JPROC.2010.2043918

Fischer, G., Tubiello, F. N., van Velthuizen, H., & Wiberg, D. A. (2007). Climate change impacts on irrigation water requirements: Effects of mitigation, 1990-2080. *Technological Forecasting and Social Change*, *74*(7), 1083–1107. https://doi.org/10.1016/j.techfore.2006.05.021

Giacomelli, A., Bacchiega, U., Troch, P. A., & Mancini, M. (1995). Evaluation of surface soil moisture distribution by means of SAR remote sensing techniques and conceptual hydrological modelling. *Journal of Hydrology*, *166*(3), 445–459. https://doi.org/https://doi.org/10.1016/0022-1694(94)05100-C

Hatfield, J. L., Gitelson, A. A., Schepers, J. S., & Walthall, C. L. (2008). Application of spectral remote sensing for agronomic decisions. *Agronomy Journal*, *100*(3 SUPPL.). https://doi.org/10.2134/agronj2006.0370c

Imaoka, K., Maeda, T., Kachi, M., Kasahara, M., Ito, N., & Nakagawa, K. (2012). Status of AMSR2 instrument on GCOM-W1. In H. Shimoda, X. Xiong, C. Cao, X. Gu, C. Kim, & A. S. K. Kumar (Eds.), *Earth Observing Missions and Sensors: Development, Implementation, and Characterization II* (Vol. 8528, pp. 201–206). https://doi.org/10.1117/12.977774

Jiménez-Muñoz, J. C., & Sobrino, J. A. (2003). A generalized single-channel method for retrieving land surface temperature from remote sensing data. *Journal of Geophysical Research: Atmospheres*, *108*(D22). https://doi.org/10.1029/2003JD003480

Kerr, Y. H., Waldteufel, P., Wigneron, J.-., Martinuzzi, J., Font, J., & Berger, M. (2001). Soil moisture retrieval from space: the Soil Moisture and Ocean Salinity (SMOS) mission. *IEEE Transactions on Geoscience and Remote Sensing*, *39*(8), 1729–1735. https://doi.org/10.1109/36.942551

Kerr, Y. H., Waldteufel, P., Wigneron, J., Delwart, S., Cabot, F., Boutin, J., … Mecklenburg, S. (2010). The SMOS Mission: New Tool for Monitoring Key Elements ofthe Global Water Cycle. *Proceedings of the IEEE*, *98*(5), 666–687. https://doi.org/10.1109/JPROC.2010.2043032

Martínez-Fernández, J., González-Zamora, A., Sánchez, N., & Gumuzzio, A. (2015). A soil water based index as a suitable agricultural drought indicator. *Journal of Hydrology*, *522*, 265–273. https://doi.org/10.1016/j.jhydrol.2014.12.051

Merlin, O., Duchemin, B., Hagolle, O., Jacob, F., Coudert, B., Chehbouni, G., … Kerr, Y. (2010). Disaggregation of MODIS surface temperature over an agricultural area using a time series of Formosat-2 images. *Remote Sensing of Environment*, *114*(11), 2500–2512. https://doi.org/https://doi.org/10.1016/j.rse.2010.05.025

Petropoulos, G., Carlson, T. N., Wooster, M. J., & Islam, S. (2009). A review of Ts/VI remote sensing based methods for the retrieval of land surface energy fluxes and soil surface moisture. *Progress in Physical Geography*, *33*(2), 224–250. https://doi.org/10.1177/0309133309338997

Ravazzani, G., Corbari, C., Ceppi, A., Feki, M., Mancini, M., Ferrari, F., … Ober, G. (2017). From (cyber)space to ground: New technologies for smart farming. *Hydrology Research*, *48*(3), 656–672. https://doi.org/10.2166/nh.2016.112

Sepulcre-Canto, G., Horion, S., Singleton, A., Carrao, H., & Vogt, J. (2012). Development of a Combined Drought Indicator to detect agricultural drought in Europe. *Natural Hazards and Earth System Science*, *12*(11), 3519–3531. https://doi.org/10.5194/nhess-12-3519-2012

Skokovic, D. Calibration and Validation of Thermal Infrared Remote Sensing Sensors and Land/Sea Surface Temperature algorithms over the Iberian Peninsula. Ph.D. dissertation, Universidad de Valencia, Valencia, Spain, 2017

Svoboda, M., & Fuchs, B. (2017). *Handbook of Drought Indicators and Indices**. https://doi.org/10.1201/9781315265551-12

Vicente-Serrano, S. M., Beguería, S., & López-Moreno, J. I. (2010). A multiscalar drought index sensitive to global warming: The standardized precipitation evapotranspiration index. *Journal of Climate*, *23*(7), 1696–1718. https://doi.org/10.1175/2009JCLI2909.1

Vinukollu, R. K., Wood, E. F., Ferguson, C. R., & Fisher, J. B. (2011). Global estimates of evapotranspiration for climate studies using multi-sensor remote sensing data: Evaluation of three process-based approaches. *Remote Sensing of Environment*, *115*(3), 801–823. https://doi.org/10.1016/j.rse.2010.11.006

Vuolo, F., Essl, L., & Atzberger, C. (2015). Costs and benefits of satellite-based tools for irrigation management. *Frontiers in Environmental Science*, *3*(JUL), 1–12. https://doi.org/10.3389/fenvs.2015.00052

Wagner, W, Scipal, K., Boogard, H., van Diepen, K., Beck, R., Nobbe, E., & Savin, I. (2000). Assessing water-limited crop production with a scatterometer based crop growth monitoring system. *IGARSS 2000. IEEE 2000 International Geoscience and Remote Sensing Symposium. Taking the Pulse of the Planet: The Role of Remote Sensing in Managing the Environment. Proceedings (Cat. No.00CH37120)*, *4*, 1696–1698 vol.4. https://doi.org/10.1109/IGARSS.2000.857316

Wagner, Wolfgang, Hahn, S., Kidd, R., Melzer, T., Bartalis, Z., Hasenauer, S., … Steinnocher, K. (2013). The ASCAT Soil Moisture Product: A Review of its Specifications, Validation

Results, and Emerging Applications. *Meteorologische Zeitschrift*, *22*(1), 5–33. https://doi.org/10.1127/0941-2948/2013/0399

Wu, H., Svoboda, M. D., Hayes, M. J., Wilhite, D. A., & Wen, F. (2007). Appropriate application of the standardized precipitation index in arid locations and dry seasons. *International Journal of Climatology*, *27*(1), 65–79. https://doi.org/10.1002/joc.1371

Siti web

(1) https://bari.ilquotidianoitaliano.com/attualita/2012/08/news/siccita-allarme-coldiretti-per-la-puglia-108-milioni-di-metri-cubi-dacqua-in-meno-rispetto-al-2011-14159.html/

(2) https://www.quotidianodipuglia.it/regione/in_puglia_emergenza_siccita_distrutti_i_nostri_raccolti-2552780.html

Index of Figures

Figure 1.1 Spectral signature of vegetation, soil and water ………………………………...13

Figure 1.2 Agricultural drought process……………………………………………………17

Figure 2.1 Case study area: Capitanata irrigation Consortium……………..…………………23

Figure 2.2 Spatial distribution of GROW sensors ……..……………………………………24

Figure 2.3 Sensors configuration (southern zone) ……………………………………….…26

Figure 2.4 Sensors configuration (eastern zone) ………………………………..…………26

Figure 2.5 Fields with monitoring stations…………………………………………………27

Figure 2.6 Temporal duration of monitoring stations data……………………………………27

Figure 2.7 Pixel size of SMOS and SMAP images…………………………………………...29

Figure 2.8 Pixel size of ESA CCI active/combined images……………….…………………29

Figure 2.9 Clouds in LST satellite images ……………………………………………………30

Figure 2.10 Image with strips of L7 satellite …………………………………………………31

Figure 2.11 Cropped LST image …………………………………………………….………31

Figure 2.12 Meteorological stations distribution in the territory of Puglia with Consortium area highlighted..……………………………………………………………………..…………32

Figure 3. 2 Eastern fields with sensors on 22nd of July (on the left) and on 20th of October (on the right)….…………….……………..…………………………………………………….36

Figure 3.2 Southern fields with sensors on 22nd of July (on the left) and on 20th of October (on the right)……….……………………………………………………………….…………37

Figure 3.3 Soil moisture time series of GROW sensors.……………….……………….………39

Figure 3.4 Soil moisture and vegetative indices of sensors in tomato fields…………………41

Figure 3.5 Soil moisture and vegetative indices of sensors in asparagus fields………………43

Figure 3.6 Soil moisture and vegetative indices of sensors in fields vegetables………………43

Figure 3.7 De Filippo field during tomatoes cultivation……….…………………………..44

Figure 3.8 Soil moisture and vegetative indices of Onoranza Consortium tomato field………45

Figure 3.9 Soil moisture and vegetative indices of De Filippo tomato field …………………..45

Figure 3.10 Soil moisture and vegetative indices of De Filippo wheat field …………………..46

Figure 4.1 Trend of observed LST and simulated RET ……….…………………………..49

Figure 4.2 AMBE between simulated RET and observed LST from Landsat images………...49

Figure 4.3 Comparison between maps of LST from Landsat and RET from FEST-EWB…... 51

Figure 4.4 Autocorrelation curves of hydrological variables and soil parameters………52

Figure 4.5 NDVI-RET and NDVI-LST correlation maps………………………………54

Figure 4.6 Zoom at field scale of NDVI-SM, NDVI-RET, NDVI-LST correlation maps…… 54

Figure 4.7 Comparison at field scale of LST-ET correlation maps in winter and summer period……………………………………………………………………………………55
Figure 4.8 Spatial LST-NDVI relationship…………………………………………………56
Figure 4.9 LST- NDVI and RET-NDVI spatial relationship…………………………………..57
Figure 5.1 PA of ERA5 precipitation…...……………………………………………………..60
Figure 5.2 SPI of ERA5 precipitation…………………………………………………………60
Figure 5.3 Comparison between monthly and total anomaly of SMOS soil moisture.………...62
Figure 5.4 Comparison between monthly and total anomaly of SMAP soil moisture…………62
Figure 5.5 Comparison between monthly and total anomaly of ESA CCI Active soil moisture……………………………………………………………………………………….63
Figure 5.6 Comparison between monthly and total anomaly of ESA CCI Combined soil moisture……………………………………………………………………………………….63
Figure 5.7 Soil moisture anomaly averaged of SMOS, SMAP, ESA CCI Active and combined anomaly………………………………………………………………………………………64
Figure 5.8 Comparison between monthly and total LST anomaly from MODIS…………….65
Figure 5.9 Comparison between total anomalies of vegetative indices from MODIS…………66
Figure 5.10 Zoom on opposite peaks observed in NDVI and NDWI anomalies………………67
Figure 5.11 Comparison between monthly anomalies of NDVI and NDWI…………………..67
Figure 5.12 Cumulated drought index of long time series analysis……………………………69
Figure 5.13 Comparison between cumulated drought index computed using PA and SPI1…..70
Figure 5.14 Comparison between SPI, PA and SMA of the months for those inconsistency is observed………………………………………………………………………………………72
Figure 5.15 A zoom on 2020: comparison between the drought index calculated with SPI and PA..…………………………………………………………………………………………73
Figure 5.16 Irrigation aqueduct volumes and drought index comparison (dashed lines drought index with PA, continuous lines drought index with SPI)……………………………………74
Figure 5.17 Scatterplot between drought index and irrigation volumes and between drought index and irrigation plus precipitation volumes………………………………………………75
Figure 5.18 PA of observed precipitation……………………………………………………..77
Figure 5.19 Comparison between SPI of observed and ERA5 precipitation…………………..77
Figure 5.20 Comparison between monthly and total anomaly of simulated SM……………..78
Figure 5.21 Comparison between Copernicus and FEST SMA……………………….……….. 79

Figure 5.22 Comparison between LST monthly anomaly from MODIS and Landsat……….. 80
Figure 5.23 RET monthly anomaly……….…………………………………..……………80
Figure 5.24 Comparison between monthly and total NDVI anomaly form Landsat…………..81
Figure 5.25 Comparison between monthly and total NDWI anomaly form Landsat…………..82
Figure 5.26 Comparison between NDVI monthly anomaly from Landsat and MODIS……….82

Figure 5.27 ET deficit monthly anomaly…..…………………………………...……………83
Figure 5.28 SPEI of observed precipitation………………………………………………...84
Figure 5.29 SWDI and SM monthly anomaly comparison…………………………………85
Figure 5.30 Scatterplot between SMA on cultivated fields and SMA on basin area…………86
Figure 5.31 Scatterplot between RETA on cultivated fields and RETA on basin area……….87
Figure 5.32 Scatterplot between NDVIA on cultivated fields and NDVIA on basin area……..87
Figure 5.33 Zoom on anomaly maps of SM, RET and LST at filed scale……………………...88
Figure 5.34 RET and LST anomaly maps at basin scale………………………………………89
Figure 5.35 NDVI anomaly maps for summer 2017 and 2018………………………………..89
Figure 5.36 Combined drought index of high resolution analysis……………………………..90
Figure 5.37 Comparison between combined drought index of high- and low-resolution data...91
Figure 5.38 Comparison between combined drought index and SWDI……………………….92

Index of Tables

Table 1.1 Classification of drought according to SPI…..…..…………………………………19

Table 1.2 Classification of drought according to SWDI………………………………………20

Table 1.3 Classification of drought according to the agricultural combined drought index.....21

Table 2.1 Example of sensors dataset………………………………………………………25

Table 2.2 Summary of precipitation, soil moisture, land surface temperature and vegetation indices satellite dataset……………………………………………………………………….. 33

Table 3.1 Tomato sensors coordinates in UTM 33N…………………………………………..35

Table 3.2 Tomato sensors codes and their fields of installation………………………………36

Table 3.3 Number of irrigations applied on tomato fields……………………………………..37

Table 3.4 Satellite images used for vegetation parameters recovering………………………..40

Table 3.5 Vegetables sensors coordinate in UTM 33N………………………………………..42

Table 3.6 Coordinate of field with monitoring stations………………………………………..44

Table 3.7 Pearson correlation coefficients between SM, LST and NDVI……………………..47

Table 4.1 Average temperature of LST and FEST……………………………………………48

Table 4.2 Dates used for temporal correlation year2017………………………………………53

Table 4.3 Dates used for temporal correlation year 2018..……………………………………53

Table 4.4 Pearson's coefficient signs and their interpretation…………………………………53

Table 5.1 RMSE between monthly and total anomalies for each soil moisture satellite product…..…………………………………………………………………………………61

Table 5.2 RMSE between soil moisture products anomalies…………………………………61

Table 5.3 RMSE between vegetative indices total anomalies…………………………………65

Table 5.4 PA values for the days corresponding to NDVI and NDWI opposite peaks……..…66

Table 5.5 Correlation coefficients between anomalies………………………………………..68

Table 5.6 Correlation coefficients between LST and NDVI anomalies for winter and summer period……………………………………………………………………………………68

Table 5.7 Months with inconsistency in term of SPI and SMA, comparison between SPI from observed and ERA5 precipitation…………………………………………………………..71

Table 5.8 Comparison between the number of days with inconsistency observed in the drought index calculated with PA and SPI…………………………………………………………71

Table 5.9 Angular coefficients and R^2 between drought index and irrigation volume (and precipitation…………………………………………………………………………………..75

Table 5.10 Nash index and RMSE between simulated and remote sensed soil moisture monthly anomaly………………………………………………………………………………78

Table 5.11 Nash index and RMSE between RET and LST anomaly…………………………..79

Table 5.12 Nash index and RMSE between NDVI monthly anomaly from MODIS and Landsat…………………………………………………………………………………..81
Table 5.13 Wilting point and field capacity at basin scale……………………………………..84
Table 5.14 Satellite images of Fcover in July for the years 2015-2018………………………85
Table 5.15 Angular coefficient and R2 between monthly anomaly on cultivated field and basin area……………………………………………………………………………………86
Table 5.16 Pearson's correlation coefficients………………………………………………….90
Table 5.17 Comparison between drought index and irrigation aqueduct volumes…………….91

Ringraziamenti

Questi anni universitari non si sono conclusi come speravo, qualcosa più grande di noi ha preso il sopravvento nella vita di tutti i giorni e l’ha modificata e stravolta. Sarà una laurea speciale e fuori dal comune e a maggior ragione voglio ringraziare tutti coloro che mi hanno supportata in questo percorso.
Prima di tutto, voglio ringraziare proprio il Poli che mi ha accolta a 18 anni appena arrivata dalla Sicilia, mi ha fatto crescere, mi ha formato e fatto diventare ciò che sono adesso.
Ringrazio la mia Prof. Chiara Corbari che mi ha seguito ed aiutato in questo lavoro di tesi, nonostante tutte le difficoltà che si sono presentate.
Ringrazio mia madre per avermi sostenuto in ogni scelta e mio padre che mi ha fatto sempre sentire orgogliosa di essere sua figlia. Ringrazio Adriano mia esatta metà. Ringrazio Francesca che è al mio fianco dal primo anno e credo non smetterà mai di esserlo. Ringrazio Cristina, senza la quale probabilmente non sarei arrivata viva a fine quarantena. Ringrazio il Portogallo che mi ha fatto scoprire un modo nuovo vedere le cose.
Ringrazio la mia seconda famiglia ESN, per avermi fatto sentire parte di qualcosa, ringrazio Albe, Sacco e Ale per tutti i momenti condivisi. Ringrazio Francesca per esser diventata in così poco tempo così tanto. Ringrazio Antonio per sopportarmi da 17 anni. Ringrazio tutti i miei amici di giù, tutti i miei colleghi e le persone conosciute qui a Milano durante questi anni.
Infine, ringrazio Leonardo per essere il mio punto di riferimento.